ABSTRACT

Title of Document:	THERMAL IMAGING OF MULTIWALLED CARBON NANOTUBES. Kamal Hussain Baloch, Doctor of Philosophy, 2010
Directed By:	Professor John Cumings, Chemical Physics Program and Department of Materials Science and Engineering

Since early days of their discovery, it has been realized that Carbon Nanotubes (CNTs) have an unusually high thermal conductivity. Unfortunately, the amount of heat they can transfer from one medium to another can be limited by their thermal contact resistance, R_c, which in the worst case can result in thermally insulating bulk materials. Prior studies on individual nanotubes have reached various disparate conclusions, partly because many techniques employed for measuring such small samples rely on uncharacterized heat sources thus leaving fundamental uncertainties in the measurements. This has caused concerns that the true potential of these extraordinary thermal conductors will remain untapped. Relying on solid to liquid phase transition of sub-200nm Indium islands for thermometry, we report direct measurement of R_c by employing an independently characterized metallic heat source. Also we demonstrate that this contact resistance can be reduced by almost two orders of magnitude if a CNT is imbedded into metal contacts. Additionally in

our preliminary data on a self-heated CNT we observe that the substrate gets hot while the CNT itself remains cold when electric current is passed through it. This observation cannot be explained by assuming joule heating to be the primary source of heat transfer. We can qualitatively explain these results by assuming that hot electrons flowing through the biased CNT can be scattered off the phonons of a dielectric substrate. Principles of the novel measurement technique, experimental results and simulations are presented in this dissertation.

.

THERMAL IMAGING OF MULTIWALLED WALLED CARBON NANOTUBES

By

Kamal Hussain Baloch

Dissertation submitted to the Faculty of the Graduate School of the
University of Maryland, College Park, in partial fulfillment
of the requirements for the degree of
PhD
2010

Advisory Committee:
Professor John Cumings, Chair
Professor Richard Greene, Deans Representative
Professor Michael Fuhrer
Professor Salamanca-Riba
Professor Min Ouyang

Preface

This dissertation starts with chapter 1 which gives an introduction to the morphology of the carbon nanotubes. Their two most common synthesis methods, arc-discharge method and chemical vapor deposition method are discussed there as well. The theory of their fundamental electronic and thermal properties is outlined in chapter 2. This chapter also lists some interesting experiments done since their discovery to explore these properties. Chapter 3 is dedicated to two important properties of nanotubes namely; thermal contact resistance and remote electron-phonon scattering. There experimental details and the results of most widely employed thermal contact resistance measurement methods are discussed. We note that the values of this important physical property, reported by the various methods discussed, vary by more than two orders of magnitude. All the techniques employed in these studies have their short comings. Most of them, in their measurements, mainly relay on heat sources that are not independently characterized. Consequently, there is little consensus on the measured values of thermal contact resistance.

To address this issue we develop a new thermal imaging method, named Electron Thermal Microscopy (EThM), which relies on well studied (and understood) phenomenon of Joule heating in a thin metal wire, as a heat source. The temperature sensors in our technique are nano-meter sized, low but standardized melting point Indium islands. Once the temperature in our samples gets higher than melting temperature of these Indium islands, their melting could be observed in-situ and in real-time. Thus they serve as binary thermometers. This work is published in the

peer-review journal Nano Letters (T. Brintlinger, Y. Qi, **K. H. Baloch**, D. Goldhaber-Gordon, and J. Cumings, Nano Lett., 8(2), 582 (2008))

In chapter 5 we employ EThM to measure the thermal contact resistance by directly and find the value to be surprisingly high. We however, demonstrate that this high contact resistance is not a limiting factor in nanotube devices. We can control and thus reduce the inherently high thermal contact resistance of a nanotube on a substrate by almost two orders of magnitude. This work is published in the peer-reviewed Journal Applied Physics Letters (**K. H. Baloch**, N. Voskanian, J. Cumings, App. Phys. Lett. 97, 063105 (2010))

In the last chapter, we present data of ongoing work in which we study the thermal behavior of a biased carbon nanotube. There we make another interesting observation; as the current is passed through carbon nanotube, the nanotube itself remain cold but the substrate gets hot. We conclude this dissertation by suggesting that this observation of substrate getting hot while the nanotube does not could be a signature of remote electron-phonon scattering; in which hot electrons in the nanotube can scatter off the phonons in the substrate. The manuscript on this work is in preparation.

We have chosen the format of the dissertation such that the contents, list of figures and acronyms are at the beginning whereas the references for each chapter appear at the end of that chapter.

Dedication

To Mumtaz Zahra

my dearest sister and my friend

Acknowledgements

Many people have played a significant role in my life and helped me in shaping the person I am today. It will not be possible to acknowledge everyone here.

I will start by thanking my dearest sister Mumtaz Zahra Baloch for her love, care and support throughout my life. She has guided, motivated and inspired me all along. She has always encouraged me in all my pursuits and decisions. I am so thankful for her being a sister and a friend. I wish her all the best.

I must thank my advisor Dr. John Cumings who is not just a remarkable scientist but also an exceptional advisor and mentor. I appreciate his hands-on approach in research and his availability to his students even at odd hours. He has always shown faith in my abilities and encouraged me at every step. I am indebted to all other members of my thesis committee for spending time to read this thesis. Additionally, I thank Dr. Greene for his feed-back on the presentations that I gave in his seminar classes; Dr. Fuhrer for reading and editing my candidacy paper and letting me use his labs for lithography; Dr. Ouyang for his guidance and witty and humorous remarks passed in physics corridors; Dr. Salamanca-Riba for letting me sit through her TEM class. Her knowledge about TEM is remarkable.

I will like to thank all of my professors at Maryland and the institutions I attended prior to coming here. I will not be able to name all of them here. But I will like to acknowledge Dr. Ismat Shah, Dr. Mariana Safronova, Dr. Valeria Gabriela Stoleru and Dr. Coplan for their guidance and support.

I will like to thank all the staff in the IPST and Materials Science department, Fablab, NISP lab and Physics machine shop.

This dissertation would not have been possible without the help of my friends both in the lab and outside. I should thank all the present and past members in the Cumings group; Dr. Todd Brintlinger (now at NRL), Dr. Yi Qi (now at Princeton), Colin Heikes (now at Cornell), and Dr. Hongwei Liao. I want to specially thank Stephen Daunhiemer, for his unconditional support, collaboration and constructive feedbacks; Paris Alexander for her intelligence, genuineness and sincerity that always inspire me. I always value her advice for my research projects; Norvik Voskanian, for being an exceptional collaborator and a friend. I am thankful to him for constantly reminding me to be in shape and arranging all the soccer games. Khim Karki for his intelligent discussions related to research, and for introducing me to Nepali culture and cuisine; Eric Epstein, for being a genuine friend. My long discussions with him have been very enlightening. His intelligence inspires me. Many thanks to newer members of Cumings group i.e. Elizabeth Messina, John Bavier. I am also grateful for the friendship of Adrian Southard, Brooke Hester, Dan Lenski, Enrique Cobas, Arun Luykx and Dwight Hunter. I will miss them dearly. There is so much I want to say to them but the lack of space here does not permit me.

I thank my parents for bringing me into this world. They have done their best in raising me. I hope that I have and will continue to make them proud. My father, especially, has been a great mentor and a friend. He is a truly exceptional man with unbelievable strength, courage and optimism. I am so very proud and thankful to all my sisters who have always made me feel special by their unconditional love and care. I am aware that my success and happiness means the world to them. Completion of this PhD is as much a result of their efforts as it is of mine. I am indebted to my

brother who has always loved me like his own son. He, just like my parents and sisters, is a great role model. I would also like to thank all my friends in Pakistan and elsewhere for their love, understanding and support. The self-confidence that I have is as much because of the support and confidence of my family and friends as it is because of the encouragement of my professors. It is sad that some, including my grandparents, who dreamed of this day long before I started attending graduate school, are not there to see me graduate with a PhD degree. My late friend, Saeed Ahmad needs special mention here. His untimely death was tragic. He will never be forgotten.

I thank God for blessing me with my sweetest and most wonderful daughter Sakina. She is the most important person in my life. She is my pride and the source of my strength.

I have spent five most wonderful and productive years of my life at this University. Not only have I worked hard to contribute to Physics, I have grown tremendously as a person here. It is an extraordinary school and truly attracts some of the finest minds from across the world. My interaction with faculty and students here has opened my mind and broadened my horizons. Even as it is difficult to say goodbye, I leave with a sense of accomplishment and gratitude for everyone who made this day possible.

Contents

List of Figures

Chapter 1

Introduction to Carbon Nanotubes

1.1 Discovery

Evidence of the existence of carbon nanotubes (CNTs) of about 50 nm can be traced back to as far as 1952 by revisiting the TEM images of carbon fibers published by Russian scientists Radushkevich and Luckyanovich, in Russian Journal of Physical Chemistry (1.1). Because of the unavailability of the aforementioned paper in English, lack of any preparation recipe, theoretical framework or knowledge about their tremendous potential, the CNTs remained unnoticed. After the breakthrough work of late 70's and 80's on C_{60}, CNTs were talked of as being a possibility in conference proceedings. However, it was not until the publication of S. Iijima's famous paper in which he identified multiwalled carbon nanotubes using a transmission electron microscope (TEM) (1.2), did they catch the unprecedented attention of the scientific community. After the initial efforts on preparation of CNTs by various methods, focus soon turned to their characterization and it did not take long for investigators to judge their tremendous potential. For almost two decades now, a great deal of effort has been spent to understand their electrical, mechanical and thermal properties.

1.2 Morphology of Nanotubes

The initial theoretical framework on the structure of CNTs which is essential for understanding their electronic and vibrational properties was laid down in papers by Saito *et. al.*(1.3), Hamada *et. al.*(1.4), and Mintmire *et. al.* (1.5). The morphology of CNTs is briefly discussed below and the electronic and thermal properties will be discussed in chapter 2.

1.2.1 Bonding

A CNT can be considered as a cylindrical structure formed by rolling a graphene sheet onto itself. A graphene sheet is composed of sp^2 hybridized carbon atoms which have atomic number 6 and the electronic configuration $1s^2\ 2s^2 2p^2$. This hybridization of *s* and *p* orbitals results in three in-plane sp^2 orbitals and one *p* orbital, oriented at 90° to the plane containing the sp^2 orbitals. Consequently, each carbon atom is covalently bonded (through σ bonds) to three other in-plane carbon atoms; such that the angle between two adjacent σ bonds is $120°$. Thus a graphene sheet is composed of covalently bonded carbon atoms arranged at the corners of imaginary hexagons.

1.2.2 Structure

The structure of CNTs can be specified by defining a vector $\bar{C}$, obtained by joining two equivalent points on a graphene lattice by two non-orthogonal basis vectors $\overline{a_1}$ and $\overline{a_2}$. The vector $\bar{C}$ is expressed as

$$\bar{C} = n\overline{a_1} + m\overline{a_2} \qquad (1)$$

where n and m are integers and conventionally, $n \geq m \geq 0$. The geometry of a nanotube can be completely specified by translation vector $\bar{C}$.

The diameter (d_t) of a CNT tube is given as:

$$d_t = \frac{\sqrt{|\bar{C}|^2}}{\pi} = \sqrt{n^2 + m^2 + nm}\frac{|\bar{a}|^2}{\pi} \quad (2)$$

where $|\overline{a_1}| = |\overline{a_2}| = 0.246°A$.

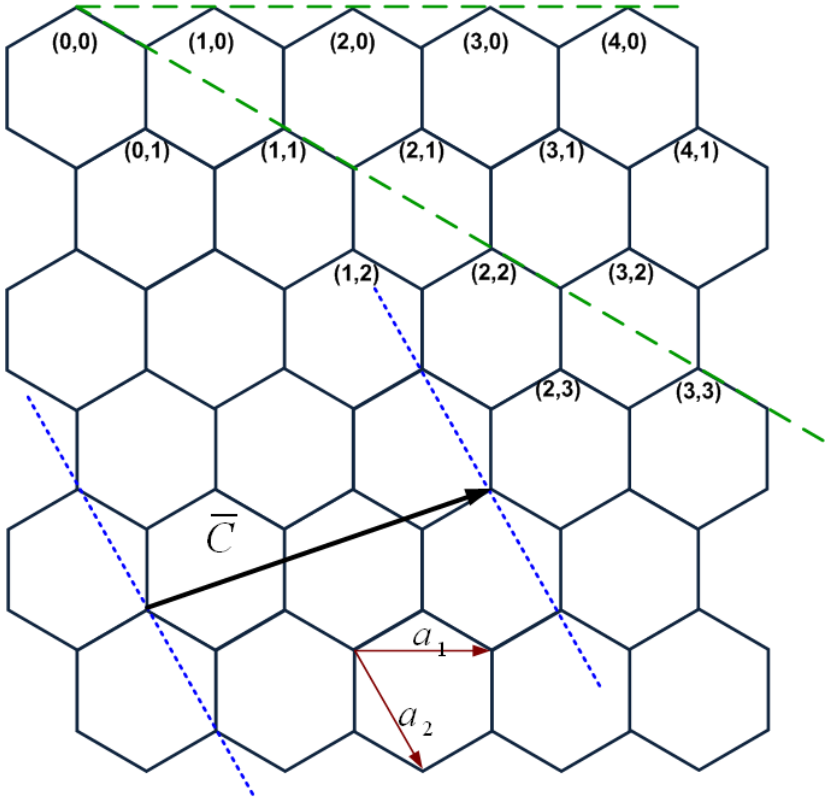

Figure 1.1 Schematic of the honey-comb graphene lattice. Such a graphene sheet can be rolled in arm-chair or zig-zag manner to form a CNT.

Depending on the arrangement of hexagonal structures around its circumference, CNTs can be characterized into three divisions;

- All $(n, 0)$ nanotubes are zig-zag.
- All $(n = m)$; (n, n) nanotubes are arm-chair, and

- The rest when $m \neq 0$, and $n \neq m$ the nanotubes are called chiral CNTs.

1.2.3 Layer structure in MWCNTs

A MWCNT is comprised of several concentric rolled graphene sheets. The diameters of two successive layers of a MWCNT differ by$3.4\ \overset{o}{A}$.

The arrangement of the layers of MWCNTs can be “scroll-like” or “concentric cylinders” or a combination of both. It is not feasible to have MWCNT made up of concentric cylinders of individual zig-zag tubular structures but they can be formed by concentric arm-chair tubes. The arrangement becomes complicated for chiral tubes as the likelihood of two consecutive walls having same chirality is rather low. High resolution TEM images of MWCNTs are shown in Figures 1.3 and 1.5. The reason a MWCNT appears as a set of parallel lines separated by an empty region in these images is that the scattering occurs most strongly when the electron beam is perpendicular to the vectors defining carbon planes.

1.3 Preparation

While several methods have been proposed for the growth of CNTs (1.6-1.8), the two most common methods presently employed are the chemical vapor deposition (CVD) method to grow SWCNTs (1.7), and the arc-discharge method for the growth of MWCNTs (1.8). The typical diameter ranges for SWCNTs and MWCNTs are 0.7-1.6nm and 10-20nm respectively and they can be up to several centimeters long (1.9). These two most widely employed methods are described below:

1.3.1 Arc-discharge /Arc-evaporation Method

The arc-discharge method used today for the synthesis of CNTs is not much different from the method employed by Kratschmer *et. al*. for the production of C_{60} in 1980's (1.8).

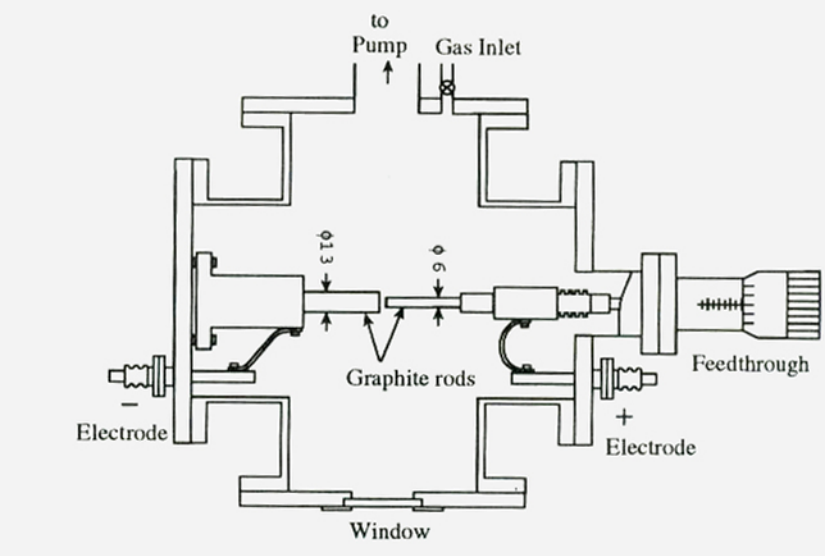

Figure 1.2 Schematic of a typical arc-discharge set-up. An arc-discharge takes place when the moveable anode comes in close proximity of the cathode. A constant gas pressure of He is maintained during the growth process. (Figure 5.3 of "Carbon Nanotubes: Synthesis, Structure, Properties, and Applications", M. S. Dresselhaus *et al* eds., Springer-Verlag (2000); ISBN 3-54041-086-4)

Briefly, in this method, a moveable anode made up of graphite is brought closer to a stationary graphitic cathode such that a stable electric-discharge can be maintained. The typical separation of the electrodes in the process is ~ 1 mm. The arc-discharge is traditionally carried out at about 20 *V*. During this process a static base pressure is maintained by continuously pumping out and injecting an inert gas

(usually helium (He)). While the optimal current depends upon various factors such as the diameter and separation of the electrodes, gas pressure etc., it is typically in the 50-100A range. As a result of arcing, the carbon in the graphitic anode evaporates and condenses on the cathode in the form of a soot that contains MWCNTs. The efficient cooling of the cathode is essential for the production of good quality CNTs. The schematic of the apparatus used for arc-discharge synthesis is shown in the Figure 1.2.

1.3.1.1 Factors for good yield and high quality

Initially the yield was low (1.10) but T. Ebbesen and P. Ajayan in 1992, found that it could be increased significantly by increasing the pressure of He in the chamber (1.11, 1.12). The gas pressure of 500 Torr is more or less optimal. If the pressure is below this value both yield and quality of the CNTs produced is low, whereas if the pressure is increased above 500 Torr their yield goes down without any improvement to their quality (1.13).

The current across the electrodes can affect the quality of the nanotubes produced as well (1.14, 1.15). Low current is generally preferable as long as stable plasma can be generated across the electrodes. At high current fewer CNTs are produced and instead a hard sintered material grows on the cathode.

1.3.1.2 Developments in Arc-evaporation

Many developments have taken place since early days of the production of CNTs. CNTs can be grown by purging the arc-discharge chamber by several other

gases like H_2 (1.16-1.18), CF_4 (1.19), or organic vapor (1.20), N_2 (1.21) without having much effect on yield or quality. Additionally, it has been shown that MWCNTs can be produced in liquids as well (1.22-1.28).

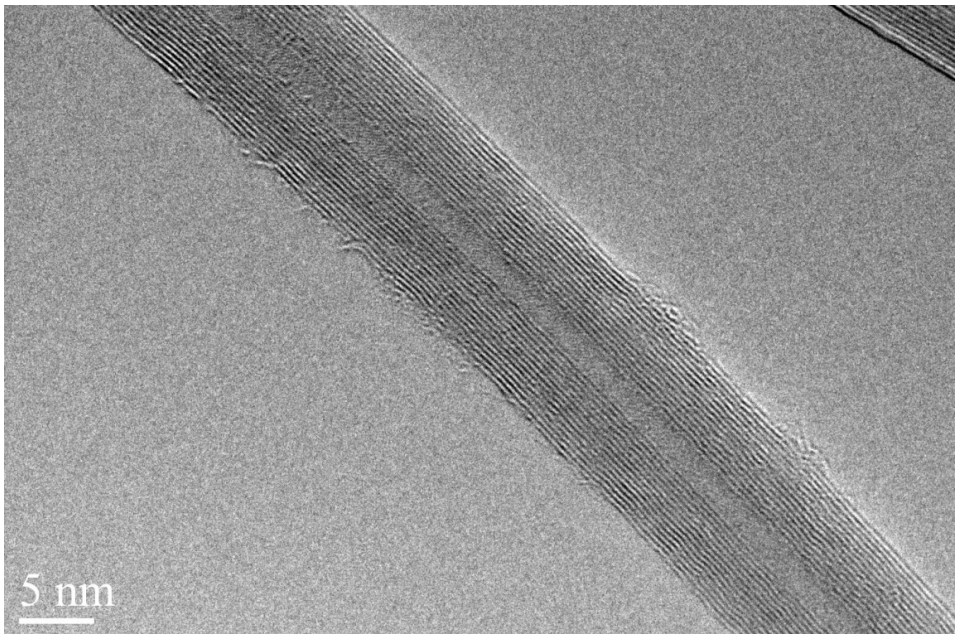

Figure 1.3. A high reolution TEM image of arc-discharge grown MWCNT, obtained from Sigma-Aldrich Inc.

MWCNTs can also be produced by using another method called chemical vapor deposition (CVD) described below.

1.3.2 Chemical Vapor Deposition (CVD) Method

In this process, the growth of nanotubes is assisted by a metallic catalyst. This is neither a new concept nor is limited exclusively to the growth of CNTs. CVD was widely employed before Baker *et. al.* studied the growth of Carbon filaments by this process.(1.21). In 1993 Jose-Yacaman *et. al.* was the first to grow single walled CNTs by this method (1.22). The basics of this process are described below:

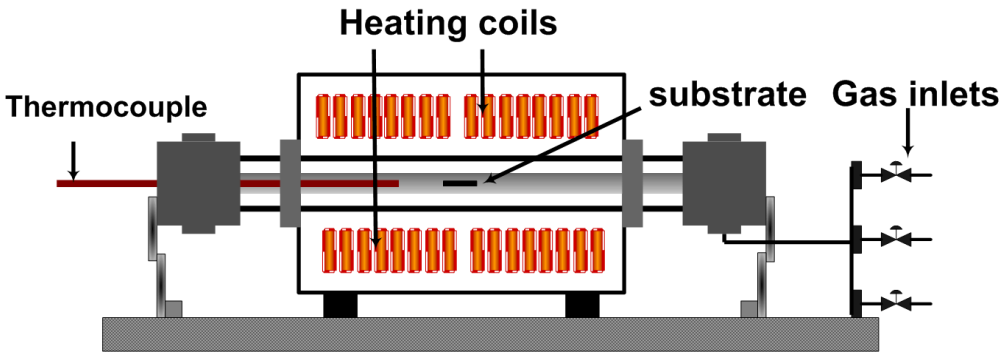

Figure 1.4 Schematic of CVD chamber typically used for CNT growth. The hydrocarbons and the inert gas (Ar) are introduced into the chamber, equipped with heating coils and a thermocouple. CNTs grow onto the substrate in the presence of a metallic catalyst.

In CVD, hydrocarbons, typically ethylene or acetylene, along with an inert gas usually argon, are injected into a chamber having a built-in furnace and a thermocouple to measure the temperature. At temperatures ranging between 550 ^{o}C and 750 ^{o}C, these hydrocarbons decompose in the presence of a catalyst such as iron, nickel or cobalt. Due to its low solubility in the catalytic metals at such high temperatures, carbon precipitates and forms CNTs since under such conditions this is the minimum energy configuration.

For the research described in this dissertation we do not grow MWCNTs in our lab. Instead they are purchased from commercial vendors; such as Sigma-Aldrich. TEM structural characterization of arc-discharge (shown in Figures 1.3) and CVD grown (shown in Figure 1.5) MWCNTs showed that, in general, the ones grown by arc-discharge have fewer defects and thus are of superior quality.

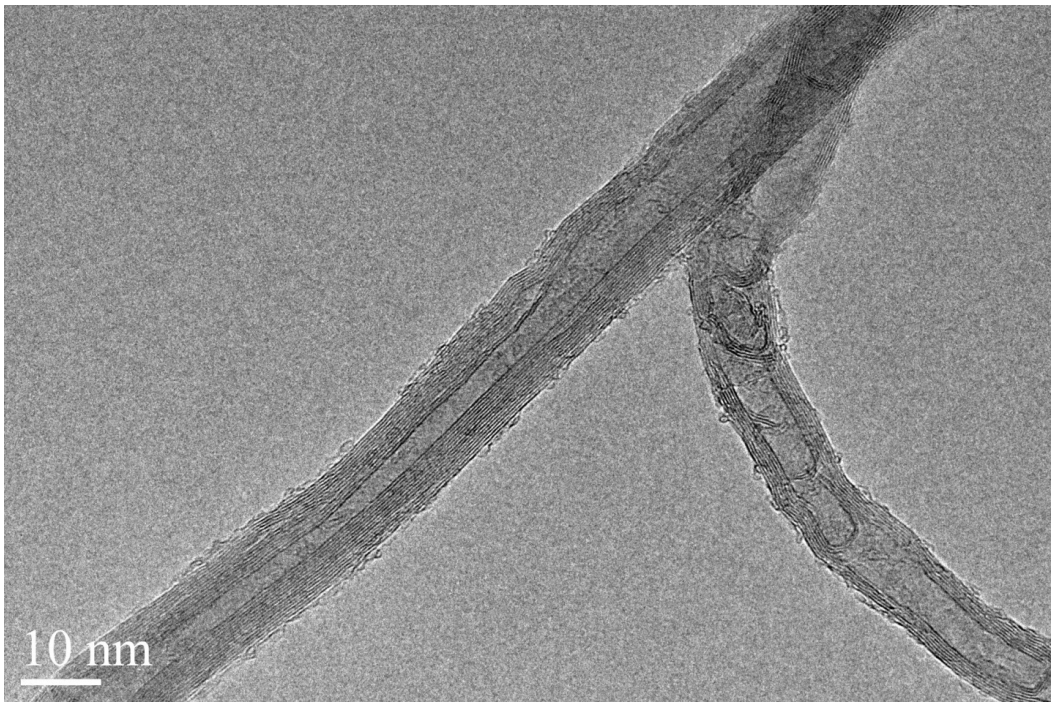

Figure 1.5 High resolution TEM image of two CVD grown MWCNTs purchased from Sigma-Aldrich. A comparison with Figure 1.3 readily shows that arc-discharge process gives higher quality MWCNTs.

References

1.1 Radushkevich L.V., Lukyanovich V.M., Zurn Fisic Chim. 24, 111, (1952)

1.2 S. Ijima. Nature, 354, 56 (1991)

1.3 R. Saito, M. Fujita, G. Dresselhaus, M. S. Dresselhaus, Appl. Phys. Lett. 60, 18, 6951 (1992)

1.4 N. Hamada, S, Sawada and A. Oshiyama, Phys. Rev. Lett., 68, 10, 1579 (1992)

1.5 J. W. Mintmire, B. I. Dunlap, C. T. White, Phys. Rev. Lett. 68, 5, 631 (1992)

1.6 T. Guo, P. Nikolaev, A. Rinzler, D. Tomanek, D. Colbet and R. Smalley, J. Phys. Chem. 99, 10694 (1995)

1.7 M. Jose-Yacaman, M. Miki-Yoshida, L. Rendon And J. G. Santiesteban, Appl. Phys. Lett. 62 657 (1993)

1.8 W. Kratschmer, L. Lamb, K. Foristopoulos and D. Huffman, Nature 347, 354 (1990)

1.9 X. Wang, Q. Li, J. Xie, Z. Jin, J. Wang, Y. Li, K. Jiang and S. Fan, Nano Lett. 9, 9 3137 (2009)

1.10 T. W. Ebbesen, Carbon Nanotubes, Ann. Rev. Mater. Sci. , 24, 235 (1994)

1.11 T. W. Ebbesen, Carbon Nanotubes: Preparation and Properties, ed. T. W. Ebbesen, CRC Press, Boca Raton, 1997, p139

1.12 T. W. Ebbesen and P. M. Ajayyan, 358, 220 (1992)

1.13 T. W. Ebbesen, H. Hiura, J. Fujita et. al., Chem. Phys. Lett., 209, 83 (1993)

1.14 G.H. Taylor et. al., Cathode deposits in fullerene formation- microstructural evidence for independent pathways of pyrolytic carbon and nanobody formation, J. Cryst. Growth, 135, 157 (1994)

1.15 X. Zho et. al., Preparation of high grade carbon nanotubes by hydrogen arc discharge, Carbon, 35, 775 (1994)

1.16 X. K. Wang et. al., Carbon nanotubes synthesized in a hydrogen arc discharge, Appl. Phys. Lett., 66, 2430, (1995)

1.17 L. C. Qin, et. al. The smallest carbon nanotube, Nature, 408, 50 (2000)

1.18 H. Yokomichi, et. al. Synthesis of carbon nanotubes by arc discharge in CF_4 gas atmosphere, Jpn. J. Appl. Phys., 37, 6492 (1998)

1.19 K. Shimotani et. al., New synthesis of multi-walled carbon nanotubes using an arc discharge technique under organic molecular atmospheres, Appl. Phys. A, 73, 451 (2001)

1.20 S. Cui et. al., Investigation on preparation of multiwalled carbon nanotubes by DC arc discharge under N_2 atmosphere, Carbon, 42, 931 (2004)

1.21 M. Ishigami et. al. A simple method for the continuous production of carbon nanotubes, Chem. Phys. Lett. 319, 457 (2000)

1.22 H. W. Zhu et. al., Formation of carbon nanotubes in water by the electric-arc technique, Chem. Phys. Lett., 366, 664 (2002)

1.23 X. S. Li et. al., High-yield synthesis of multiwalled carbon nanotubes by water-protected arc discharge method, Carbon 41, 1664 (2003)

1.24 N. Sano et. al., Pressure effects on nanotubes formation using submerged arc in water method, Chem. Phys. Lett., 378, 29 (2003)

1.25 I. Alexandrou et. al., Structure of carbon onions and nanotubes formed by arc in liquids, J. Chem. Phys., 120, 1055 (2004)

1.26 N. Sano, Synthesis of carbon onions in water, Nature, 414, 506 (2001)

1.27 R.T.K. Baker and P.S. Harris Chemistry and Physics of Carbon, Marcel Dekker, Inc., New York pp. 83–165 (1998)

Chapter 2

Electrical and Thermal Properties of Carbon Nanotubes

2.1 Electronic Properties

2.1.1Electronic Band Structure

The basics of electronic structure of a CNT can be understood by considering it as a rolled graphene sheet. A unit cell of graphene has two atoms. Thus, there are four valence (three σ and one π) bonds. Due to the overlap between wave-functions of adjacent atoms, the graphene has high in-plane mobility. The dispersion relation of 2-D graphene is calculated to be (2.1),

$$E(k_x, k_y) = \pm\gamma_O\{1 + 4\cos\left(\frac{\sqrt{3}k_x a}{2}\right)\cos\left(\frac{\sqrt{3}k_y a}{2}\right) + 4cos^2(\frac{\sqrt{3}k_y a}{2})\}^{1/2} \qquad (2.1)$$

k_x and k_y are two components of the wave-vector.

γ_O is the nearest neighbor coupling constant, while a is in-plane lattice parameter. The $\pm$ signs in equation (2.1) correspond to anti-bonding and bonding of π bonds. At zero *K*, all the bonding π orbitals are completely filled and all the anti-bonding π orbitals are completely empty.

The rolling of a graphene sheet into a nanotube results in the quantization of the reciprocal-space vectors in the circumferential direction. When these quantized

allowed wave-vectors are plotted on to the Brillion-Zone (B.Z.), we get a series of parallel lines separated by

$$\Delta k = \frac{2}{d_t}, \tag{2.2}$$

where, d_t is the nanotube diameter.

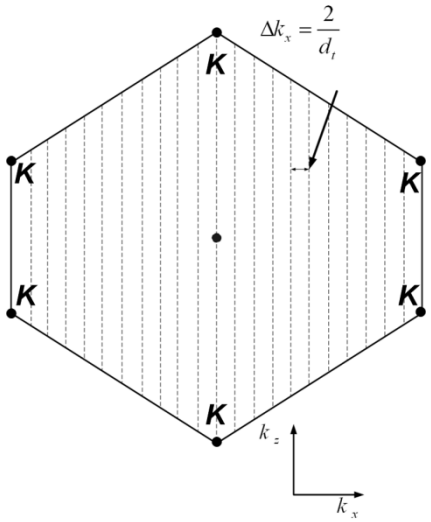

Figure 2.1 Linear sub-band structure of a (10, 10) nanotube. Rolling a graphene sheet into a CNT results in quantization of the wave-vector.

Length, orientation and spacing of these parallel lines are determined by the chilarity of the CNT. The valence and conduction bands of graphene cross at K point of the B.Z. For a nanotube, if this K point is an allowed state i.e. if the allowed wave-vector lines pass through it, the tube will be metallic. Otherwise the nanotube will have a finite band-gap which will make it a semiconductor.

Since the quantization condition requires that

$$\bar{k} \cdot \bar{C} = 2\pi l, \quad \text{where } l \text{ is an integer} \tag{2.3}$$

and K point for graphene is located at $\frac{1}{3}(\overline{k_1} - \overline{k_2})$, the following can be concluded:

- CNT is metallic if $n - m = 3l$

- CNT is semiconducting, having a moderate band-gap of $\sim 1eV$, if $n - m \neq 3l$

Therefore, the geometry of CNTs directly influences their band-structure. Additionally, the metallic nanotubes can develop a small bandgap for $l \neq 0$ as described below.

2.1.2 Effect of curvature

It is expected that for small diameter CNTs the curvature may add some sp^3 character to the bonding (2.2, 2.3) which will result in arm-chair CNTs (n= m) to be metallic in nature. In that case, even though the curvature shifts the Fermi-vector from K point, it remains on the allowed wave-vector lines on the B.Z. Whereas in case of non arm-chair nanotubes the curvature can change the band structure significantly. This will make the Fermi-wave vector move away from the K point, resulting in semiconducting CNTs.

From this it can be shown that if $n - m = 3l$, the CNT will be a semi-metal having a small band-gap of less than 0.1 eV for $l \neq 0$. However, this effect is negligible for CNTs with $d_t > 20nm$. Thus MWCNTs we employed in our studies are considered to be metallic in nature.

2.2 Measured Electrical Properties of MWCNT

Many experiments have been performed to understand the electrical properties of CNTs and much interesting physics of these 1-d materials has come to light. Here we list a few of their electrical properties:

Electronic transport in a CNT can be both ballistic (2.4) and diffusive (2.5). Various electronic devices such as p-type as well as n-type field effect transistors (FETs) (2.6-2.9), logic devices (2.9, 2.10), diodes and invertors (2.10, 2.11), single electron transistors (SETs) (2.12-2.14) made by employing CNTs have all been realized. CNTs can sustain supercurrents (2.15, 2.16), and their electronic properties can be altered from being semiconducting to metallic (and vice versa) by mechanically straining the CNTs (2.17)

In biased metallic MWCNTs the current primarily flows in the outermost shell due to the shell's direct contact with the electrodes. However, it has been demonstrated that inner shells of a biased metallic MWCNT conduct as well (2.18).

In spite of all the developments in the field, not much is known about the interaction of CNTs with the substrate. If they are to be employed in future electronics, it is essential to understand how the substrate can affect their electrical properties. This aspect will be explored in chapter 6 of this dissertation, which deals with the study of CNTs under high bias.

2.3 Thermal Properties of CNTs

2.3.1 Theory: Thermal Conductivity

At moderate temperatures the thermal conductivity of carbon-based materials, namely diamond and in-plane graphite, is higher than that of any other known material (2.19). Unlike metals, the thermal transport in these materials is primarily carried out by phonons instead of electrons and thus Wiedemann-Franz law $\kappa/_{\sigma T} \approx 2.45 \times 10^{-8} (VK^{-1})^2$ does not hold (2.20).

The thermal conductivity tensor of carbon-based materials can be calculated by assuming that the scattering time is constant (2.21). Its diagonal term is given by the following equation:

$$\kappa_{zz} = \sum C v_z{}^2 \tau \qquad (2.4)$$

where C, v and τ are specific heat, group velocity and relaxation time corresponding to a given phonon state. The sum is over all such phonon states. The constant scattering time approximation is most valid at low temperatures ($T < \theta_D/10$, θ_D being the Debye Temperature). At higher temperatures, however, Umklapp scattering is the dominant contributor to τ.

The main contribution to the thermal conductivity (κ) of carbon-based materials comes from the states which have highest v and τ. That is why the thermal conductivity of graphite can be approximated by that of its a-b plane. Since the inter-planar coupling is weak, its contribution to κ can be ignored. It is tempting to assume that κ of the SWCNTs and MWCNTs would have the same temperature dependence as the graphene sheets (in case of SWCNTs) or that of constituent tubes (in case of MWCNTs). However, building of SWCNTs from graphene sheets and MWCNTs from individual tubes may perturb the magnitude as well as the temperature dependence of their κ due to the presence of other scattering effects.

Nevertheless, the phonon band structure of nanotubes can be formulated from that of a graphene sheet similar to the electronic band structure by considering the quantization of the circumferential component of the wave vectors of the phonons, breaking the two dimensional B.Z. into linear sub bands (2.22-2.23) as shown previously in the Figure 2.1. Unlike the electronic structure, the chirality of the tube

does not matter for the phonon bandstructure for qualitative purposes. This is due to the low-lying acoustic phonon band of graphene band, which is essentially circularly symmetric about the Γ-point.For nanotubes, the zeroth order sub-band, the one that passes through the center of the B.Z. in Figure 2.1, is the only sub-band for which $\omega \to 0$ as $k_z \to 0$, whereas the rest of the sub-bands have finite minimum cut-off frequencies. For this reason, the only contribution to κ at low temperatures, comes from zeroth order sub-bands. At these temperatures, the contribution of the zeroth order sub-band is predicted to be linear in temperature. The higher-order sub-bands do not contribute because they are not populated at low temperatures. At 30 *K*, when the first sub-band begins to populate, deviation in linearity of κ with temperature is expected. At higher temperature more and more phonon modes start to contribute to this non-linearity. κ is expected to keep increasing with temperature approximately as T^2, reflecting the temperature dependence of 2D heat capacity of graphene and graphite. At higher temperatures it saturates when the Umklapp scattering starts to set-in.

2.4 Thermal Measurements of CNTs

Electrical and mechanical properties of CNTs have been studied extensively for almost two decades now. However, even though their thermal properties like specific heat, thermal conductivity, thermopower etc. are predicted to be quite interesting, they have not been studied in as much detail, partly because of unavailability of suitable techniques. Most of the techniques utilized for these studies, some of which we discuss in chapter 3, are still in the development stage. Additional

difficulties arise from the requirement for such measurements to be reliable even when carried out on an individual CNT level, which can be experimentally challenging.

2.4.1 Bulk measurements

Measurements on highly graphitic materials at low temperatures (< 100 K) show that $\kappa(T) \propto T^{2.3}$ (2.24). However, due to the onset of the phonon-phonon Umklapp scattering above 100K, when the occupation density of high energy phonons increases, $\kappa(T)$ saturates and starts to decrease. In less graphitic samples such a saturation peak at higher temperatures is not observed (2.25).

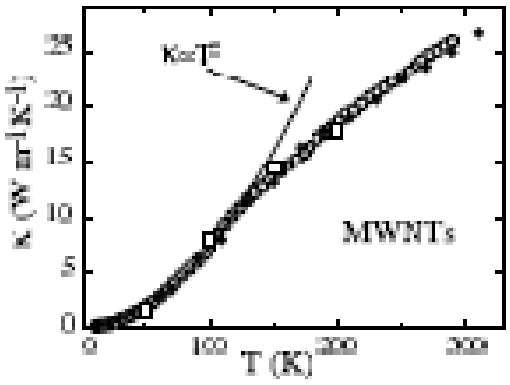

Figure 2.2 The variation of thermal conductivity of a CNT bundle with temperature. (Figure 6 of (2.29)

In the case of CVD grown MWCNT bundles the thermal conductivity shows the expected $\kappa(T) \propto T^2$ behavior at low temperatures (<100K) (2.26) as shown in Figure 2.2, where it can be seen that, just like for less graphitic materials, no

saturation in $\kappa(T)$ is observed. This is due to the fact that near room temperatures grain-boundary scattering, due to small crystallite size, dominate the thermal conductivity.

2.4.2 Individual MWCNT measurements

P. Kim *et. al.* first elaborated the difference between bulk and intrinsic measurements (2.27) in thermal transport measurement of an individual MWCNT. Where Figure 2.3 gives the measured thermal conductance of a single MWCNT, it also shows absence of certain features observed in bulk measurements (inset Figure 2.3).

The lower bound of the intrinsic thermal conductivity was measured to be ~3000 *W/m.K*. While this lower bound is comparable to the theoretical expectations (2.28), it is 15 times higher than measured bulk values (2.29). This suggests that numerous tube-tube junctions present in the bulk are highly resistive and dominate the thermal transport. Some recent measurements have shown that these extra-ordinary thermal conductors can be combined to form thermally insulating mats (2.30). It has also been demonstrated that the thermal conductivity is dependent upon the diameter of the MWCNTs (2.31). Measurements on individual MWCNTs at very high temperatures (>1000 K) show that the they retain their high thermal conductivity at such temperatures (2.32). However, at such high temperatures other modes of heat transfers like thermal radiation may play a role. Since prior studies (2.32) did not account for thermal radiation in their work, their model and conclusion may require modifications.

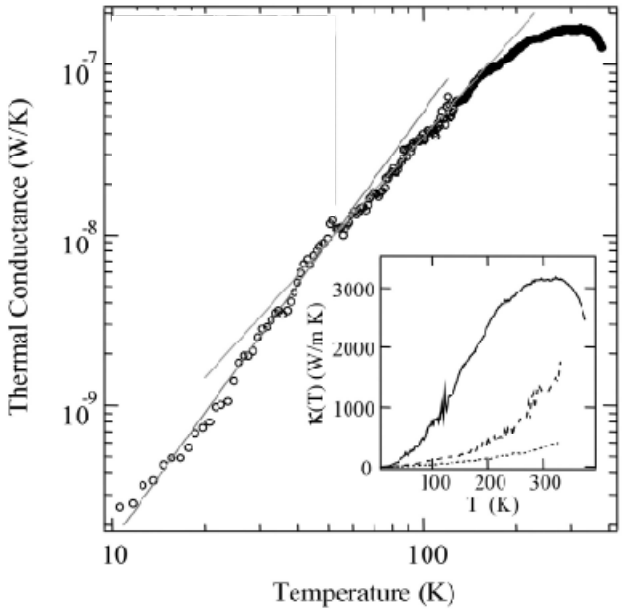

Figure 2.3 Thermal conductance of as suspended individual MWCNT. The linearly fitted experimental data is represented on a on logarithmic scale by two solid lines having slope 2.5 and 2.01. Lower right inset compares the thermal conductivities of the individual suspended MWCNT (solid line) with that of small (d~80 nm) and large (d~200 nm) MWCNT bundles represented with broken and dotted lines respectively. Certain features present in the thermal conductivity curve of the individual nanotube are not present in case of large and small bundles. (Figure 3 of (2.27))

References

2.1 P.R. Wallace. Phys. Rev. 71, 622 (1947)

2.2 X. Blasé, L. X. Benedict, E. L. Shirley. Phys. Rev. Lett. 72, 1878 (1994)

2.3 C.L. Kane and E. J. Mele. Phys. Rev. Lett. 78, 1932 (1997)

2.4 Z. Yao, C. L. Kane, and C. Dekker. Phys. Rev. Lett. 84, 2941 (2000)

2.5 J-Y Park, S. Rosenblatt, Y. Yaish, V. Sazonova, H. Ustunel, S. Braig, T. A. Arias, P. Brouwer and P. L. McEuen, Nano Lett. 4, 517 (2004)

2.6 S. J. Tans, R. M. Verschueren, and C. Dekker. Nature 393, 49 (1998)

2.7 M. Bockrath, J. Hone, A. Zettl, P. L. McEuen, A. G. Rinzler, and R. E. Smalley.Phys. Rev.B 61, 10606 (2000)

2.8 R. Martel, V. Derycke, C. Lavoie, J. Appenzeller, K. K. Chan, J. Terso, and P. Avouris. Phys. Rev. Lett. 8725, 6805 (2001)

2.9 A. Bachtold, P. Hadley, T. Nakanishi, and C. Dekker. Science 294, 1317 (2001)

2.10 V. Derycke, R. Martel, J. Appenzeller, and P. Avouris,Nano Letters 1, 453 (2001)

2.11 C. W. Zhou, J. Kong, E. Yenilmez, and H. J. Dai. Science 290, 1552 (2000)

2.12 S. J. Tans, M. H. Devoret, H. Dai, A. Thess, R. E. Smalley, L. J. Georliga, and C. Dekker. Nature 386, 474 (1997)

2.13 Bockrath, D. H. Cobden, P. L. McEuen, N. G. Chopra, A. Zettl, A. Thess, and R. E. Smalley. Science 275,1922 (1997)

2.14 H. W. C. Postma, T. Teepen, Z. Yao, M. Grifoni, and C. Dekker. Science 293, 76 (2001)

2.15 A. Y. Kasumov, R. Deblock, M. Kociak, B. Reulet, H. Bouchiat, II Khodos, Y. B. Gorbatov, V. T. Volkov, C. Journet, and M. Burghard. Science 284, 1508 (1999)

2.16 A. F. Morpurgo, J. Kong, C. M. Marcus, and H. Dai. Science 286, 263 (1999)

2.17 Tzahi Cohen-Karni , Lior Segev , Onit Srur-Lavi , Sidney R. Cohen & Ernesto Joselevich. Nature Nanotech. 1, 36 - 41 (2006)

2.18 B. Bourlon, C. Miko, L. Forro, D. C. Glattli, and A. Batchtold. Phys. Rev. Lett. 93, 176806 (2004)

2.19 G.W. C. Kaye and T. H. Laby, Tables of Physical and Chemical Constants, 16th ed. Longman, London, (1995)

2.20 J.C. Hones, Studies of 1-D Carbon based Metals: AC_{60} and Carbon Nanotubes, 109 (1998)

2.21 J.C. Hones, Studies of 1-D Carbon based Metals: AC_{60} and Carbon Nanotubes, 111 (1998)

2.22 J. W. Mintmire and C. T. White, Carbon 33, 893-902 (1995)

2.23 N. Hamada, S. Sawada and A. Oshiyama, Phy. Rev. Lett. 68, 1579-1581 (1992)

2.24 J. Heremans, C. P. Beetz Jr.. Phys. Rev. B 32, 1981 (1985)

2.25 M.S. Dresselhaus, G. Dresselhaus, Ph. Avouris (Eds): Cabon Nanotubes, Adv. Topics in Appl. Phys. 88 (2001)

2.26 W. Yi, L. Lu, Z. Dian-lin, Z. W. Pan, S. S. Xie. Phys. Rev. B 59, R9015 (1999)

2.27 P. Kim, L. Shi, A. Majumdar, and P. L. McEuen, Phys. Rev. Lett. 87, 215502 (2001)

2.28 S. Berber, Y. K. Kwon, and D. Tomanek, Phys. Rev. Lett. 84, 4613 (2000)

2.29 E. S. Choi, D. S. Suh, G. T. Kim, D. C. Kim, Y.W. Park,K. Liu, G. Duesberg, and S. Roth, Synth. Met. 103, 2504 (1999)

2.30 R. S. Prasher, X. J. Hu, Y. Chalopin, N. Mingo, K. Lofgreen, S. Volz, F. Cleri, and P. Keblinski

2.31 M. Fujii, X. Zhang, H. Xie, H. Ago, K. Takahashi, T. Ikuta, H. Abe, and T. Shimizu, Phys. Rev. Lett. 95, 065502 (2005)

2.32 G.E. Begtrup, K.G. Ray, B.M. Kessler, T.D. Yuzvinsky, H. Garcia, and A. Zettl, Phys. Rev. Lett. 99, 155901 (2007)

Chapter 3

Thermal Metrology of Nanotubes and Nanostructures

3.1 The Concept of Thermal Boundary Resistance

3.1.1 A brief History

The concept that a thermal boundary resistance (R_b) existed between liquid Helium (He) and a solid interface existed as far back as 1936, but except some sparse mentions by a few scientists that year, it was not explored. Kaptiza, in 1941, was the first to report a temperature drop at such interfaces (3.1). However, it was not until 1952 when a theoretical model (3.2) attributed the temperature discontinuity at the interface measured by Kapitza, to the existence of R_b. $R_b$is defined as the ratio of temperature discontinuity and power flux density across an interface. In later decades, R_b was experimentally noted to have a measureable effect in solid-solid interfaces as well.

3.1.2 Theoretical Models for Thermal Boundary Resistance

The two famous models that estimate $R_b$are described below:

(I) Acoustic Mismatch Model

In acoustic mismatch model (AMM) the phonons in a material are treated as sound waves travelling across the boundary-assumed to be a perfect plane i.e. a plane without any lattice structure. In real systems, this assumption is only valid when wavelength of the phonons propagating from one medium to another (even when the two mediums are of same material) is much larger than the inter-atomic distance of the interface. Only then there would be no interaction between the phonons and the atoms, and thus the phonons (just like photons traveling from one medium at another) could reflect, refract or mode-convert as shown in the Figure 3.1.

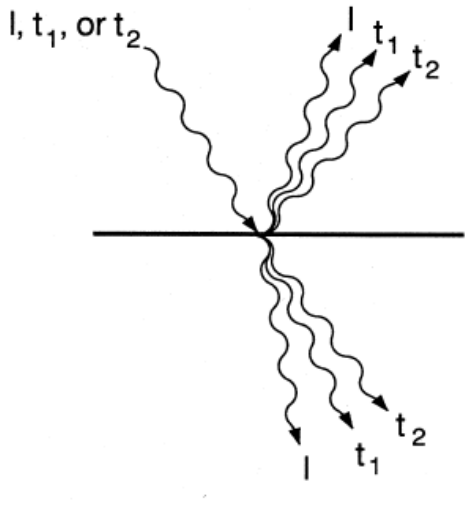

Figure 3.1 The schematic of the ways in which an incident phonon can interact with a plane, under the assumptions of AMM. The l's and t's represent possible longitudinal and transverse polarizations of an incident phonon. (Figure 12 of (3.3))

In AMM there is an equivalent of Snell's law valid for these acoustic phonons, which determines the probability of what mode a particular phonon would have after its incidence on the interface. Additionally, it also gives the angles of

reflection or refraction of these phonons. If a phonon is transmitted through the interface the acoustic Snell's law can be used to determine the angle of transmission as follows:

$$\sin\theta_{transmitted} = \frac{v_j^1}{v_j^2}\sin\theta_{incident} \qquad (1)$$

where v_j^i with $i = 1, 2$ is phonon velocity of j^{th} polarization (longitudinal or transverse) in the respective medium. Analogous to optics, the transmission probability at critical angle for a particular mode is zero and all angles smaller than this critical angle constitute a 'critical cone'. Thus only those phonons whose angles of incidence lie within this critical cone are transmitted. The transmission probability of phonons from one material to the other ($\alpha_{i\to k}, i, k = 1, 2$) in this model is a function of acoustic impedance (Z_i) defined as

$$Z_i = \rho_i v_i \qquad (2)$$

where $\rho_i, v_i$are the mass density and velocity of sound in the i^{th} medium.In this model the $R_b$is explicitly given by

$$R_b = \left[\frac{\pi^2}{15}\frac{{k_B}^4}{\hbar^3}\left[\sum_j v_{i,j}^{-2}\Gamma_{i,j}\right]\right]^{-1} T^{-3} \qquad (3)$$

where k_B is the Boltzmann constant, j is the phonon mode and $\Gamma_{i,j}$is the averaged transmission coefficient over all the phonon modes. The T^{-3} dependence in equation (3) is contributed by the heat capacity. This expression can be approximated as $(\frac{1}{4}Cv\alpha)$ (3.3) where C is the specific heat, v the velocity of sound and α is the transmission probability.

(II) Diffusive Mismatch Model

The primary assumption in diffusive mismatch model (DMM) is that all phonons incident on a boundary interface are diffusively scattered. This means that there is no correlation between the wave vectors of incident and transmitted phonons (except the energy conservation requirement). The probability of scattering of the phonons can be calculated by exploiting Fermi's "golden rule". Thus the transmission probability calculated by DMM model is expected to be a function of velocity and the density of states of the phonons. This model gives the following expression for R_b,

$$R_b = \left[\frac{\pi^2}{15}\frac{{k_B}^4}{\hbar^3}\frac{1}{2}\frac{(\sum_j {v_{i,j}}^{-2})(\sum_j {v_{k,j}}^{-2}}{\sum_{i,j}{v_{i,j}}^{-2}}\right]^{-1} T^{-3} \qquad (4)$$

To avoid any confusion on the use of indices we repeat here that i, k are the medium indices whereas the index j is used for phonon modes. Just as in the case of AMM, the T^{-3} dependence of $R_b$in equation (4) comes from the Debye heat capacity.

3.1.3 Comparison and Limitations of the two Models

Most interestingly, R_b does not vanish at an imaginary boundary (i.e. within a material itself) (3.3), in both models. Additionally, a comparison of equations (3) and (4) reveals that both models predict the same temperature dependence. The AMM model is expected to be more realistic at lower temperatures when the phonon scattering by the lattice of the boundary is negligible. However, at higher temperatures (greater or around Debye temperature) the scattering from the lattice structure at the boundary can no longer be ignored and DMM would be more realistic. The equations (3) & (4) were derived in the low temperature limit.

3.2 Thermal Contact Resistance

The thermal contact resistance (R_c) and R_b have a linear relationship. In case of a CNT resting on a substrate this relation is given by the relation (3.4)

$$R_c = \frac{1}{L}\left[\frac{1}{\pi\kappa_w}\ln\left(\frac{2d}{a}\right) - \frac{1}{\kappa_w} + \frac{1}{\pi\kappa_s}\ln\left(\frac{d}{\pi a}\right) + \frac{R_b}{2a}\right] \quad (5)$$

In equation (5) above κ_w& κ_s are thermal conductivities of the CNT and the substrate, d is the tube diameter, L is its length where as R_b is the thermal boundary resistance.$2a$ is the effective contact width as depicted in Figure 3.2. The experiments that we describe in this dissertation measure R_c.

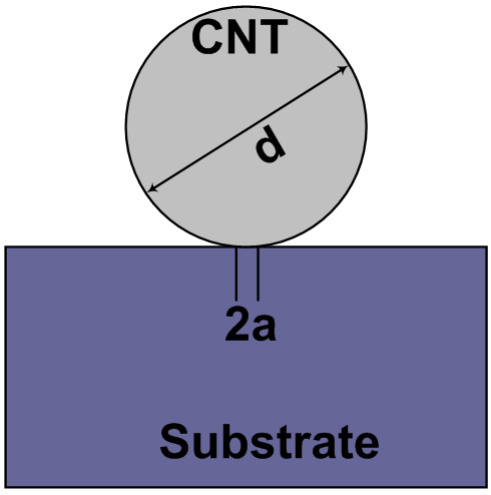

Figure 3.2 Schematic of a CNT resting on a substrate.

3.2.2 Measurements of Thermal Contact Resistance

We briefly discuss the most important methods employed to measure R_c. Here we will only discuss the basics of methods of measurement. The reported values will be summarized at the end of this section.

3.2.2.1 Electrical Break-down Method

A widely employed method to study the thermal properties of CNTs is the electrical break down method. In this method current (I) is passed through metallic CNTs by applying a potential (V) across them. The current through these CNTs increases as the voltage is increased till there is a sudden drop noted in the I-V curve. This sudden drop corresponds to the electrical break down of the CNT. Break down occurs because of the oxidation of the nanotube as it is self-heated. Under ambient conditions, the CNTs burn at 600 ^{o}C (3.5). This serves as one temperature calibration point in these measurements (3.6).

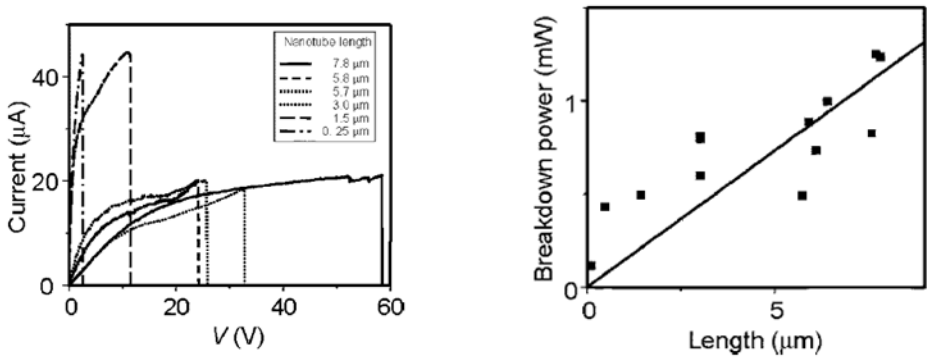

Figure 3.3 Measurement of contact resistance by electrical breakdown of several CNTs on a sapphire substrate. The figure on the left gives the I-V curve (right upto the breakdown of CNTs) for various lengths and the figure on the right is the a plot of the power at which each CNT burns versus its length. The slope of the fitted line is used to calculate the thermal contact resistance. Figures 1 & 2 of (3.6)

Because of dependence of electrical resistance on length of CNT; CNTs of different lengths break down at different applied powers. By observing electrical break down of CNTs of varying lengths a plot of applied power vs their length is obtained an example of which is shown in Figure 3.3 (3.6). The R_c can then calculated from the

slope of the linear fit to such a plot by using the relation $R_c = (\frac{dP}{dL})^{-1} \times \Delta T$, where $(\frac{dP}{dL})$ is the slope of the plot in Figure 3.3 and ΔT is the difference in temperatures of the CNT (600 ^{o}C when it breaks down) and the substrate (20 ^{o}C). The values measured by employing this method are in 0.6-3 m.K/W range (3.6, 3.7).

3.2.2.2 Optical Methods

In optical methods, photons are employed for the thermal characterization of the CNTs. Such techniques rely on inelastic scattering of single-wavelength photons (usually a laser) from the sample of interest. Upon interaction of the photons with the electron cloud in the sample, the electrons are excited into a virtual state. Eventually these electrons de-excite into excited vibrational or rotational states and emit a photon which has lower energy. The loss in energy is the characteristic of the material. This process is called as Raman Scattering (RS). Usually RS gives a weak signal because most photons are Raleigh (elastically) scattered. To circumvent this i.e. to achieve a better signal, the wavelength of the laser could be chosen such that its energy coincides with the excited state of the material of interest.

Hsu et. al.(3.8) measured the ratio (γ) of R_c to the intrinsic thermal resistance of the CNT ($^{\mathrm{CNT}}R_{th} = {\kappa_{CNT}}^{-1}$) by using an optical laser of wavelength 532nm. The diameter of the spot of this laser was ~ 0.36μm. A suspended SWCNT (Figure 3.4 a) was heated along its length by using this laser and a shift in the Raman peak was observed. This shift was due to the temperature increase in CNT at the point where the laser is shone. Functional form of such a change in temperature (Figure 3.4 c) profile along the length of CNT was then used to calculate the ratio γ to be in the

range of 0.02-0.17. While this technique can measure the ratio, γ between $R_c$and $^{CNT}R_{th}$, it unfortunately does not allow direct measurement of the thermal contact resistance, R_c, independently.

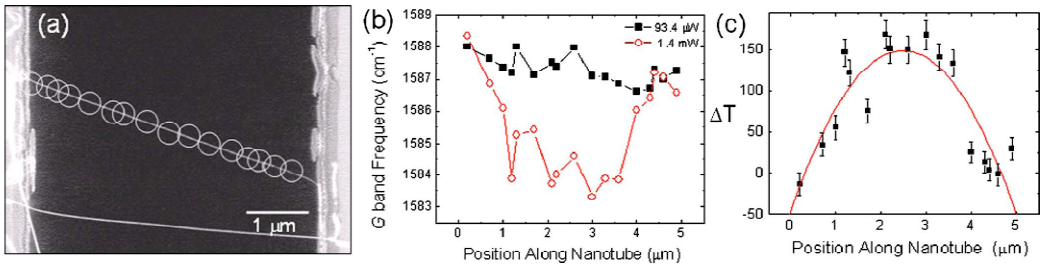

Figure 3.4 Optical measurement of thermal transport in a suspended CNT. (a) An SEM image of the suspended CNT. Circles along the length of the CNT represent the regions where the laser was shone. (b) Raman shift of the CNT along its length. (c) Extracted Temperature information. The red line is the functional fit to the data. Figure 1 of (3.8)

3.2.2.3 Employing Micro-Device

Micro-device comprises of two suspended structures as shown in Figure 3.5. An individual CNT (3.9) or a CNT fiber (3.10) bridges two suspended structures. Each of the suspended structure has a thin Pt resistor which serves dual purposes- as a heat the nanotube by joule heating in Pt resistor and as a themal sensor to measure the resulting temperature change. All the heat transfer between the islands takes place through CNT since the suspended islands are thermally isolated from each other. The thermal conductivity of CNT, κ_{CNT} is estimated by using a simple heat transfer model shown in Figure 3.6 to be,

$$T_h = T_o + \frac{\kappa_d + \kappa_{CNT}}{\kappa_d(\kappa_d + 2\kappa_{CNT})} P, \text{ and} \qquad (6)$$

$$T_s = T_o + \frac{\kappa_{CNT}}{\kappa_d(\kappa_d + 2\kappa_{CNT})} P, \qquad (7)$$

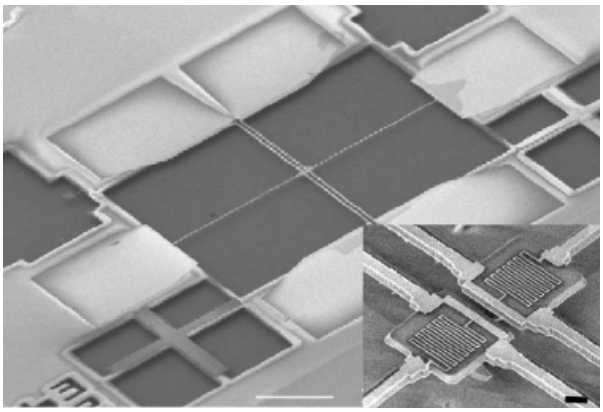

Figure 3.5. A scanning electron microscopy image of the device. Two structures suspended by three sets of silicon nitride beams which are $250\mu m$ long each. Pt lines on each islands, which have a temperature dependent resistance, act as thermometer and heater. The scale bar represents $100\mu m$. Inset is the zoomed-in image of the device. MWCNT bridges the two islands. Figure 1 (a) in (3.9)

where, T_o, is thermal bath temperature, T_h and T_s are the increased temperatures of islands corresponding to resistors R_h and R_s, P is applied Joule power and κ_d is thermal conductance of the suspended beams. The above equations can be solved for κ_{CNT} by determining the slopes of R_h and R_s vs P. Once this is done, R_c can be calculated by using fin hear transfer model (3.11, 3.12) which gives the following expression:

$$R_{cj} = \left[\sqrt{\frac{\kappa_{CNT}A}{R_c'}} \tanh\left(\frac{L_{cj}}{\kappa_{CNT}AR_c'}\right)\right]^{-1} \qquad (8)$$

where R'_{cj}, is the thermal contact resistance at each of the two CNT suspended beam contacts, L_{cj} is the length of CNT at each contact, A is the cross-sectional area and R'_c is the thermal contact resistance per unit length.

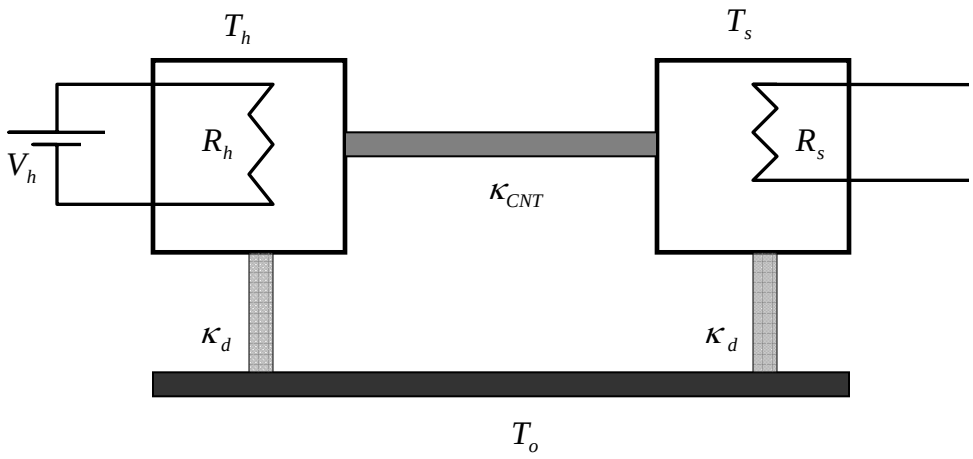

Figure 3.6 Schematic of the heat flow device where T_o, T_h & T_s represent the temperatures of thermal bath, Pt resistors R_h & R_s on the two suspended islands respectively. κ_d is the thermal conductivity of the suspended legs and κ_{CNT} is that of the connecting nanotube.

To measure the contact resistance, Pettes et. al. (3.13) decreased the length of suspended CNT by deposition of Platinum-Carbon (Pt-C) composite using Focused Ion Beam (FIB) deposition at one end of CNT-heater contact. After each such controlled Pt-C deposition, thermal conductance of the CNT was measured. This way a number of thermal conductance values per length were obtained. The comparison of these measured values with the intrinsic thermal conductance (when no Pt-C is deposited) gave the thermal resistance per unit length at the contact (R'_c). Once R'_c is known equation (8) can be readily solved for R_{cj}.

This set-up can be placed in a cryostat and the typical reported values were taken in the temperature range of 8-370K. The R_c values measured for CVD grown CNTs was in the range of 78-585 K.m/W (3.13)

3.2.2.4 Photothermal Current Microscopy

Thermal properties of CNTs have been studied through another novel method known as Photothermal Current Microscopy (PTCM) (3.14). In this method the temperature increase in a gated CNT, due to shining of the laser results in photo thermal current (PTC) through the CNT. This current was measureable in the experimental set-up of Tsen et. al.. Increase in laser power resulted in a linear increase in PTC as shown in Figure 3.7 (b). The direction of the PTC was always opposite to the direction of source-drain current resulting in change in conductance (ΔG). The conductance G measured before shining the laser is plotted in Figure 3.7 (c). This ΔG vs G was fitted and compared with the functional form $\Delta G = \frac{dG}{dT}\Delta T$, from which the ΔT can be calculated. Finally, the thermal contact resistance between the substrate and CNT could be calculated by the relation $R_c = {}^{\Delta T}/_{P}$, where P is the power of the laser. They reported value for this technique is ~25 K.m/W (3.14).

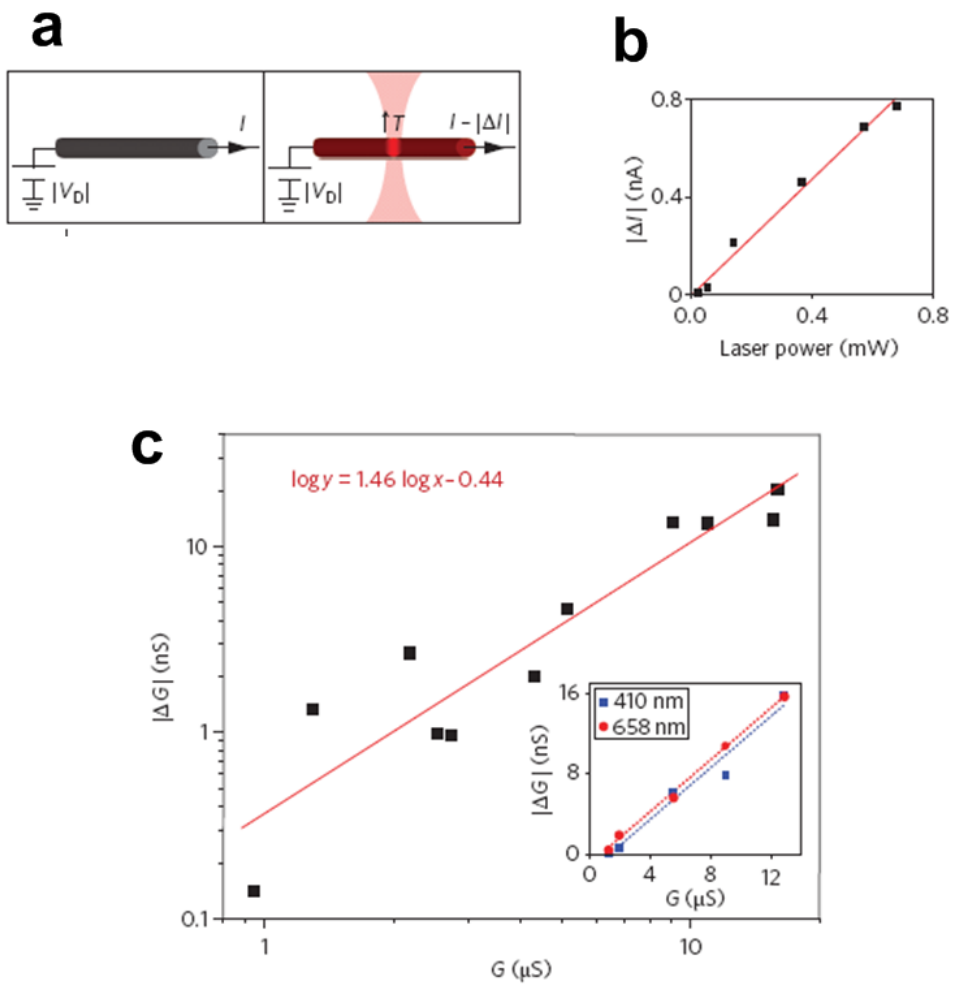

Figure 3.7 The Photothermal Current Microscopy. (a) The conductance of a gated CNT is measured before and after shining the laser. (b) Photothermal current vs Laser power has a linear relationship. This photothermal current is always opposite to the direction of source-drain current. (c) Change in thermal conductance due to photothermal current vs the characteristic conductance of the device. This log-log plot is fitted with linear function to extract the relationship between the rise in temperature resulting from the change in conductance. This Figure is compiled from parts of Figures 1and 2 of (3.14).

3.2.2.5 Scanning Thermal Microscopy

The desire to increase the spatial resolution due to the developments in the field of nano materials led to development of a new thermal imaging technique called

scanning thermal microscopy (SThM) (3.15). SThM raster-scans samples by a temperature sensing tip which is its key element. Attached to the tip is usually a thermocouple junction made up of Platinum (Pt) and Chrome (Cr) because of high difference in their Seebeck coefficients and low thermal conductivities relative to other potential metals or Silicon (Si) and is mounted on a cantilever beam. The force feedback of an atomic force microscope (AFM) maintains a constant tip-sample contact force. As the sample is raster scanned the thermocouple can capture the temperature gradient information by measuring the deflection of the tip by a laser. While the schematic of the cantilever probe is shown in Figure 3.8, the details of this technique are reported elsewhere (3.15, 3.16). It is worth mentioning that SThM is generally operated in contact mode. For this reason contact resistance between the tip of the thermal probe and the sample is generally high to ensure that there is negligible electrical contact between the two. The thermal image thus captured, therefore, results from phonon coupling instead of electron coupling at the sample-tip junction.

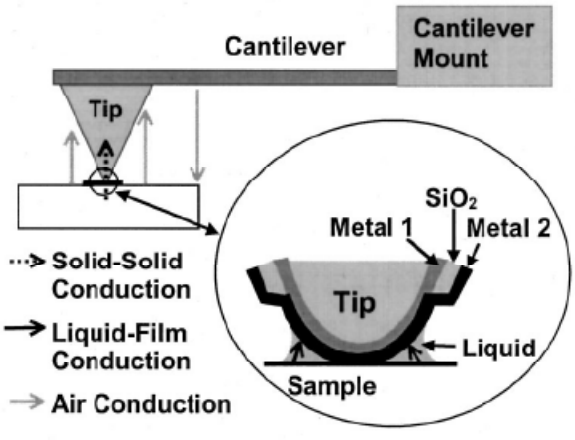

Figure 3.8 Schematic of the tip and the cantilever used in scanning thermal microscopy. Also indicated are the heat transfer mechanisms between the tip and the sample. (Figure 1 in (3.16))

This thermal scanning technique does have a better resolution, but it requires the tip, in the process of raster scanning the sample, to reach thermal equilibrium at each point of contact to give a reliable temperature profile. This makes this technique inherently slow, giving a low temporal resolution. Using this technique Kim *et. al.* reported their measured $R_c$to be 12 m.K/W (3.17).

3.2.3 Summary

The values of R_c measured by employing the methods described above are summarized in the following table 3.1.

Material	R_c	Method	Reference
MWCNT on SiO_2	**0.6 *K.m/W***	Electrical Breakdown	(3.6)
MWCNT on SiO_2	**12 *K.m/W***	Scanning Thermal Microscopy	(3.17)
SWCNT on SiO_2	**25 *K.m/W***	Laser Heating	(3.14)
CVD-MWCNTs Suspended b/w Pt electrodes	**78-585 *K.m/W***	Indirect heating under suspension between a Heater and a Sensor	(3.13)

Table 3.1 Summary of reported $R_c$values

A quick look at the table reveals clearly that the R_c values vary widely and the measurements clearly depend on the method of measurement. For this reason it is important to have an un-ambiguous technique which does not rely on

uncharacterized heat sources. We will develop such a technique in the next chapter and come back to the R_c measurements in chapter 5. Before doing that, we will briefly describe another important concept that will come under discussion in the later parts of this dissertation.

3.3 Remote Electron-Phonon Scattering in Carbon Nanotubes

The thermal transport in a CNT is primarily phonon mediated and the contribution of electrons to its thermal conductivity is believed to be negligible (3.18). However, the coupling of hot electrons in a biased CNT to the phonon modes can lead to interesting phenomenon like negative differential resistance (3.19) and current saturation (3.20). Such electron-phonon coupling (EPC) in CNTs has been extensively studied (3.21).

In addition to a coupling between the electrons and phonons of a CNT, the hot electrons in a biased CNT that rests on a dielectric substrate may also couple with optical phonons of the substrate. This phenomenon, known as remote electron-phonon (REP) scattering, has been experimentally demonstrated to exist in graphene (3.22, 3.23), where such a scattering results in a decrease in mobility of the electrons in graphene.

The polar nature of dielectric substrates causes an electric field to be generated at their surfaces. Just as in case of graphene, the electric field on the surface of the substrate can influence the hot electrons of the CNT which are in close proximity to the substrate as shown in Figure 3.9. Despite having low occupation the surface phonons dominate the carrier mobility because they are more strongly

coupled to the hot electrons and the coupling between the acoustic phonons of a CNT and the electrons is weak under high bias.

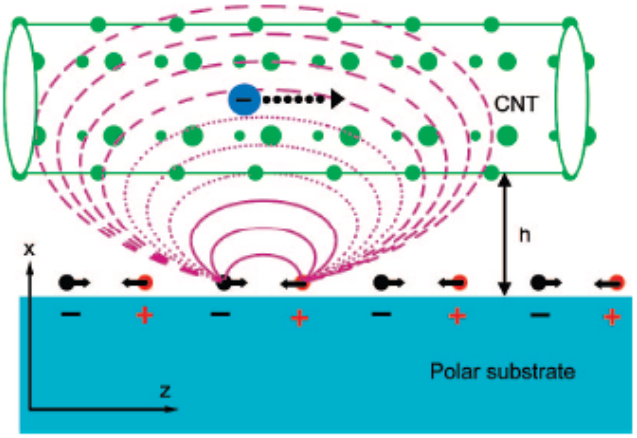

Figure 3. 9 Schematic of Remote electron-phonon scattering in a CNT. The field generated by a dielectric substrate can couple the hot electrons in the CNT to the surface phonons of the substrate. Figure 1 of (3.24)

Surprisingly, in CNTs under high bias, the drift velocity of the carriers can increase due to such EPC (3.24). This effect, among other factors, can depend on the diameter of the CNT and surface roughness of the substrate.

This REP scattering in CNTs has not been explored much experimentally. In chapter 6 of this dissertation we will propose that this phenomenon could explain our most recent data on CNT under high bias.

References

3.1 G. L. Pollack, Rev. of Modern Phys. 41, 1 (1969)

3.2 A. A. Abrikosov and I. M. Khalatnikov Sov. Phys. Usp. 66, 68, (1958)

3.3 T. E. Swartz, R. O. Pohl, Rev. of Mod. Phys. 61, 3, 605-668 (1999)

3.4 R. Prasher, Nano Lett. 5, 2155 (2005)

3.5 P. G. Collins, M. Hersam, M. Arnold, R. Martel, and P. Avouris, Phys. Rev. Lett. 86, 3128 (2001)

3.6 H. Maune, H-Y. Chiu and M. Bockrath. Appl. Phy. Lett. 89, 013109 (2006)

3.7 H. Y. Chiu, V. V. Deshpande, H. W. C. Postma, C. N. Lau, C. Miko, L. Forro, and M. Bockrath, Phys. Rev. Lett. 95, 226101 (2005)

3.8 I-K Hsu, R. Kumar, A. Bushmaker and S. B. Cronin, Appl. Phys. Lett. 92, 063119 (2008)

3.9 P. Kim, L. Shi, A. Majumdar and P. L. McEuen, Phys. Rev. Lett. 87, 21, 215502-1 (2001)

3.10 C. H. Yu, S. Saha, J. H. Zhou, L. Shi, A. M. Cassell, B. A. Cruden, Q. Ngo, J. Li, J. Heat Transfer 128, 234, (2006)

3.11 Prasher, Phys. Rev. B, 77, 075424 (2008)

3.12 C. H. Yu, S. Saha, J. H. Zhou, L. Shi, A. M. Cassell, B. A. Cruden, Q. Ngo, J. Li, J. Heat Transfer 128, 234 (2006)

3.13 M. T. Pettes and L. Shi, Adv. Fun. Mat. 19, 3918 (2009)

3.14 A.W. Tsen, A. K. Donev, H. Kurt, L. H. Herman, J. Park. Nature Nanotech. 2, 108-113 (2008)

3.15 A. Majumdar, Ann. Rev. of Mat. Sci., 29, 505, (1999)

3.16 L. Shi, S. Plyasunov, A. Bachtold, P. L. McEuen, and A. Majumdar, App. Phys. Lett.77, 26, (2000)

3.17 P. Kim,L. Shi, A. Majumdar, P. L. McEuen, Mesoscopic Physica B, 323, 67-70 (2002)

3.18 J. Hone, M. Whitney, C. Piskoti, and A. Zettl, Phys. Rev. B 59, R2514 (1999)

3.19 E. Pop, D. Mann, J. Cao, Q. Wang, K. Goodson, H. Dai, Phys. Rev. Lett. 95, 155505 (2005)

3.20 A. Javey, J. Guo, Q. Wang, M. Lundstrom and H. Dai, Nature 424, 654-657 (2003)

3.21 A. W. Bushmaker, V. V. Deshpande, M. W. Bockrath, and S. B. Cronin. Nano Lett. 7, 12, 3618 (2007)

3.22 J-H. Chen, C. Jang, S. Xiao, M. Ishigami and M. S. Fuhrer, Nature Nanotech., 3, 207, (2008)

3.23 A. M. Dasilva, K. Zou, J. K. Jain, and J. Zhu, Phys. Rev. Lett. PRL 104, 236601 (2010)

3.24 V. Perebeinos, S. V. Rotkin, A. G. Petrov, and P. Avouris, Nano lett. 9, 1, 312 (2009)

Chapter 4

In-Situ Electron Thermal Microscopy: A Novel Thermal Imaging Technique

In this chapter we give a brief introduction to Transmission Electron Microscope (TEM), the modes of its operation and discuss the development of an in-situ thermal imaging technique called Electron Thermal Microscopy (EThM). EThM relies on solid to liquid phase transmission of sub-200nm low melting point Indium (In) islands for thermometry. Due to the presence of a self-passivating layer of robust Indium Oxide (In_2O_3), these In islands retain their shapes when molten. As a result, our samples can be operated over various melting-solidifying cycles of these tiny thermometers. The work on the development of this novel technique is published in the Nano Letters (T. Brintlinger, Y. Qi, **K. H. Baloch**, D. Goldhaber-Gordon, and J. Cumings, Nano Lett., 8(2), 582 (2008)).

4.1 Transmission Electron Microscopy

4.1.1 A Brief History of TEMs

Historically, TEMs were developed to overcome the limitations imposed by the wavelength of the visible-light employed in optical microscopes. In 1932, not

long after de Broglie's proposition of wave-particle duality and Davisson & Germer and Thompson & Reid electron diffraction experiments, Knoll and Ruska demonstrated the concept of electron lenses to be a practical reality. While within a year of the publication of their paper the resolution of an optical microscope was surpassed (4.1), it was not till 1986 was Ernst Ruska awarded a Nobel Prize. Very shortly after the first demonstration of electron lenses the potential of a TEM was realized by the commercial companies. The first commercially available TEM was developed by a British heavy electrical company, Metropolitan-Vickers (Metrovick). Siemens and Halske, however, started regular (relatively) large production of TEMs in 1939. After World War II, several other companies including Jeol, Hitachi and Philips were selling TEMs.

TEMs have come a long way since their early days. Arguably, they now constitute the most versatile, efficient and reliable tool for the characterization of, at the very least, nanoscale samples. They can have resolution of up to the atomic level.

4.1.2 Basics of TEM

A typical TEM can be thought of as comprising of three major components:

i) Illumination system

Illumination system is composed of an electron gun assembly and condenser lenses. The gun assembly has an electron source built within it. These sources produce electrons either by thermionic emission (TE) or field-emission (FE). A TE gun (TEG) comprises of tungsten or Lathanum Borate (LaB_6).

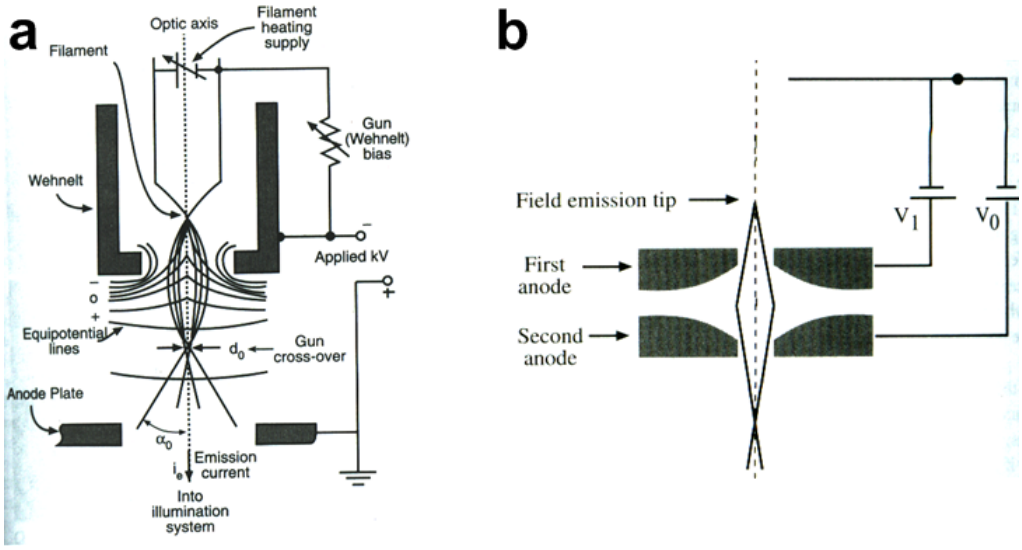

Figure 4.1 Schematics of the gun assemblies conventionally used in a TEM. A gun assembly with (a) thermionic emission source (b) field emission source (Figure 5.1 of (4.1))

Whereas a FE gun (FEG) is generally a thin tungsten wire tip with a radius of less than 0.1 μm. The gun assemblies for the two types of sources are different as shown in Figure 4.1. For routine TEM operation a FEG is a preferred source since it is brightest and most coherent.

The electron beam coming out of the gun assembly passes through two condenser lenses, C1 and C2. C1 forms a demagnified image of the gun whereas, C2 is adjusted to produce an under-focused image of the C1 crossover. The purpose of having condenser lenses is to achieve a parallel beam for sample imaging. Coherence of the beam can be further increased by inserting a condenser aperture in the path of the beam made parallel by the condenser lenses.

ii) Objective Lenses

The Objective lens (OL) is used to form the initial specimen image that can then be magnified by the other lenses. Thus it is of most crucial importance in a TEM design. For high resolution, OL should have short focal length which means that it should be a strong lens. The most streamlined way of achieving this is to have split pole pieces. This way upper and lower pole pieces have separate coils and can be controlled in strength separately. In such geometry the sample is inserted between the pole pieces. The schematic of this is shown in Figure 4.2. The OL set-up extends to less than 1cm in the column. It is responsible for the resolution and quality of the image and is thus fittingly referred to as “heart of a TEM’ (page 132 (4.1))

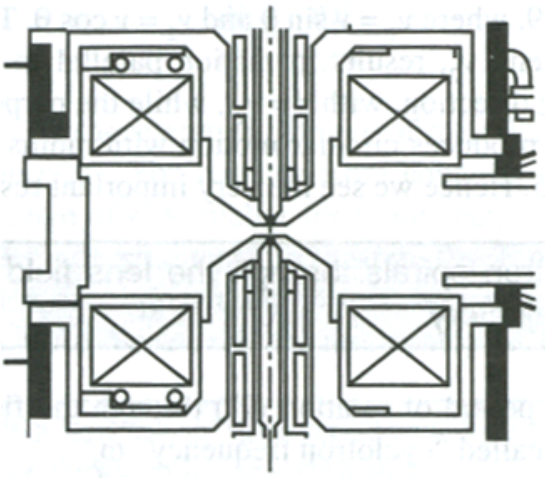

Figure 4.2 Schematic of a “split” OL. The benefit of having such an OL is that the strength of each pole piece can be controlled separately. The sample is inserted between the two poles pieces from the right. (Figure 6.8 (A) of (4.1))

iii) Imaging system

The imaging system is composed of magnifying lenses (referred to as intermediate lenses (ILs)), used to magnify the image or the diffraction pattern made

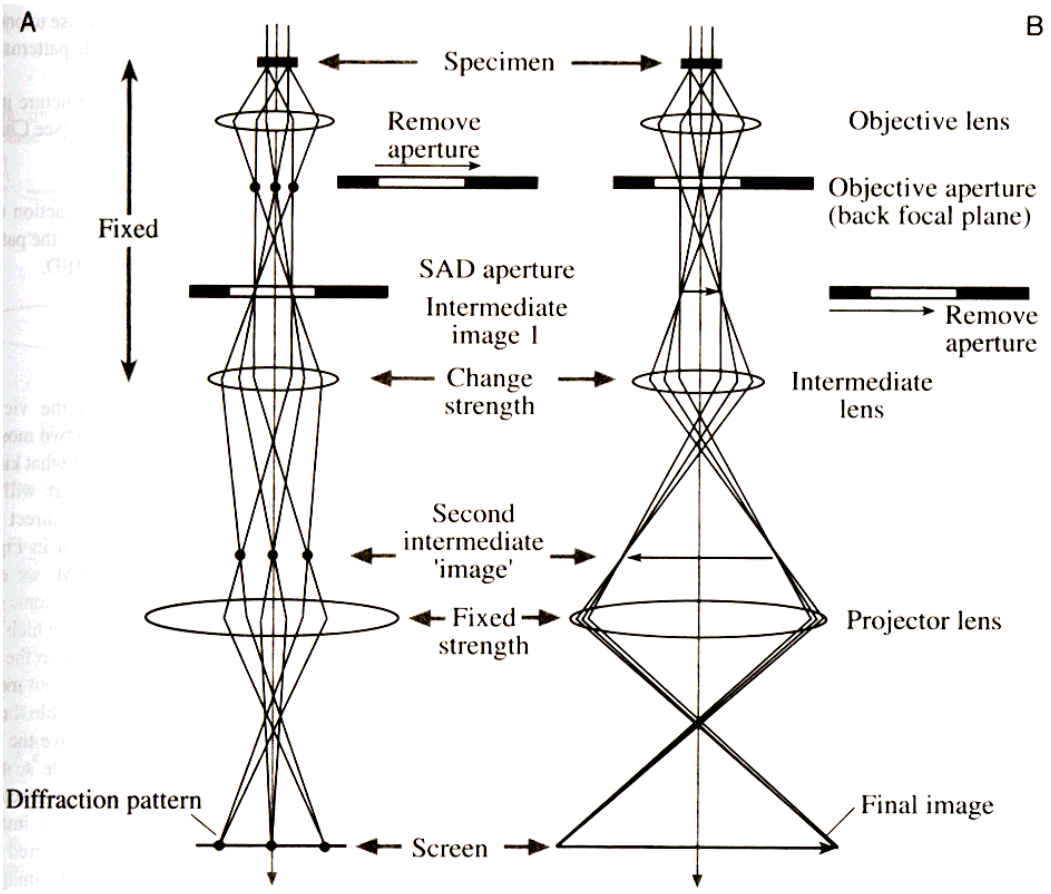

Figure 4.3 Ray diagrams depicting the role of OL and Imaging system in a TEM. Objective aperture and selected area diffraction (SAD) aperture are used to allow the desired electron go through to the imaging system to obtain the desired image or diffraction pattern, respectively. (Figure 9.12 of (4.1)).

by the OL , a projector lens (PLA), often referred to as final lens that projects the magnified image onto the other part of the imaging system, a viewing screen or a

CCD camera. The ray diagram showing the role of the last two components is shown in the Figure 4.3.

4.1.3 TEM Bright field & Dark Field Imaging

In its very basic operation, a TEM can be used to obtain two forms of images. After its interaction with the sample, the beam is composed of transmitted un-scattered and some scattered electrons.

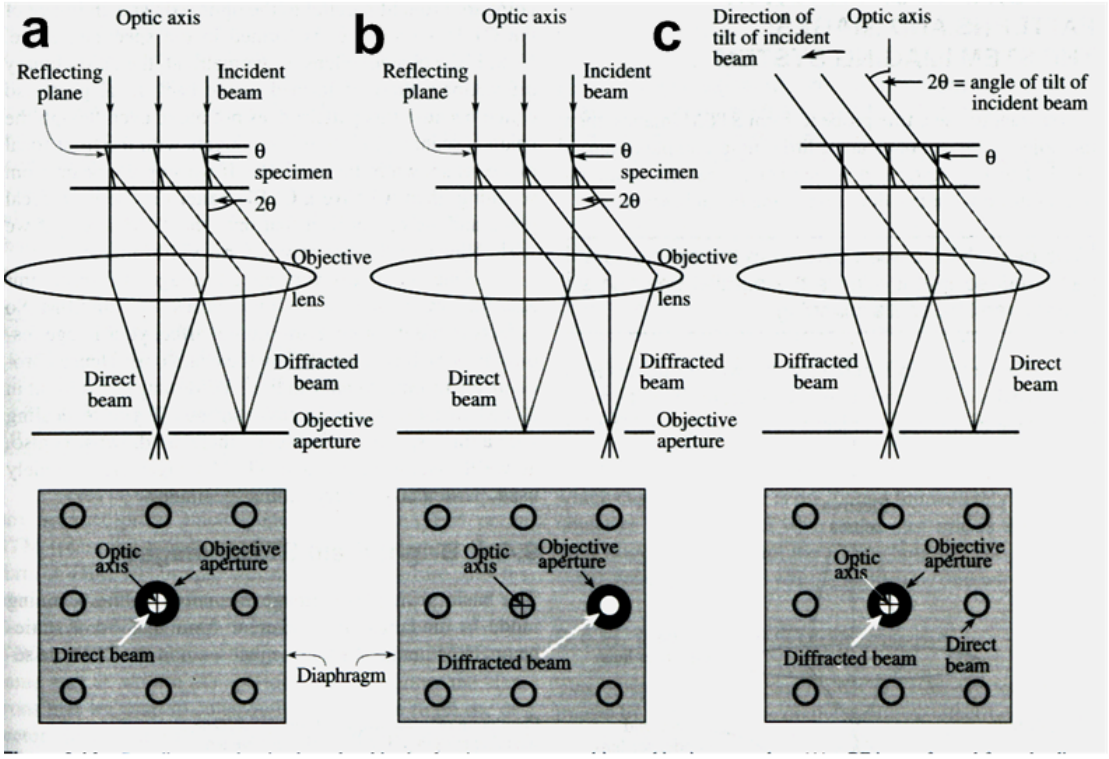

Figure 4.4 Diagram explaining BF and DF imaging. (a) BF imaging (b) Displaced area DF imaging and (c) Centered DF imaging. (Figure 9.14 of (4.1))

An image can be formed onto the viewing screen (or CCD) by using the direct un-scattered electrons or from some or all of the scattered electrons. This is done by adjusting the position of the objective aperture, located in the back focal plane of OL. This way only those electrons are let through which fall on the hole of the aperture. If the image is obtained by using the direct (un-scattered) beam we get a Bright Field (BF) image. Whereas, if the image is generated by using scattered electrons, the resulting image is called a Dark Field (DF) image. This is explained in Figure 4.4. BF imaging mode is a relatively straightforward operational mode and for imaging purposes TEMs are conventionally operated in BF mode.

While we image our samples in BF mode for structural information, DF mode is employed for thermal data collection for the reasons explained later in this chapter. Thus it will be instructive to go over Centered DF (CDF) operational mode described below.

4.1.4 Centered DF Operation

Since in DF mode objective aperture is moved to select the electrons that are off the optical axis, an image thus obtained is difficult to focus. It is because the off-axis electrons have a lot of aberration and astigmatism. This problem can be solved by tilting the beam so that it hits the sample at an angle which is equal and opposite to the scattering angle. This makes the scattering electrons to travel parallel to the optical axis of the beam. This process of obtaining a DF image by tilting the beam is known to microscopists as Centered DF (CDF) imaging and it is employed when a focused DF image is required. In general, however, it is much easier and convenient

to acquire DF in Displaced-Aperture (DA) DF mode, i.e. when the aperture is physically moved (as explained above), rather than tilting the incident beam. Moving the objective aperture does not misalign the microscope whereas tilting the beam does. In our experiments, we make a judgment call by looking at the DF image whether to resort to CDF or employ DADF. The basic principles of BF imaging, DADF and CDF are shown in Figure 4.4.

4.2 In-situ Transmission Electron Miscroscopy

A TEM is a much more powerful tool than just being an imaging system. In fact, it can be used as a mini laboratory. Heating and cooling the samples in-situ and observing their properties is very common. For heating, heating holders, equipped with typically a resistive heater wire and a calibrated thermocouple to measure the temperature, are commercially available. So are the cooling holders which employ liquid-N_2 or liquid-He and are frequently used for in-situ studies of both high and low T_c superconductors.

However, to be able to do in-situ thermal and electrical measurements we had to design and assemble our own specimen holder. Since, at the start of this project we had access to only Jeol 4000FX TEM, initial studies were performed on custom built-TEM holder (shown in Figure 4.5) for that microscope. Later we gained access to Jeol 2100 (LaB_6) and Jeol 2100F (FEG) microscopes for which we custom built another specimen holder . The specimen holders for Jeol 4000 series and Jeol 2100 series are not mutually compatible. However, the basic design and assembly process

for the two were same. Thus, we will briefly discuss the basics about the design of these holders below and leave the details for the appendix.

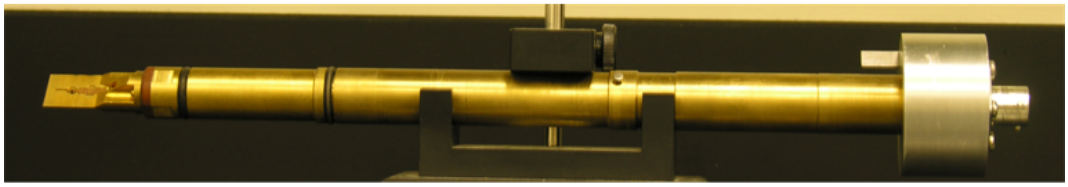

Jeol 2100

Jeol 4000Fx

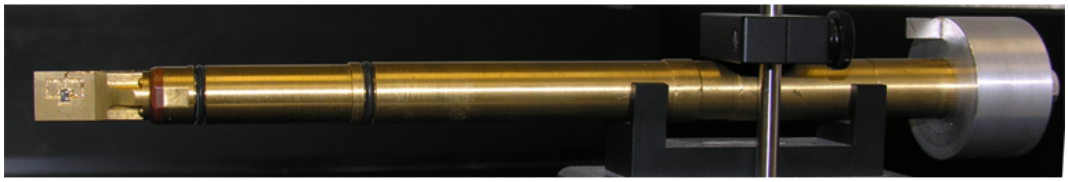

Hall Sensor for Jeol 2100

Figure 4.5 Custom-built TEM specimen-holders used for in-situ electron microscopy built by the author. Top two specimen-holders are used for electrical and thermal measurement. The bottom holder was custom-fabricated to calibrate the magnetic field produced by the OL.

The custom-built holder has four Beryllium-Copper (Be-Cu) clips that make electrical contact with the sample on one end and with the detronics connector at the other end through Cu wires. All of these four clips are electrically insulated from each other and the body of the holder. Hence this holder can be used for up to four probe

measurements. We utilized only two probes for most of the work reported in this dissertation.

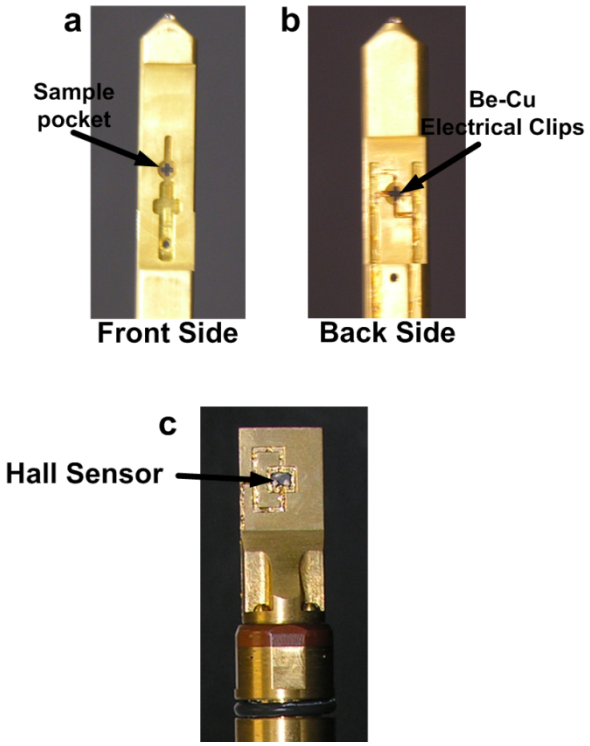

Figure 4.6 View of tips of the custom-built specimen-holders. (a) & (b) Front and back view of the tip of specimen-holder built for Jeol 4000FX microscope. This holder is capable of four probe measurements. The Be-Cu clips extend to the front of the holder through the hole and make electrical contact with the sample placed upside-down. (c) shows the holder used to calibrate field produced by the OL of Jeol 2100 microscope. It can be seen that instead of having a specimen pocket, such a holder has a hall sensor affixed at the center of the tip.

The body of the holder is made up of brass as opposed to phosphor bronze of which commercially available holders are typically made. The external end is the most bulky part of the holder. To make the holder lighter and avoid any weight imbalance at two ends, the external end was made of aluminium.

The Cumings group also studies magnetic properties of nanostrucutres by using a TEM. In one particular project magnetization directions of domain walls in artificial spin ice structures are studied in-situ. During such measurements TEM is operated in low magnification mode and thus during data acquisition, no current flows through OL. However for magnetization reversal of the domains an 'external field' is needed in such experiments, which is provided by passing current through the OL solenoid. To know the strength of the field produced by the solenoid, OL is needed to be calibrated to develop the relation between the current passed through OL solenoids and the field that current produces. For this purpose we custom-built a holder which had a Hall sensor affixed to it at the position where sample is placed in conventional specimen holders as shown in Figure 4.6 c. By employing this holder we calibrated the current through the OL and determined the relation between the current and the filed it produces. The relation is shown in the Figure 4.7.

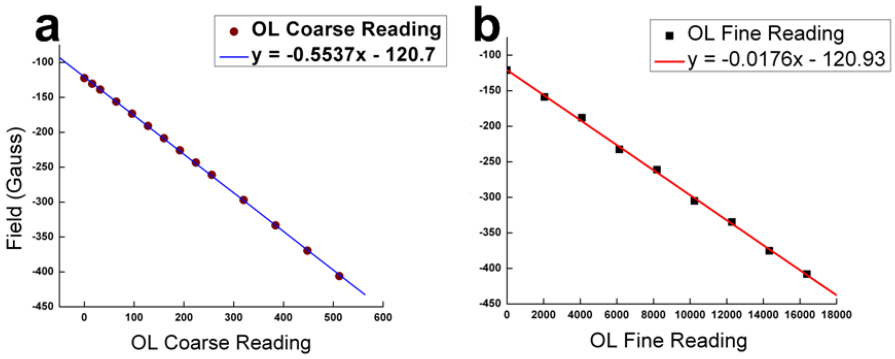

Figure 4.7 OL current calibration plots obtained by employing custom built TEM holder having a hall sensor.

4.3 Electron Thermal Miscroscopy

Scanning thermal imaging techniques conventionally employed to study nanostructures have their limitations. They rely either on measure of heat transfer through raster scanning of the sample by an AFM tip (in case of Scanning Thermal microscopy (SThM) (4.2)) or on measure of optical phonon energy absorbed by shinning a laser (in case of micro-Raman Spectroscopy) and hence provide an indirect measure of the temperature. Instead of obtaining a direct measure, the temperature in such techniques can only be inferred through theoretical models. Due to strong dependence on experimental details, the temperature thus extracted can only be approximate at best. Therefore to get an accurate measure of temperature, a separate (and independent) characterization is needed by incorporating the strong effects of experimental details on the measurements. Consequently we deemed it necessary to have a reliable thermal imaging technique at hand before proceeding on to the thermal characterization of MWCNTs.

We developed an in-situ real-time technique; we call Electron Thermal Microscopy (EThM), which provides a direct measure of temperature. This technique relies on in-situ observation of solid to liquid phase transition of nanometer-sized metallic islands deposited on an electron transparent substrate. As these islands undergo phase transition when the temperature is raised above their melting point, the diffraction of the electron beam by the islands changes. Under right imaging conditions this change in diffraction manifests itself as change in contrast of the islands in the two phases, thus enabling each island to be used as a binary thermal probe.

The high energy electrons incident on the bare substrate are only slightly scattered and are essentially transmitted, whereas those incident on the metallic probes get diffracted. If the TEM image is generated by the transmitted electrons (i.e. if TEM is operated in conventional BF mode) these islands will appear as dark patches on a bright background. Consequently, a phase transition will not be observable in a TEM. However, since the electron beam diffracts from these metallic probes differently when they are in solid or liquid phase, it is possible to observe the change in contrast of the two states by operating the TEM in correct DF conditions.

In this study we employ Indium (In) as thermal probes. In is a relatively low melting point (156.6 ^{o}C) metal with well characterized phase transitions. The basic principle of EThM is demonstrated in Figure 4.8. The composite diffraction pattern (obtained in solid and liquid phases) of In islands is shown in Figure 4.8 (b). Clearly, the diffraction pattern of the islands in the two phases is different. In the solid phase (left half of Figure 4.8 (b)) the diffraction pattern is composed of sharp rings because of the electrons diffracting at large angles where as in liquid phase the diffraction pattern is diffusive and amorphous-like. If the image is obtained by selecting the transmitted electrons, which is done by aligning the objective aperture concentric with the optical axis of the electron beam (BF mode), the TEM images of the In islands in the two phases would look identical (see Figure 4.8 a). However, if the diffracted portion of the beam is used to obtain the image by moving the objective aperture to the position shown by a white circle in Figure 4.8 b (DADF mode) or equivalently tilting the incident electron beam (CDF mode), the contrast of the In islands will be different in the two phases as shown in parts (c) and (d) of Figure 4.8.

Observing this change in contrast in solid and liquid phases is the basic principle of our technique. This is how we obtain maps of local temperature gradient over the entire in-situ field of view.

It is worth noting that even when molten, the In islands retain their shape. This is due to the presence of a thin but robust, self-passivating In_2O_3 layer around each individual island. This enables our thermal imaging technique to be repeatable over several phase transition cycles.

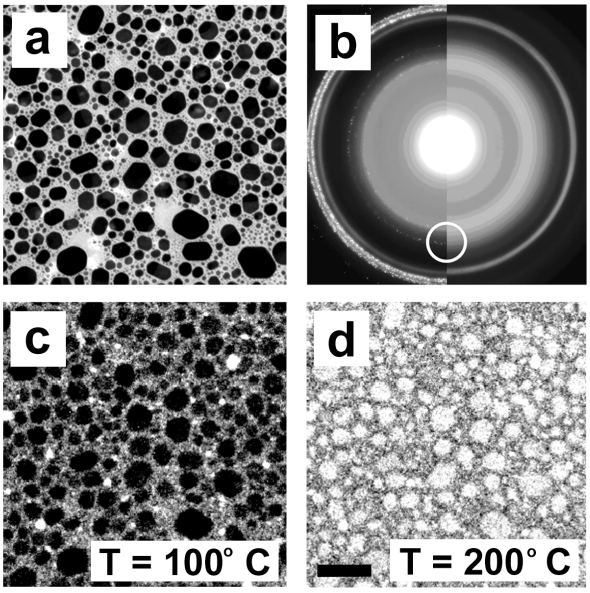

Figure 4.8 TEM images of the In Islands. (a) Bright-field image of the islands. (b) Composite diffraction pattern of In islands. Dark field images are obtained when the aperture is placed approximately where the circle is drawn. (c) Dark field image of the islands when they are in solid state. (d) Dark field image of the islands in liquid state. (Figure 1 of (4.3))

Samples are prepared on commercially available free standing electron transparent silicon nitride (SiN_x) membranes because they are electrically non-conducting and can sustain high temperatures. As a check of the validity of the

concept we proceeded by measuring the thermal conductivity of these silicon nitride films and compared it with the values found in literature for similar free standing SiN_x membranes. These results have been published in 2008 in Nano Letters (4.3). Once this technique was developed, we employed it to study the thermal properties of MWCNTs as explained in chapters 5 and 6.

Device Fabrication and Experiment

The local temperature gradient is attained by Joule heating in metallic heater wires. 1-d Palladium-Titanium (Pd/Ti) heater wire about a micron in length was fabricated by electron beam lithography (EBL) on 100 nm thick membranes. In later studies thinner membranes of thickness 50nm and 20nm were also used. In all of our experiments the thermal conductivity of the substrate is individually calibrated.

Preparation of samples for our experiments is a multi-step process, the details of which are described below:

STEP I Spinning Resist

The first step involves spinning and baking of the resist on the SiN_x substrates. We start by spinning a copolymer resist, composed of a mixture of polymethyl methacrylate (PMMA) and 8.5% methacrylic acid, on a bare substrate. During the deposition of this layer the sample is spun at 4500 rpm for 40 sec. This copolymer resist is shortly called as MMA(8.5)MAA or simply MMA . Once MMA is deposited, the sample is heated at about 150 ^{o}C for 10 mins to harden the deposited resist. This layer of MMA acts as an under layer to produce a re-entrant profile.

On the top of hardened MMA, a layer of PMMA having molecular weight of 950k is deposited. This layer is spin cast at 6000 rpm for 40 sec and then baked for 10 mins at about 150 ^{o}C. Finally, we deposit a thin conducting layer of Aqua-Save (4.4) onto this bi-layer resist. This conducting layer is added to help in writing the contamination spot during electron beam lithography (EBL). Using a contamination spot to focus and correct for any astigmatism in the beam is critical for obtaining the desired resolution of the features. The schematic of the sample preparation details is shown in the Figure 4.9.

STEP II Electron Beam Lithography

Once the resist is deposited onto the substrate, the desired pattern is written by using EBL. The electron beam dissociates the C-C bonds in the polymer through scission. Consequently the larger parent polymer breaks down into smaller segments. Once pattern is written, the water soluble Aqua-Save layer is removed by de-ionized (DI) water, before developing the e-beam exposed sample in a 1:3 solution of Methyl Isobutyl Ketone (MIBK) and Isopropanol (IPA). The developing time is usually between 30-60 secs. The smaller segments generated as a result of scission of larger molecules are more readily soluble in MIBK/IPA solution. PMMA and MMA both are positive resists. (STEP II of Schematic of Figure 4.9)

STEP III Metal Depostion

The next step is to deposit high purity (usually better than 99.99%) metal through thermal or electron beam evaporation methods. We use thermal evaporation

for chromium (Cr) and gold (Au) deposition whereas for Pd electron beam evaporation is employed. (STEP III of Schematic of Figure 4.9)

STEP IV LIFT OFF

After metal deposition, the sample is soaked in acetone for 30-60 mins. Acetone dissolves the resist left in the undeveloped regions and excess metal is removed with it. The only metal that does not get washed away after the lift-off is where the pattern was written by EBL. (STEP IV of Schematic of Figure 4.9)

STEP V Indium Deposition

The final step is the deposition of thin layer of In at the back side of the substrate. When thermally evaporated to a thickness of 16-20 nm (measured by quartz crystal monitor) In forms a discontinuous layer of sub-200nm islands. These In islands act as thermal probes in our measurements. (STEP V of Schematic of the Figure 4.9)

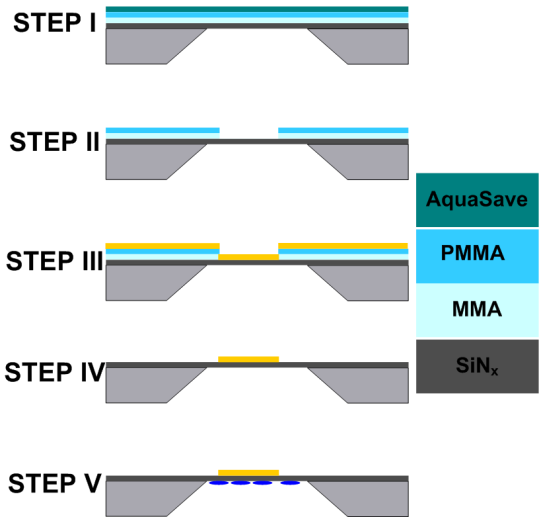

Figure 4.9 Schematics of sample preparation steps. STEP I involves spinning and baking of e-beam resist. The legend on the right gives the order in which the resist is put down on SiN_x substrate. In STEP II, after EBL, sample in developed for 30-60s. In STEP III metal is evaporated. STEP IV is the schematic of how the cross-section of the sample looks like after the lift-off. Finally in STEP V, a thin discontinuous layer of In is evaporated on the back side.

Data and Results

As mentioned before, in-situ thermal imaging of the device is made possible by using a four probe custom-built electrical measurement TEM specimen holder. Optical image of the sample in such a specimen holder is shown in Figure 4.10.

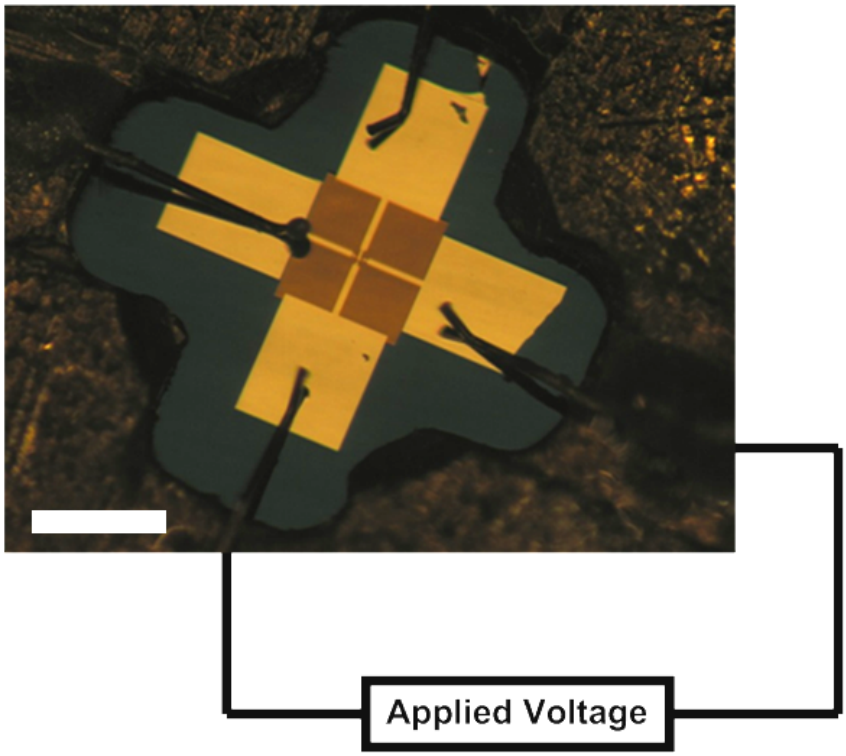

Fig 4.10 Optical Image of the sample in custom-built TEM specimen holder. Be-Cu copper clips of this specimen holder electrically contact the heater wire in middle of the sample (not apparent in this optical image) to the external electronics through large Pd/Ti contact pads. The scale-bar is 1 mm.

Joule heating in the Pd/Ti metallic wire when a bias is applied across them creates local temperature gradients. When the temperature of substrate at any particular location reaches the melting point of In (156.6 ^{o}C), the islands at that location melt. By ramping the applied voltage, a series of DF images are obtained. The location of each island and the voltage at which it melts are captured in real-time by a video recorder. High resolution images during the voltage cycle can also be obtained by using the Gatan CCD camera on the Jeol 2100 TEM as shown in 4.11 (a). By assigning unique colors to the lowest voltage at which each In island melts, a

thermal map as shown in Fig 4.11 (b) is obtained where like colors represent isothermal regions.

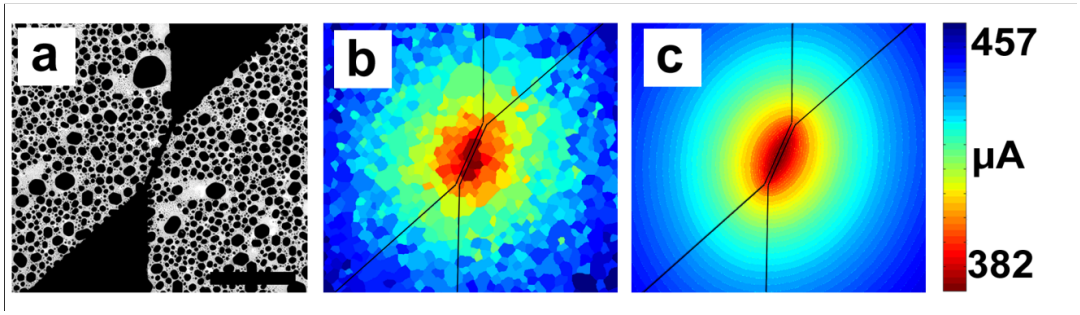

Fig 4.11 (a) A bright-field, high resolution image of the device with tapered electrodes and In islands on the back. Scale bar is 1 μm (b) Thermal map obtained experimentally. Different colors correspond to different voltages needed to melt each island. Each color corresponds to an isothermal region. (c) Map obtained by finite element analysis used to extract the thermal conductivity of the membrane. (Figure 2 of (4.2))

As expected for Ohmic Joule heating in metallic wires, most of the heat dissipation occurs at the middle of the heater wire. To model our data we employed finite element analysis where temperature T is given by,

$$\nabla(\kappa\nabla T) + P = 0$$

κ is the local thermal conductivity and P, is power given by,

$$P = \sigma|\nabla V|^2,$$

V is the electric potential and σ, is electrical conductivity which has a temperature dependence given by,

$$\sigma = \sigma_o(1 + \alpha\Delta T)^{-1}$$

The parameter α in the above equation is the thermal coefficient which gives the transfer of Joule power from low temperature to high temperature regions. The electrical conductivity and temperature coefficient are iteratively fitted by matching the model to the measured current density of the sample at low and high bias respectively.

The temperature dependence of thermal conductivity of the heater wires is calculated by Wiedemann-Franz law (4.5). The simulations for this study were carried out by using FlexPDE. By choosing the thermal conductivity of SiN_x (assumed to be constant in temperature) to be a free parameter a series of thermal maps were obtained and compared to the experimental data. The thermal conductivity of the membrane was extracted to be $3.6 \pm 0.1 W/m \cdot K$ from the simulated thermal map that most closely resembled the one obtained experimentally (see Figure 4.11 (c)). This extracted value is in agreement with the value found in literature (4.6-4.9), thus confirming the validity of our technique. In Figure 4.11 (c) a small field of view in shown but simulations using the above equations was performed over the entire $500 \times 500\ \mu m^2$ membrane window.

4.4 Resolution limits of EThM

(i) Melting Point Suppression due to Variation in Size of the In Islands

In was chosen as indicator because it is a low melting point metal whose phase transitions can be standardized (4.10). The deposited In forms a discontinuous layer due to Volmer-Webber (4.11) growth. The size of these islands can vary

between a few nm to 200 nm. However, we observe that the islands that are smaller than ~30nm are completely oxidized.

Due to the variation in size, there is suppression in melting-point of these islands which introduces a temperature uncertainty in our technique. The variation in melting point of In with the size of the islands can be measured independently by employing a heating-holder. We observed that the temperature uncertainty due to variation in size of the islands is variable, but never more than10 ^{o}C. We take this uncertainty into account in analysis of the data.

Additionally, we observed that solidification of the islands occurs at significantly lower temperatures than the temperature at which they melt. The islands have to be super-cooled before they solidify. In comparison to the melting, the solidification process is noted to be random and less reliable. Consequently, we always rely on melting profiles for thermal imaging.

(ii) Spatial Resolution

The size of the Indium islands, average spacing between them and the thickness of the substrate limit the resolution of this technique to about 200 nm. Smaller and more uniform diameter islands can be obtained if the substrate is kept at higher temperature (around the melting point of In) during the metal deposition or by evaporating a layer thinner than having a typical thickness of 16 nm-19 nm used in our experiments. But if the Indium layer is made too thin (<15 nm, as measured by quartz crystal monitor), it gets oxidized and makes thermal imaging impossible. However, in principle, the resolution limit can be pushed to ~10 nm or lower if

chemical methods are employed which are reported to produce smaller and uniform metal islands (4.12).

Alternatively, other metals and alloys can potentially be used for thermometry. Such metals include Sn, Pb, Ga, Al and their alloys. To reduce the signal to noise ratio and thus increase the spatial resolution, we have also used thinner substrates, which are readily available, in our later studies. For example, the experiment described above was repeated on 50 nm thick membranes.

(iii) Effect of Beam Heating

During TEM imaging, the electron beam can induce a measureable amount of heating. We noted that under certain beam conditions melting of In occured at a temperatures lower than expected. This was due to the additional heating provided by the intense electron beam. However, if we chose spot size 4 (corresponding to beam current of 42 pA) instead of generally employed spot size 1(corresponding to a beam current of 508 pA), it is still possible to accumulate data in DF mode but the effects of beam heating become negligible (less than 1^{o}C, as measured by the specimen heating holder).

While we can image our sample using this technique, over several voltage cycles, the In does eventually oxidize with repeated exposure. The exact mechanism of the oxidation process or its dependence on the energy of the electron beam is not clear but it only occurs if the sample is simultaneously heated to melting and illuminated with the electron beam, and we find the imaging life we find the imaging

life of samples is significantly increased by using less intense beam (larger spot size). This enables us to capture higher exposure images, with low signal to noise ratio.

To quantify the effects of beam heating we image a sample that has In evaporated at the back, in TEM by using a heating holder. A heating holder heats the sample circumferentially around the edge of the sample which results in a temperature gradient between the center of the suspended region (which is not thermally anchored to Si frame) and the edges of the Si frame due to radiative heat loss within the $500\mu m \times 500\mu m$ membrane region. Since the edge of the suspended region is thermally anchored to the Si frame underneath, we do not expect the electron beam heating to have much effect at the edge of the suspended window.

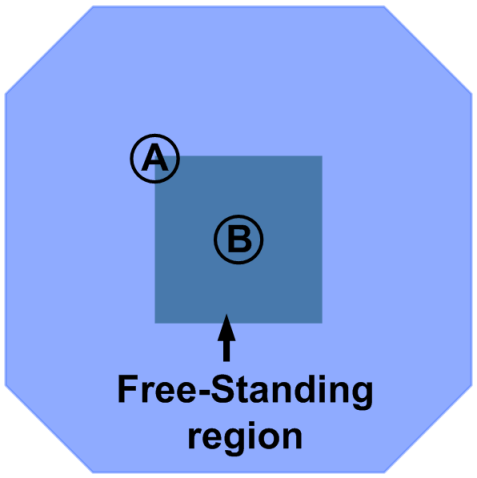

Figure 4.12 Schematic showing the regions of observation at the edge (A) and the middle (B) of the $500\mu m \times 500\mu m$ suspended region, to quantify the effects of beam heating.

To verify this we proceed by measuring the temperature at which islands on the edge (region (A) in Figure 4.12) melt under varying the beam conditions. We observe that, irrespective of the beam conditions, melting at the edge always occurred at 156.6 C

Heating Holder Temperature Needed to Melt Indium when Imaging in the Center of the Free-Standing Membrane

Spot Size	No Condensor Aperture Inserted	First Condensor Aperture Inserted
1	136.80 ^{o}C	167.0 ^{o}C
2	150.71 ^{o}C	170.45 ^{o}C
4	174.62 ^{o}C	175.69 ^{o}C

Table 4.1 Table showing how different beam conditions can have an effect on melting of In.

However the temperatures at which melting at the center of the suspended SiN_x region occurs (region (B) in Figure 4.12), vary with the beam conditions. At the lowest and second lowest beam currents (at which the DF imaging is still possible) the In at the center (region (B) in Figure 4.12) undergoes phase transition at 175.69^{o}C and 174.62 ^{o}C. This implies that under such conditions heating due to electron beam results in a temperature variation of 1^{o}C which is less than the temperature uncertainty in melting temperature of In due to variation in their sizes. At the highest beam current same islands melt at a much lower temperature of 136.8 ^{o}C. This suggests that heating due to electron beam can be substantial, on the order of ~40 ^{o}C. Therefore, we take data under the beam conditions that do not heat the sample significantly. Effect of heating due to electron beam at different beam conditions is

summarized in Table 4.1. Using these guidelines, we have selected to use spot size 4 and the first condensor aperture for the work described in this dissertation.

References

4.1 D. B. Williams and C. B. Carter, Transmission Electron Microscopy, Plenum Press, New York (1996) (ISBN:0-306-45247-2)

4.2 Majumdar, A. Scanning thermal microscopy. Ann. Rev. Mater. Sci. 29, 505 (1999)

4.3 T. Brintlinger, Y. Qi, K. H. Baloch, D. Goldhaber-Gordon, and J. Cumings, Nano Lett., 8(2), 582 (2008)

4.4 Aqua Save is sulfonated polyoniline obtained from Rayon Mitsubishi

4.5 Wiedemann-Franz Law, Kittel, Introduction to Solid State Physics, 5th Ed, Wiley, New York (1976)

4.6 C.H. Mastrangelo, Y. C. Tai and R. S. Mullar, Sensor Actuat a-Phys 23, 856 (1990)

4.7 S. M. Lee and D. G. Cahill, J Appl Phys 81 (6), 2590 (1997)

4.8 W. Holmes, J. M. Gildemeister, P. L. Richards et al., Appl Phys Lett 72, 18, (1998)

4.9 B. L. Zink and F. Hellman, Solid State Comm. 129, 3, 199 (2004)

4.10 H Preston-Thomas, The International Temperature Scale of 1990 (ITS-90) Metrologia, 27, 3, (1990)

4.11 A. Pimpinelli, J. Villain, Physics of Crystal Growth, Cambridge University Press. ISBN 0-521-55198-6 (1999)

4.12 G. Schmid. Chem. Rev. 92, 1709 (1992)

Chapter 5

Measurement and Manipulation of Thermal Contact Resistance of an Individual Multiwalled Carbon Nanotube

While carbon nanotubes show promise for new thermal management architectures due to their exceptionally high thermal conductivity, there are potential difficulties in fabricating such devices. Depending on the application, these extraordinary thermal conductors may be desired to be either anchored to thermally insulating mechanical supports or be required to make good thermal contacts, such as to heat sinks. Thus, on the road to making thermal management devices it will be a milestone to have the ability to manipulate the thermal nature of such mechanical contacts. However, the nature of contacts to nanotubes has been generally considered a limiting factor that cannot be controlled as per the demands of the application. Here we demonstrate that by manipulating their thermal contact resistance by almost two orders of magnitude, carbon nanotubes can be made to have weak or strong thermal coupling to their mechanical anchors. In-situ electron thermal microscopy, described in the previous chapter enabled us to directly measure the thermal contact resistance to be $4.2^{+5.6}_{-2.1}$ $\mathrm{m.K/W}$ when the thermal coupling between a nanotube and its anchor

point is strong while it is greater than $250\ \mathrm{m.K/W}$ when coupled weakly. This work is published in peer-reviewed journal Applied Physics Letter (**K. H. Baloch**, N. Voskanian, J. Cumings, APL 97, 061901 (2010))

5.1 Motivation

With a growing emphasis on energy conservation and miniaturization to increase the efficiency of electronics, an interest has emerged in extending thermal management technology down to the nanometer scale. CNTs are considered to be a strong candidate material for these applications due to their unique thermal properties (5.1-5.4). Even though many experiments have been reported and many questions relating to their electrical and mechanical properties have been resolved, these novel materials remain elusive in their thermal properties. Evidence indeed suggests them to be superior thermal conductors, but the reported thermal conductivity values vary widely between 200 W/m.K and 3000 W/m.K in the literature (5.2, 5.5-5.12). This incongruity in some cases can be attributed to variations in thermal contact resistance R_c (5.13) a parameter that, as discussed in Chapter 3, determines the amount of heat flow into or out of CNTs. Reproducibility and control of R_c would open the door for a new generation of nanoscale thermal management and thermal logic devices such as thermal diodes and thermal transistors (5.14, 5.15).

As discussed in Chapter 3, because of the importance of thermal contact resistance on thermal transport in individual CNT, the topic has recently generated interest in the scientific community, with studies to date on the subject reporting values that vary widely (5.13, 5.17-5.26). For example, Maune *et al.* perform

thermometry employing electrical breakdown of CNTs to report R_c values of 0.6-3 m.K/W (5.18), whereas Tsen *et al.* report a value for R_c of 25 m.K/W from photothermal current microscopy that relies on local heating from a scanning laser (5.20). The wide difference in R_c values may be attributable to the uncertainties in the characterization of the heat sources. In the former case, heat is assumed to be generated by Joule heating from electrical current in the CNT, while in the latter case photo-absorption is the source of thermal power. Unfortunately, in both cases the heat sources are not amenable to independent characterization and the underlying phenomena thus still leave substantial uncertainties in the modeling. In this work, we rely upon a well-characterized metallic palladium (Pd) heater wire as a power source to heat a CNT. Using this, we demonstrate by direct measurement that R_c can be manipulated by more than two orders of magnitude, making it possible to realize thermally conducting or thermally insulating contacts as may be needed for different applications.

5.2 Sample preparation

The samples used to measure the contact resistance of CNTs are prepared on SiN_x substrate which can be 20nm, 50nm or 100nm thick, in multiples steps as described below:

1. **Making the substrate ready**

We start by writing alignment markers and the contact pads on the substrate by using EBL and thermal evaporation of a layer of Cr/Au (3nm, 27nm).The purpose of

having such alignment markers is to use them as a reference in determining the position of CNTs on the substrate.

2. Making CNTs ready

(i) Isolation

For experiments described in this dissertation, high quality (as grown), arc-discharge MWCNTs are obtained from Sigma-Aldrich. The MWCNTs in the arc-discharge grown boule are scrapped off by using a razor blade from the graphitic outer shell and the graphite inner core. These scrapped off, MWCNTs are in the form bundles. Individual MWCNTs are obtained from these bundles by gently grinding them to a powder.

(ii) CNT Solutions

The nanotube powder is then dissolved in IPA. Their typical weight to volume proportion is 0.6 mg of CNT powder per 0.5mL of IPA. Sonication is required for uniform dispersion of CNTs in IPA. The Figure 5.1 shows the CNT/IPA solutions before and after the sonication process.

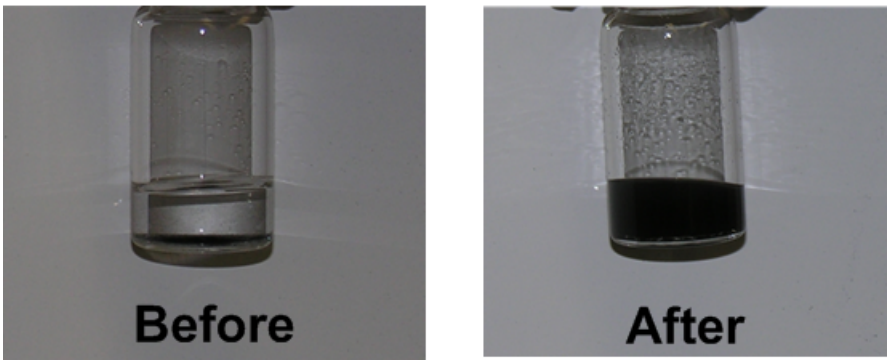

Figure 5.1 CNTs in IPA before and after the sonication process.

3. Casting CNTs onto the Substrate

This solution is then spin cast onto the substrate that already has alignment markers. This process will disperse CNTs on the substrate; many of them would be clean and isolated.

4. Determining the position of CNTs on the substrate

The position of the CNT of interest w.r.t . the alignment markers is determined by imaging the sample in TEM. One such CNT near the alignment marker is shown in Figure 5.2. To minimize the effects of beam damage, the imaging is done by operating the TEM at 100 kV instead of at conventional 200 kV.

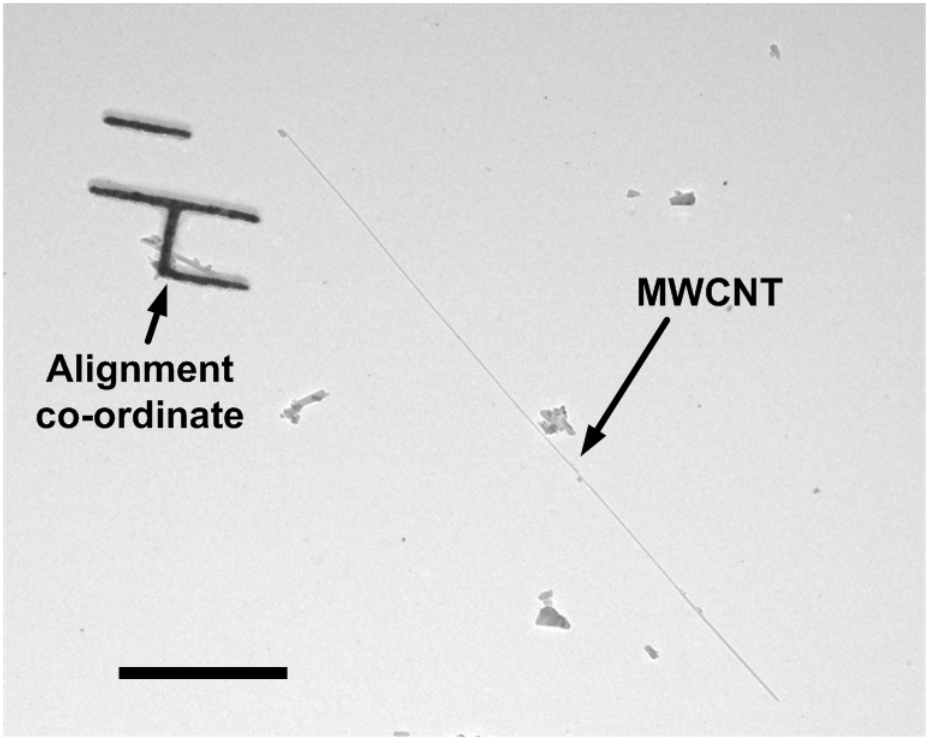

Figure 5.2 The position of a CNT on the substrate can determined to within a few hundred nanometers by making use of alignment markers. The scale bar is$1\mu m$.

5. Electrical/Thermal contacts

Once the position of CNTs on the substrate is known, the next step is to make electrical and thermal contacts to the CNT. The pattern is generated in Design CAD and the lithography steps are repeated as described previously. Because of its small grain size and the fact that it does not require a wetting layer, our electrical and thermal contacts are made up of Pd.

6. Deposition of Indium

As a final step a thin layer of In is deposited on the back side of the substrate. Since the contrast from this In layer makes it difficult to see the CNT, the images of a test device used for thermal measurements are shown in the Figure 5.3 before and after In deposition.

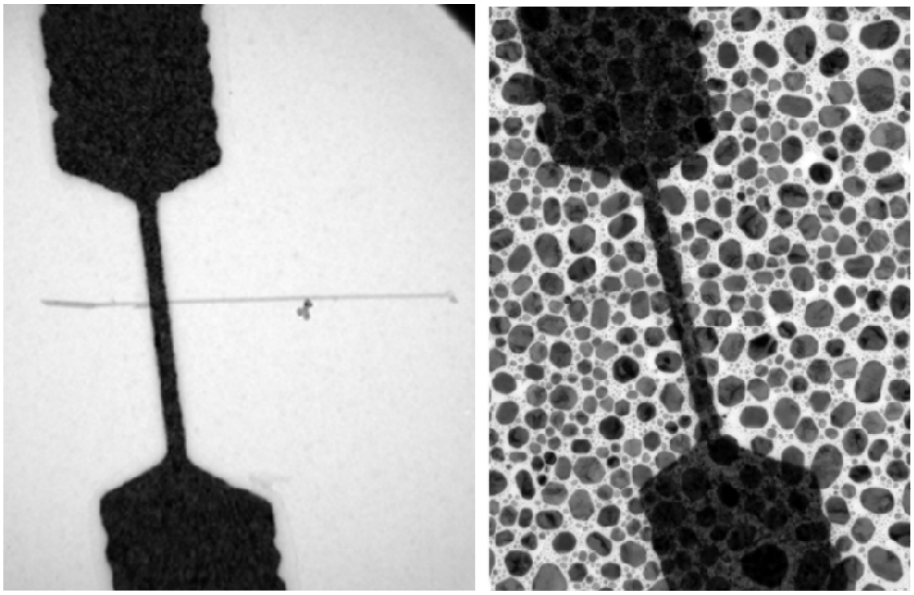

Figure 5.3 TEM image of a typical CNT device (before and after In deposition) after all the fabrication steps have been completed.

5.3 Thermal Contact Resistance Measurements

In these experiments EThM enabled us to make clear conclusions about the R_c value for the nanotube on the bare substrate ($^{SiN}R_c$) as well as for R_c for the nanotube underneath the Pd thermal contact ($^{Pd}R_c$).

Measurements were done on two types of samples, as shown by TEM images in Figures 5.4 a and 5. 4 b. In one type, a CNT was thermally anchored only by the SiN_x substrate beneath and was heated by a Pd metal contact connected to a resistive Pd heater wire. In another sample type, a second Pd contact was added to the free end of the CNT to control the contact resistance with the substrate. For clarity, a schematic top view of the test device where the CNT is thermally anchored by Pd metal at both ends is depicted in Figure 4 c. A schematic cross-section of the anchored region of CNT is shown in Figure 4 d, showing that the mechanism of thermal anchoring is the increased area of thermal contact of the CNT beneath the Pd. Note that the CNT only contacts the SiN_x substrate underneath tangentially, while the width of the overlap between the CNT and Pd metal above is nearly half the circumference of the CNT. This difference in contact area is the primary mechanism we propose for tuning the thermal contact resistance.

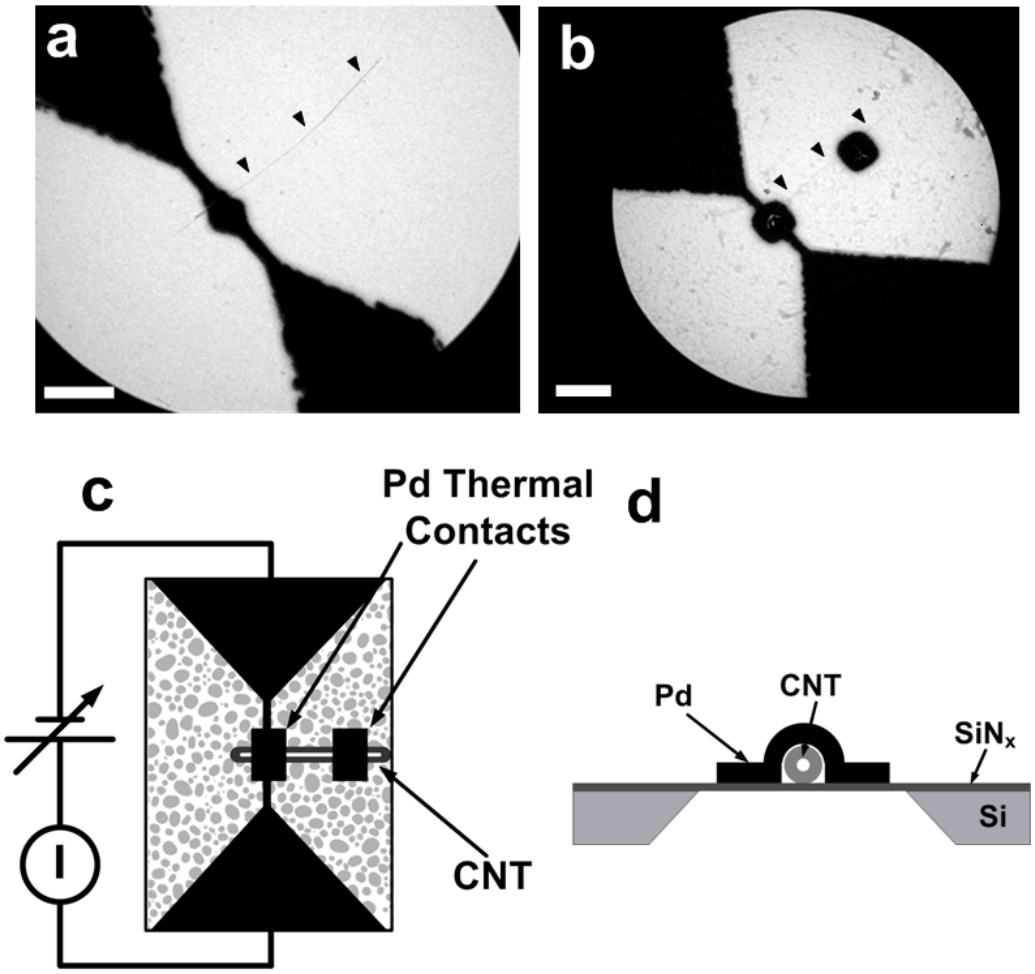

Figure 5.4 (a) and (b) TEM images of the thermally anchored and unanchored CNT devices used for this study, prior to depositing In. Small arrows indicate the position of CNT, and both scale bars are 1 μm. (c) Schematic diagram of thermally anchored device with a circuit overlay. The device is fabricated on a silicon nitride membrane with a 20nm thick discontinuous In film deposited on the back side, represented by gray dots. The thermal contact resistance to the nanotube is decreased by two square palladium contacts at each end of the nanotube. Joule heating in the Pd heater wire can be used to heat the CNT and its environment. (d) Schematic cross-section of the sample, where it can be seen that the CNT touches the SiN_x membrane only tangentially whereas the contact of the CNT with the Pd contact width is approximately half the circumference.

The heat source in these experiments was Joule heating in the Pd wire produced by a test current, a phenomenon which is well-characterized, as describe in the previous chapter. In the absence of a nanotube, the distance from the center of the Pd heater wire to which islands melt on either side is expected to be same at a given voltage, reflecting the geometrical symmetry of the structure as shown in Figure 5.5 a. However, the presence of a nanotube should introduce an asymmetry in this distance due to its high thermal conductivity (approximately 1000-3000 W/m.K, refs. 5.6-5.10) relative to the substrate (~2.5 W/m.K for 50 nm thick membranes) as shown in Figure 5.5 b. While the contact resistance between the nanotube and the substrate, R_c is assumed to be zero in Figure 5.5 b, the amount of the asymmetry can give a reliable measure this quantity.

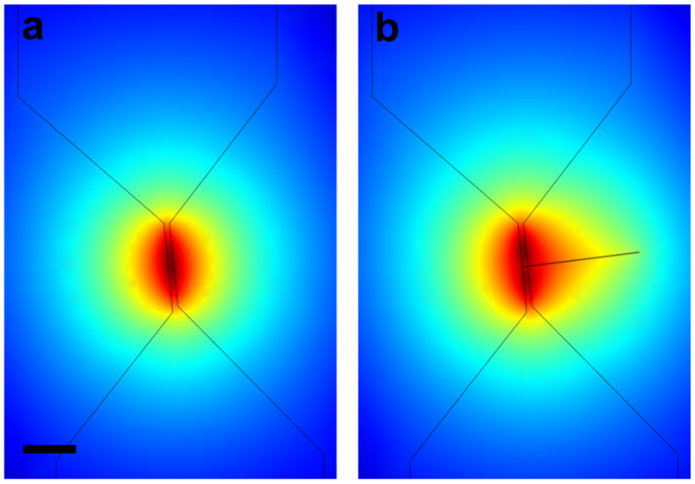

Figure 5.5 Simulations perdicting melting profiles of In islands with and without a CNT. (a) Given the symmetry of the geometry, the melting profile should be symmetric about the heater wire. However, assuming thermal conductance between the CNT and its surrondings, simulations predict an asyemmtric melting as shown in (b) because the thermal conductivity of the CNT is much higher than that of SiN_x.

In the case of the device shown in Figure 5.4 a, the thermal conductivity of the region to the right of the heater should be higher than of that on the left. This means that the melting of the In at a particular region on the right of the heater should occur at lower applied voltages compared to the melting of In at a symmetric region on the left side.

Data are acquired by continuously ramping the applied voltage using a MATLAB command and capturing the DF TEM images at each voltage. Selected frames at the specified heater biases are shown in Figure 5.6. These "as-captured" DF frames do not show any asymmetry in melting.

It will be more instructive to generate a single thermal map from these individual frames. This is done by assigning a unique color to the voltage required to melt each island. Figure 5.7 shows such a thermal map with an overlay of device geometry. The like colors represent isothermal regions. To detect an asymmetry, two parallel white lines equidistant from the heater wire are also added as a guide to the eye. Thus we can qualitatively see that melting profile of In islands in this device is identical to the situation in which there was no CNT (Figure 5.5 a). This indicates that even though the CNT has a high thermal conductivity, its ability to transport heat to the substrate is limited by a high thermal contact resistance ${}^{SiN}R_c$. Other experiments on similar devices also showed this lack of asymmetry, demonstrating that a CNT adhered to a SiN_x substrate has an inherently high ${}^{SiN}R_c$.

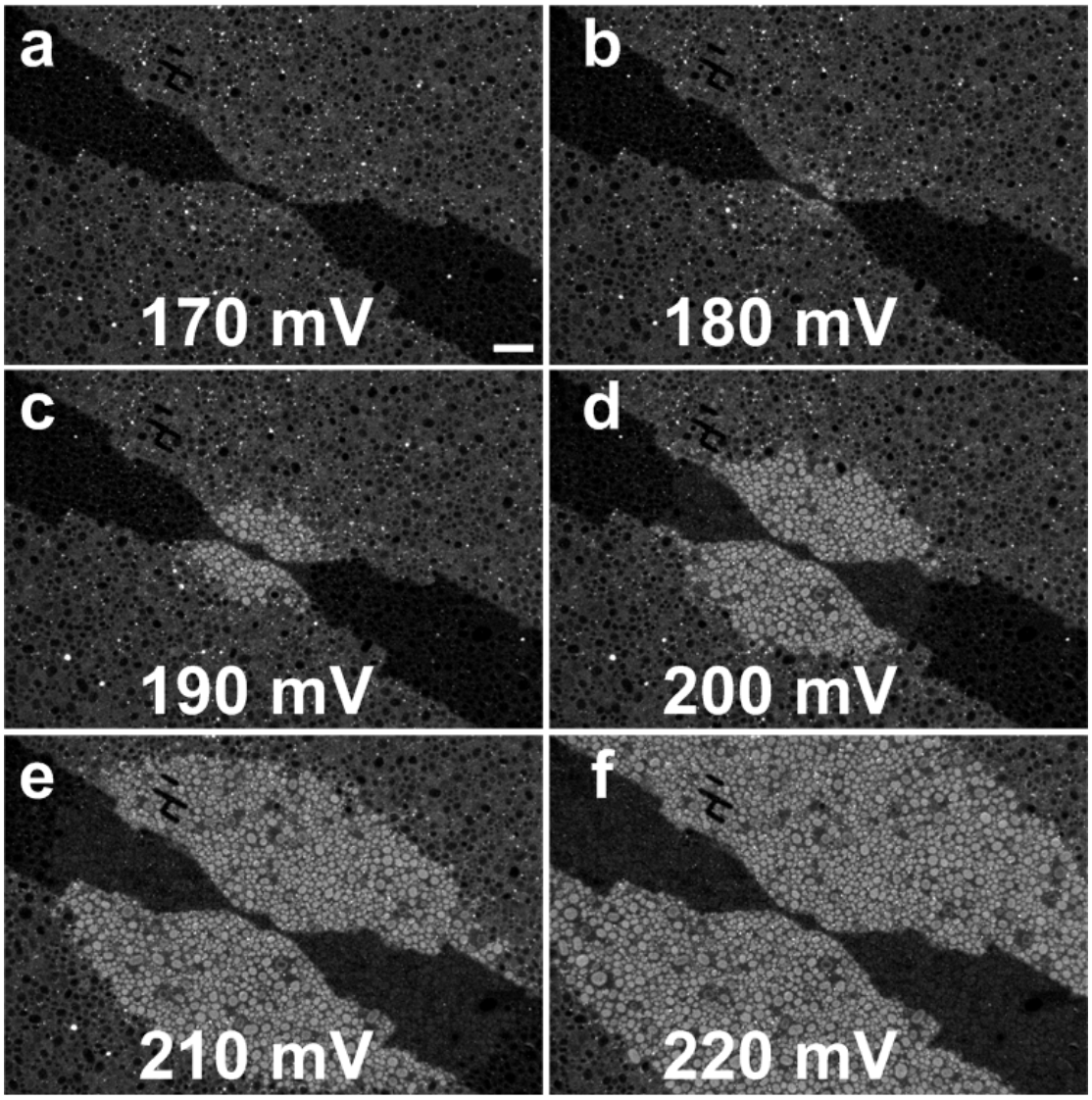

Figure 5.6 Experimental data on the device shown in Figure 5.5 (a) taken at the specified applied voltages. It can be seen that when TEM is operated in D. F. mode the contrast of the islands in solid-liquid phase is different. Scale bar is $1\mu m$.

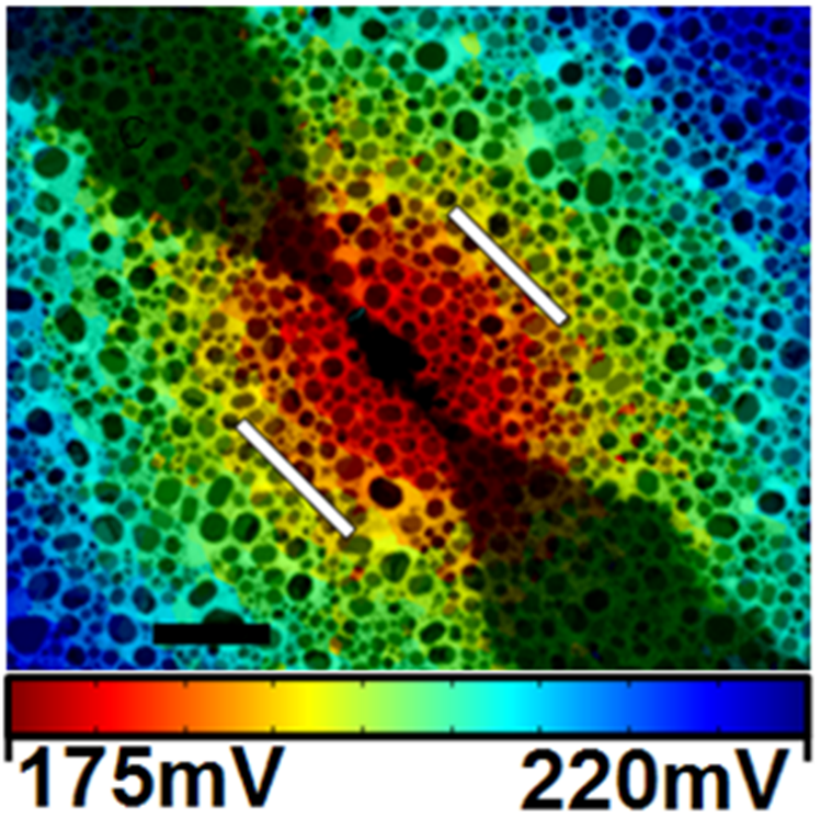

Figure 5.7 The individual TEM frames obtained by D. F. imaging can be complied into one single image by assigning a unique color to the voltage needed to melt each island. This figure shows such a thermal map with an overlay of image of the device. Here like colors represent isothermal regions. White lines are added equidistant from the center of the heater as guides to the eye for detecting any asymmetry. Contrary to prediction of Figure 5.5 b the data show no clear asymmetry in melting of the In islands on the two sides of the heater wire. This demonstrates that thermal contact between the CNT and substrate is not perfect and thus an unanchored CNT cannot transfer heat effectively to the substrate.

To measure ${}^{SiN}R_c$ quantitatively, we extract the voltages that produce melting at a point 2/3 along the nanotube[1] and at a symmetric point on the opposite side of the heater wire. These locations were chosen as they show the largest temperature-asymmetry in the finite-element model and are thus the most sensitive to variations in ${}^{SiN}R_c$. In quantitative analysis, we note that the In islands used to measure temperature come in a distribution of sizes, and confinement effects (5.27) therefore produce an uncertainty in the melting temperature of any given island. If we use just a single In island on each side to detect a voltage asymmetry, this results in a large uncertainty in the amount of asymmetry in the temperature profiles, adding error to our measurement of ${}^{SiN}R_c$. To improve our estimate of ${}^{SiN}R_c$, we instead use an ensemble of islands to extract a more precise measure of the asymmetry. This is done by selecting sets of at least 30 In islands each in proximity to the nanotube and calculating an average melting voltage and confidence interval for each set. To accomplish this, a control region is defined within a given radius around the point of interest and an identical symmetric region is defined on the opposite side of the heater wire. The radius of these regions is chosen so that they both contain at least 30 islands. For all islands within these two regions, the melting voltage and the distance from the center of the wire are extracted and plotted as shown in Figure 5.8.

[1]Since a CNT can also be viewed as a "fin" heat spreader, the characteristic thermal length of the fin (at which T drops by 1/e) may be a better length scale to use instead of using a distance 2/3 length of CNT. This characteristic length increases with R_c and K. Using the lowest values consistent with our experiments, we estimate a characteristic length much longer than the CNTs used in these studies. Thus the parameter has a diminished utility in modeling our results

Then these values are fit using a linear regression algorithm to obtain the expectation value and 95% confidence interval for the voltage needed to bring the substrate to the melting point of indium at the control point and also at the symmetric point. These expectation and 95% confidence interval values are used in the finite-element modeling described below to extract the thermal contact resistance between the CNT and substrate. We can estimate the smallest ${}^{SiN}R_c$ value that could generate an asymmetry consistent with our uncertainties by using a worst-case combination of these expectation values and confidence intervals and varying ${}^{SiN}R_c$ as a free parameter to obtain the same asymmetry within the theoretical model. Using a best-case combination of melting voltages would produce an upper bound on ${}^{SiN}R_c$, but such a combination produces a negative asymmetry and would thus predict and unphysical negative ${}^{SiN}R_c$. Thus, we can only meaningfully extract a lower bound on ${}^{SiN}R_c$. Also shown on the same plot is a second data set extracted from indium islands at a symmetric point on the opposite side of the heater wire. By comparison, it is readily apparent that there is no significant difference in melting distance on the two sides of the heater wire, indicating a high thermal contact resistance between the nanotube and the substrate.

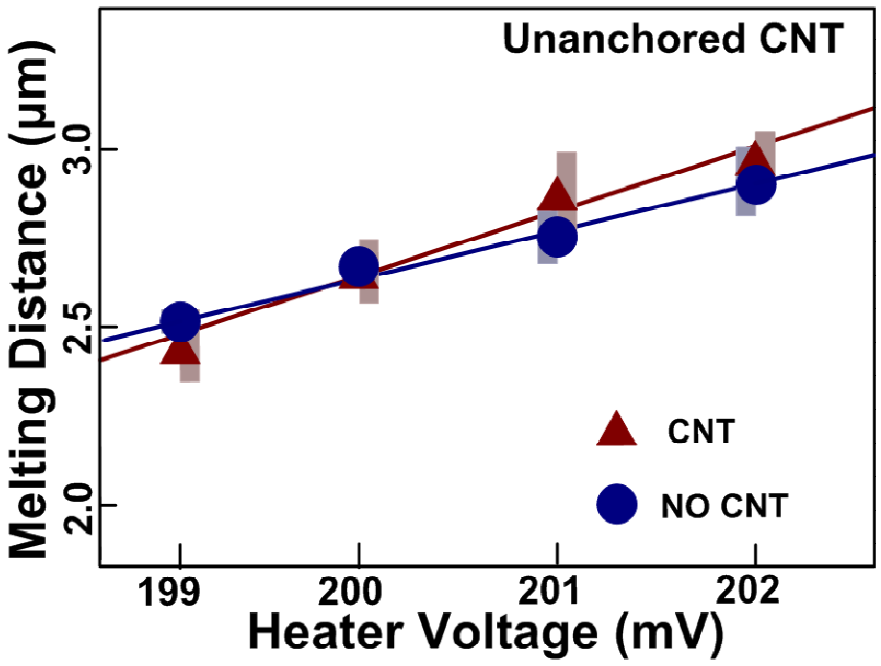

Figure 5.8 Plot of average distances (with standard deviation) at which the In islands melt for each given voltage, for un-anchored. The raw data are used to fit and extract 95% confidence intervals for the melting voltage. No quantitatively detectable asymmetry.

We can estimate the smallest ${}^{SiN}R_c$ value that could generate an asymmetry consistent with our uncertainties by using a worst-case combination of these expectation values and confidence intervals and varying ${}^{SiN}R_c$ as a free parameter to obtain the same asymmetry within a theoretical model. Modeling of the data is performed using the finite element analysis package Comsol. Combined electrical and thermal partial differential equations are used in an iterative solver. In the model, the working thermal equation is

$$\nabla.(\kappa\nabla T) - \frac{\Delta T}{R_c} + P = 0 \qquad (5.1)$$

where T is the local temperature,ΔT is the temperature difference between the CNT and the substrate, κ is thermal conductivity, $R_c$is the two dimensional thermal contact resistance of the CNT with the material it is contact with, and P is the power in the heater wire, given by $P = \sigma|\nabla V|^2$. In this relationship V is the electric potential, and $\sigma = \sigma_o(1 + \alpha\Delta T)^{-1}$, is the electrical conductivity, with σ_o the value at room temperature and α the temperature coefficient, both characterized previously. In the modeling, steady state conditions were assumed. Since the power source and thermal conductivity values were previously characterized, the only unknown parameter in equation (5.1) isR_c. A series of simulated thermal maps are obtained by choosing R_c as a free parameter. The contact resistance is extracted from the simulated thermal maps that match with the one obtained experimentally. Such a theoretically-predicted thermal map used to extract $^{SiN}R_c$ for the device being discussed is shown in Figure 5.9. Further details of modeling are explained in the Appendix at the end of this thesis.

In our modeling, we assume that the thermal contact between the Pd and SiN_x is perfect. Such interfaces are also known to exhibit thermal boundary resistance, but even in the worst case of two dissimilar materials (5.28), the temperature drop at this interface would be less than 10% of total temperature drop between the CNT and substrate.

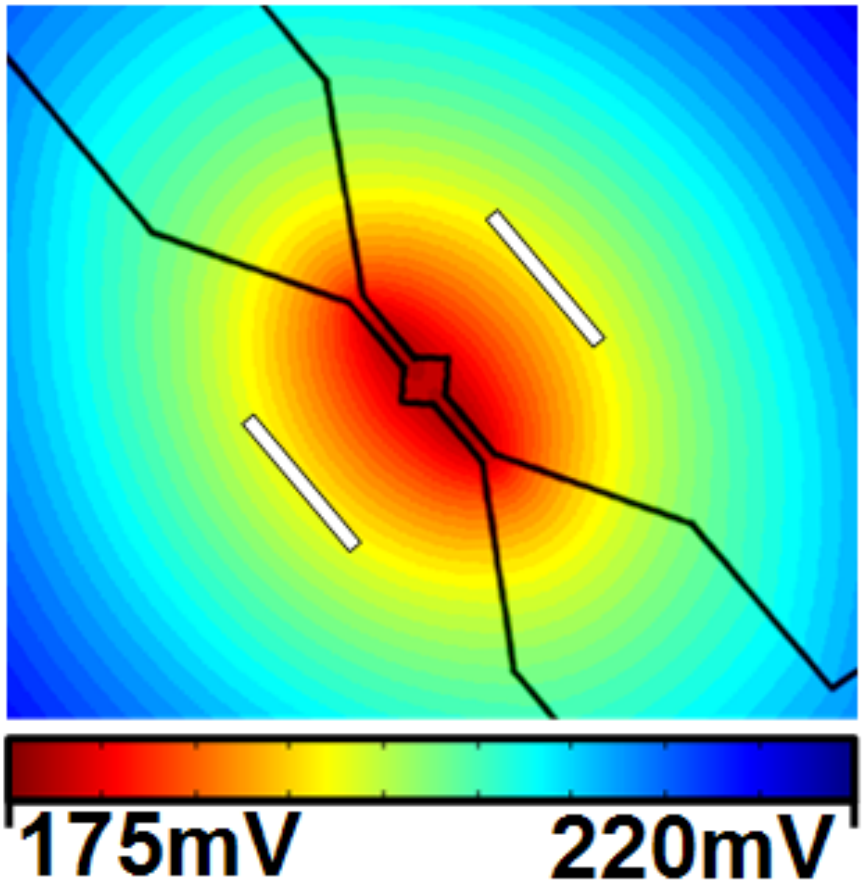

Figure 5.9 Simulated thermal maps obtained using finite element analysis. White lines equidistant from the center of the Pd heater wire are added as a guide to the eye for the detecting asymmetry. The thermal contact is extracted by comparing the simulations to the experimental data.

From these observations the ${}^{SiN}R_c$ value that we extract is 250 $m.K/W$. We can conclude that the asymmetry is smaller than this minimum-detectable level and that the ${}^{SiN}R_c$ value is therefore higher than this minimum. Thus, it is important to note that this value is a lower bound for ${}^{SiN}R_c$, and the actual value could be much higher than this. This is a high thermal contact resistance and it indicates that even though the nanotube and substrate are in intimate contact, there is effectively good thermal insulation between them.

An alternative explanation for this reduced asymmetry rather than a high R_c value might be a diminished thermal conductivity of the nanotube, as might be expected, for example, from electron-beam induced damage (5.29). However, other studies show that nanotubes retain their high thermal conductivities under similar temperatures and electron microscopy imaging conditions (5.30).

To further demonstrate that nanotubes retain high thermal conductivity in our experimental setup and to measure ${}^{Pd}R_c$, we make use of a second device designed to reduce the observed R_c value and provide a test of the high thermal conductivity of the nanotube. This is achieved by adding a second Pd thermal pad at the opposite end of the CNT as shown in Figures 5.4 c. As for the unanchored device, the Pd thermal pad located at the center of the heater wire facilitates the transport of heat into the CNT, while the other Pd thermal pad on the right side of the heater wire helps the CNT dispense heat more effectively into the substrate beneath. Figure 5.10 shows "as-captured" DF images at the specified applied voltages. Here, the middle of the heater wire is the hottest region, but unlike the un-anchored CNT case, a clear asymmetry can be seen.

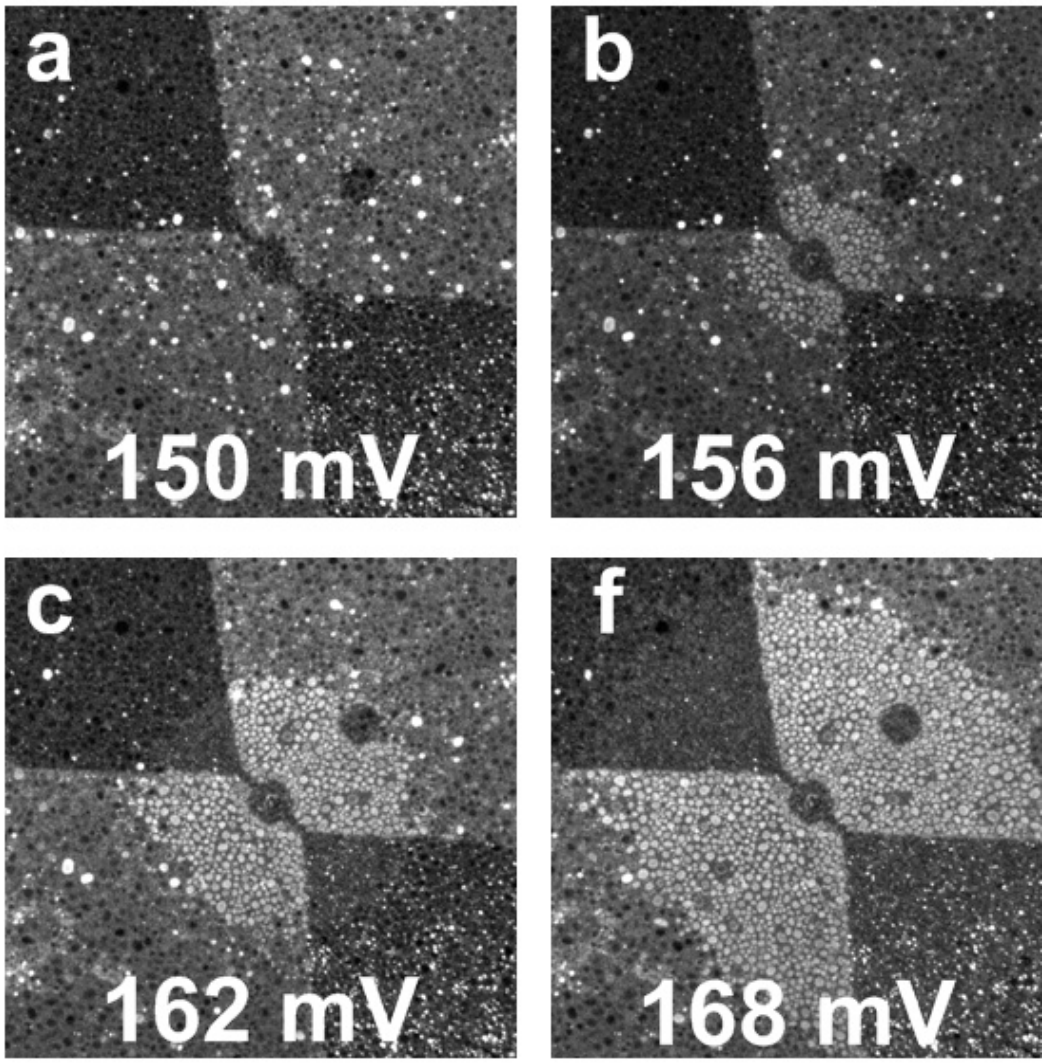

Figure 5.10 Experimental data of thermally anchored CNT device shown in Figure 4 (b). Imbedding CNT in Pd contacts improves the heat transfer between CNT and the substrate as can be seen in (b), (c) & (d).

As done earlier, these individual frames are used to compile a single thermal map by assigning colors to voltages at which each In island melts. Such a thermal map is shown in Figure 5.11. Clearly, thermal contours, obtained for this device in which the CNT is thermally anchored to the substrate through Pd, are asymmetric around the heater. The area around the Pd thermal pad to the right melts the In islands

at significantly lower voltages than an equidistant area on the left side, where there is no CNT.

.

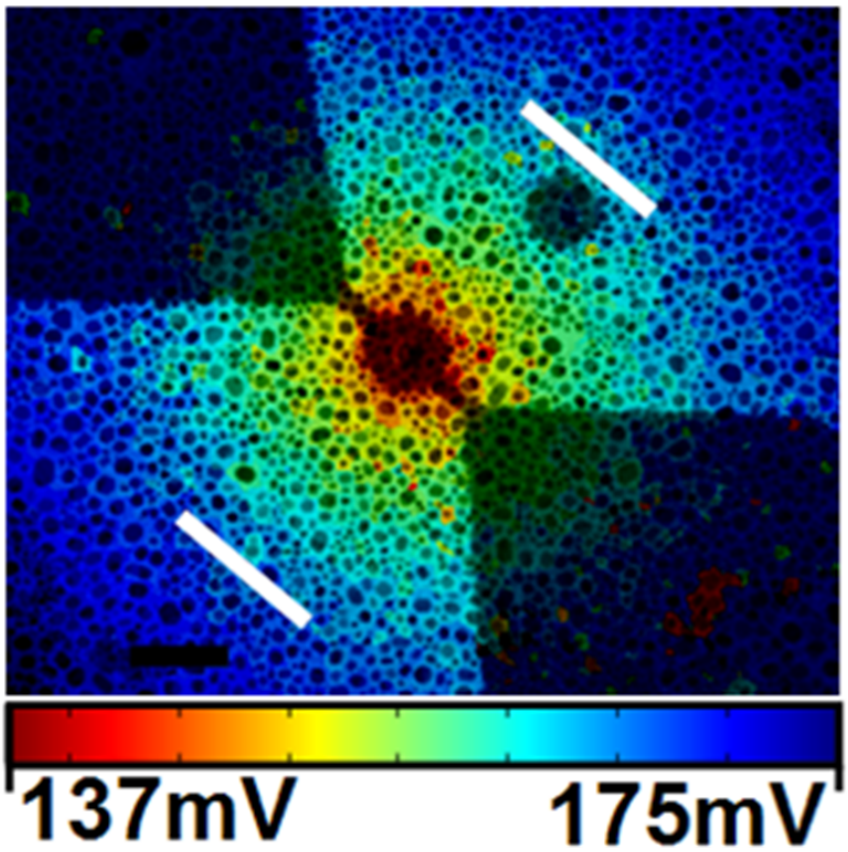

Figure 5.11 Experimental thermal maps for thermally anchored CNT obtained in the same way as the one shown in Figure 5.7 for unanchored CNT. Two white lines, parallel and equidistant from the center of the heater wire are added, as before to guide the eye to detect any asymmetry. It clearly shows the asymmetric melting of In islands on the two sides of the heater wire. At a given voltage, the melting of the islands goes further on the CNT side (above and right of the heater) than it does on the opposite side (below and left of the heater). This asymmetry is attributed to the presence of highly thermally conductive CNT and the low contact resistance at Pd contacts. The scale bars are 1 μm.

The relationship between melting voltage and distance from the heat source for a set of In islands near the Pd anchor and a symmetric point on the opposite side of the heater wire are plotted in Figure 5.13, where a clear difference can be seen between the two sides

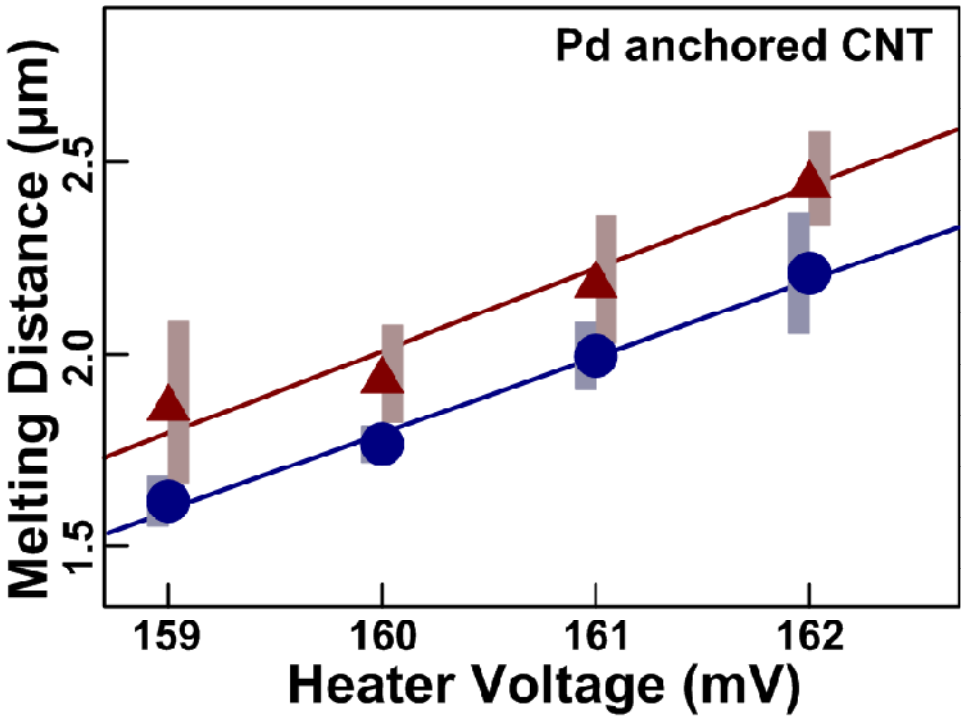

Figure 5.12 Plot of average distances (with standard deviation) at which the In islands melt for each given voltage for thermally anchored CNT. The raw data are used to fit and extract 95% confidence intervals for the melting voltage. Melting of In on the side of the heater where there is a CNT occurs at significantly lower voltages than on the other side. Thus demonstrating that thermal contact resistance of a CNT can be manipulated by increasing its area of contact.

As before, expectation voltages and 95% confidence intervals are determined by linear regression, and finite-element modeling is used to extract a value of ${}^{Pd}R_c$. However, in this case, the confidence intervals are completely non-overlapping, reflecting the strong asymmetry we observe, and we therefore can extract an expectation value with upper and lower bounds on the thermal contact resistance, as ${}^{Pd}R_c = 4.2^{+5.6}_{-2.1}\ \ m.K/W$. Figure 5.13 shows a voltage map from the modeling, showing an asymmetry comparable to the experimental voltage map.

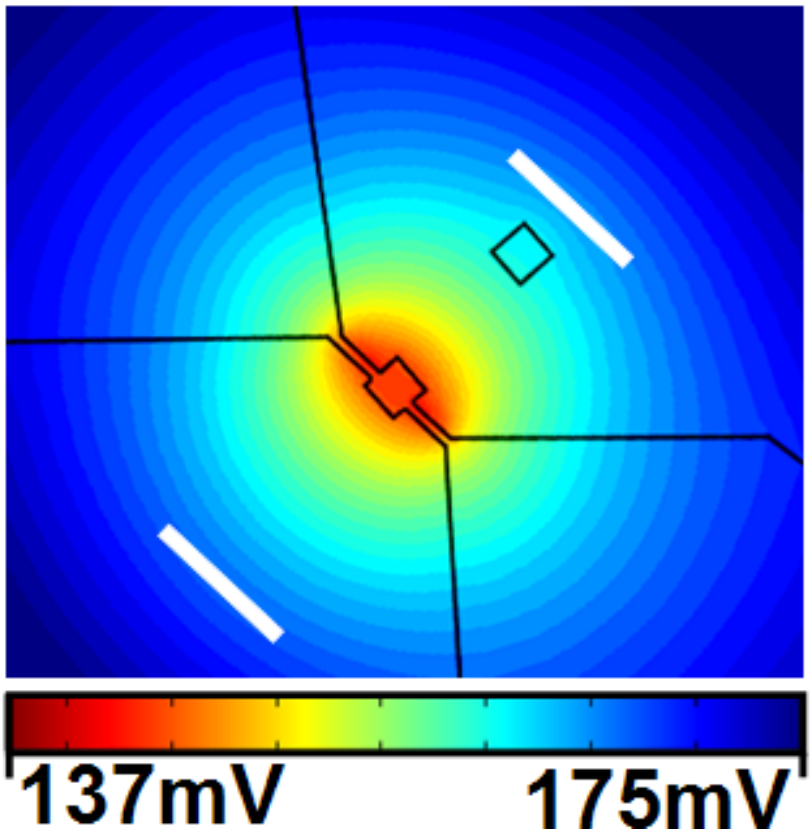

Figure 5.13 Simulated thermal map obtained by finite element modeling for thermal anchored CNT. Consistent with the experimental data, the isothermal contours are not symmetric. As before the parallel white lines, equidistant from the heater wire are added as a guide to the eye.

This low value for ${}^{Pd}R_c$ by itself demonstrates that the nanotube must have high thermal conductivity and thus is not affected significantly by beam damage, justifying the value used in the modeling above of K_{CNT} = 3000 W/m.K (5.2). However, we may alternatively estimate a minimum thermal conductivity of the CNT consistent with our results by assuming an unrealistically small ${}^{Pd}R_c$ value of 0.1 m.K/W (derived from other measurements of the thermal boundary resistance for a single-layer of graphene (5.33)). Using this, we estimate that the minimum thermal conductivity for the CNTs in this study is at least 500 W/m.K. This is still a relatively high value and would only modify the lower bound on ${}^{SiN}R_c$ from modeling the one-contact data above from 250 to 120 m.K/W, which is still substantially higher than most of the previously reported estimates, despite being only an excluded lower bound consistent with our results above.

The observation that the asymmetric melting of the In islands occurs only when two Pd thermal contacts are deposited on either end of the CNT and the fact that the ${}^{SiN}R_c$ and ${}^{Pd}R_c$ differ by more than an order of magnitude both support our assertion that manipulating the effective contact width can substantially change the thermal contact resistance. It is important to mention here that all data were acquired under imaging conditions such that the heating due to the electron beam was not a factor. Independent measurements using a specimen holder with a calibrated heat source and thermocouple confirm that beam heating at high illumination intensity can increase the sample temperature by tens of °C, but the beam conditions used here produce heating that is immeasurably small within the resolution of the heating holder, namely less than 1°C.

If we assume a model in which R_c is inversely proportional to the contact width, we expect that the higher contact area of CNT anchored to the Pd metal would give lower thermal resistance than when it is lying on the substrate, as indicated in the schematic in Figure 5.4 d. For multiwall CNTs, there are inherent difficulties in defining a contact width between the CNT and the substrate. In fact, mechanical modeling predicts almost no flattening for a CNT of the sizes we report here, when van der Waals bonded to a flat substrate (5.32). Nevertheless, for the sake of estimation, we can define the contact width as that part of the circular nanotube cross-section which comes within 0.1 nm of the substrate, assuming that the bottom of the nanotube is perfectly in contact. Using this definition, we calculate an effective contact width between the CNT and the substrate of 2.4 nm. However, underneath the Pd contact we expect the contact width to be approximately half the circumference of the nanotube, or $\pi r \approx 24$ nm. This puts ${}^{SiN}R_c$ at least 10 times larger than ${}^{Pd}R_c$, which is consistent with our observed lack of asymmetry in the thermal maps of Figures 5.6 & 5.7 and demonstrates a reliable thermally-insulating support for multiwall carbon nanotubes. The exact contact area of the nanotube and the SiN_x would require considerations of the surface roughness of the substrate and the mechanical interactions of the nanotube, which are outside the scope of this dissertation. However, we note that the membranes have very low surface roughness (< 8 Å RMS) and the basic result is the same even when the the experiment is repeated with the nanotube on the back side of the membrane (Figure 5.14), which is expected to have an even lower roughness, comparable to the parent Si wafer on which it was grown.

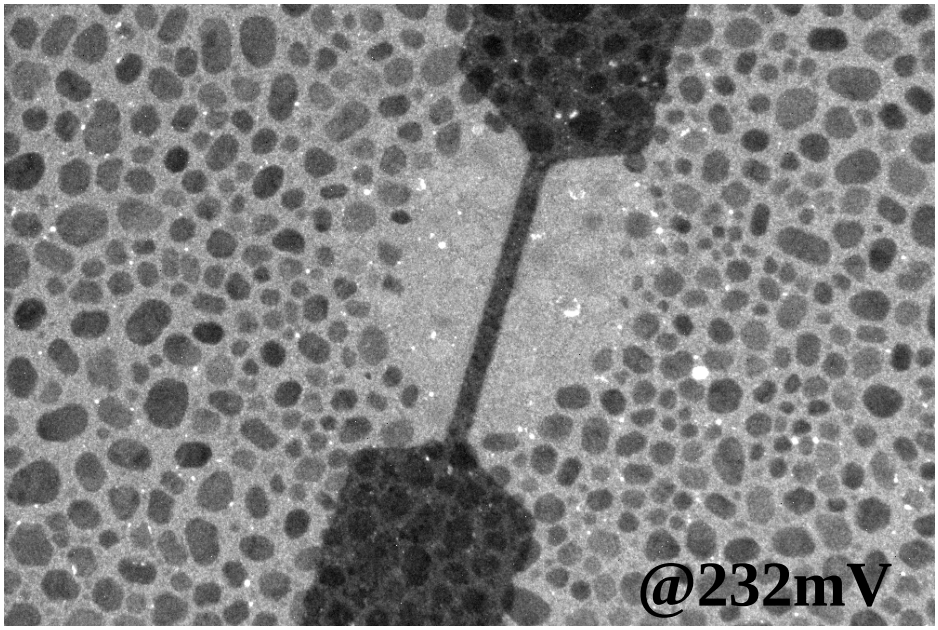

Figure 5.14 The back side of freestanding SiNx substrates are expected to be smoother than the free side because the film grows on SiO_2 wafer. Even in the situation, where the CNT is on the back (smoother) side, no asymmetry is observed. This suggests that surface roughness is not the reason for our very high thermal contact resistance.

It is also instructive to compare the thermal conductivity and electrical conductivity of the CNT-Pd contacts to determine whether the enhancement of thermal transport may be electron-mediated. In electrical devices fabricated with similar geometries (discussed in the next chapter), we routinely see an electrical contact resistance of approximately 10 kΩ, consistent with other findings (5.33). Using the Wiedemann-Franz law, we thus estimate a thermal conductance from electrons of 10^{-9} W/K. This value is two orders of magnitude smaller than our modeled thermal conductance of 1.2×10^{-7} W/K at the contacts. Thus, the heat transfer between the CNT and Pd is believed to be phonon-mediated.

In further considering these results, it is important to note an apparent inconsistency with other studies showing a smaller contact resistance for a CNT

adhered to a substrate (13, 18-25). However, many of these studies use SEM imaging (5.13, 5.19, 5.24, 5.25) which is known to deposit significant amounts of carbonaceous material onto CNTs during imaging (5.34). This material may reduce R_c in the same manner that Pd does here. Similarly, other studies use a CNT manipulation-and-placement routine that explicitly calls for embedding the CNT in an acrylic adhesive (5.2. 5.35). For other studies that do not use SEM imaging or other adhesive coatings (5.18, 5.20, 5.21, 5.23) the measurements are performed at elevated temperatures, where near-field thermal radiation (5.36) may be playing a significant role in the transport phenomena, reducing the observed R_c value. The results we report here do not use SEM imaging or adhesives, are well-characterized by TEM to exclude the possible presence of gross amounts of contaminating materials, and are carried out at relatively low temperatures, where thermal radiation effects are not expected to play a role in the transport. Thus, the R_c values we report here are obtained with high confidence and without mitigating factors.

In summary, we demonstrate that the thermal coupling between a CNT and its mechanical support can be manipulated. In fact, through this study we have shown that thermal nature of mechanical supports of a MWCNT should no longer be a limiting factor in utilizing CNTs for thermal applications. This result should aid in the future engineering of CNTs for thermal devices.

REFERENCES

5.1 J. Hone, B. Batlogg, Z. Benes, A. T. Johnson, and J. E. Fischer, Science 289, 1730 (2000)

5.2 P. Kim, L. Shi, A. Majumdar, and P. L. McEuen, Phys. Rev. Lett., 215502 (2001)

5.3 M. J. Biercuk, M.C. Llaguno, M. Radosavljevic, J.K. Hyun, A. T. Johnson, and J.E. Fischer, Appl. Phys. Lett. 80, 2767–2769 (2002)

5.4 J. Hone, M.C Llaguno, M.J. Biercuk, A.T. Johnson, B. Batlogg, Z. Benes, J.E. Fischer, Appl. Phys. A 74, 339-343 (2002)

5.5 S. Berber, Y. K. Kwon, and D. Tomanek, Phys. Rev. Lett. 84, 4613 (2000)

5.6 E. Pop, D. Mann, Q. Wang, K. Goodson, and H. J. Dai, Nano Lett. 6, 96 (2006)

5.7 S. Maruyama, Physica B 323,193 (2002)

5.8 D. J. Yang, Q. Zhang, G. Chen, S. F. Yoon, J. Ahn, S. G. Wang, Q. Zhou, Q. Wang and J. Q. Li, Phys. Rev. B 66, 165440 (2002)

5.9 T .Y. Choi, D. Poulikakos, J. Tharian, and U. Sennhauser, NanoLett. 6, 1589 (2006)

5.10 M. Fujii, X. Zhang, H. Q. Xie, H. Ago, K. Takahashi, T. Ikuta, H. Abe, and T. Shimizu, Phys. Rev. Lett. 95, 065502 (2005)

5.11 C. H. Yu, L. Shi, Z. Yao, D. Y. Li, and A. Majumdar, NanoLett. 5, 1842 (2005)

5.12 J. P. Small, K. M. Perez, and P. Kim,Phys. Rev. Lett. 91, 256801 (2003)

5.13 I. K. Hsu, R. Kumar, A. Bushmaker, S. B. Cronin, M. T. Pettes, L. Shi, T. Brintlinger, M. S. Fuhrer, and J. Cumings, Appl. Phys. Lett. 92, 063119 (2008)

5.14 B. Li, L. Wang and G. Casati, Phys. Rev. Lett.93, 184301 (2004)

5.15 B. Li, L. Wang and G. Casati, Lett. 88, 143501 (2006)

5.16 R. S. Prasher, X. J. Hu, Y. Chalopin, N. Mingo, K. Lofgreen, S. Volz, F. Cleri, and Pawel Keblinski, Phy. Rev. Lett. 102, 105901 (2009)

5.17 L. Shi, App. Phys. Lett. 92, 206103 (2008)

5.18 H. Maune, H. Y. Chiu, and M. Bockrath, Appl. Phys. Lett. 89, 013109 (2006)

5.19 C. H. Yu, S. K. Saha, J. H. Zhou, L. Shi, A. M. Cassell, B. A. Cruden, Q. Ngo, and J. Li, J. Heat Transfer 128, 234-239 (2006)

5.20 A. W. Tsen, L. A. K. Donev, H. Kurt, L. H. Herman and J. Park, Nature Nanotechnology 4, 108 - 113 (2008)

5.21 H-Y. Chiu, V. V. Deshpande, H. W. Postma, C. N. Lau, C. Miko, L. Forro, M. Bockrath, Phys. Rev. Lett. 95, 226101, (2005)

5.22 A. Javey, J. Guo, M. Paulsoson, Q. Wang, D. Mann, M. Lundstorm, H. Dai, Phys. Rev. Lett. 92, 106804 (2004)

5.23 E. Pop; D. A. Mann, K. E. Goodson, H. Dai, J. of Appl. Phys. 101, 093710 (2007)

5.24 P. Kim, L. Shi, A. Majumdar, P. L. McEuen,Physica B 323, 67-70, (2002)

5.25 L. Shi, J. Zhuo, P. Kim, A. Batchtold, A. Majumdar, P. L. McEuen, J. Appl. Phys. 105, 104306 (2009)

5.26 M.T. Pettes,L. Shi, Adv. Funct. Mater. (2009), 19, 3918-3925

5.27 G. L. Allen, R. A. Bayles, W. W. Gile,and W. A. Jesser, Thin Solid Films 144(1986)

5.28 N. G. Chopra, L. X. Benedict, V. H. Crespi, M. L. Cohen, S. G. Louie and A. Zettl, Nature 377, 135-138 (1995)

5.29 G. E. Begtrup, K. K. Ray, B. M. Kessler, T. D. Yuzvinsky, H. Garcia and A. Zettl, Phys. Rev. Lett. 99, 155901 (2007)

5.30 Z. Chen, W. Jang, W. Bao, C. N. Lau, and C. Dames. App. Phys. Lett. 95, 161910 (2009)

5.31 T. Hertel, R. E. Walkup and P. Avouris, Phys. Rev. B, 58, 20 (1998)

5.32 *M. S. Purewal*, *B. H. Hong*, *A. Ravi*, *B. Chandra*, *J. Hone*, and *P. Kim*, Phys. Rev. Lett. 98, 186808 (2007)

5.33 M. F. Yu, O. Lourie, M. J. Dyer, K. Moloni, T. F. Kelly, and R. S. Rouff, Science 287, 5453 (2000)

5.34 H. Dai, J. H. Hafner, A. G. Rinzler, D. T. Colbert, and R. E. Smalley. Nature 384, 147 (1996)

5.35 S. Shen, A. Narayanaswamy, and Gang Chen., Nano Lett. 9, 8, (2009)

Chapter 6

Mutiwalled Carbon Nanotube Devices

6.1 Joule heating in Carbon Nanotube

We studied joule heating in the CNTs by passing electrical current through them. The schematic of a typical device employed for this purpose is shown in Figure 6.1. In such a device a metallic CNT resting on SiN_x, makes top electrical contact with Pd electrodes. As discussed in the previous chapter, the imbedding of CNT under metal contacts ensures a larger area of contact and thus a lower thermal contact resistance ($^{Pd}R_c$) compared with that with the substrate ($^{SiN}R_c$).

The device fabrication process is similar to what was explained in chapter 5. There is, however, one additional step of plasma etching that is employed to rid of any lithography and CNT-deposition residues. The plasma etching is done in a TRION system available to the author, which can reliably sustain a plasma at a low power of 8W. The chamber is purged with 5 sccm of O_2 to maintain a constant pressure of 150mTorr. Lithography-done samples (prior to Pd deposition) are exposed to such a plasma for 60-90 seconds. The etching done this way is very mild which improves the two terminal electrical resistances of our devices from a few MΩ to 5-35 kΩ and is also expected to similarly assist in

improving thermal conduction without significantly damaging the CNTs. A schematic of device geometry is shown in Figure 6.1 and a high resolution TEM image of the actual device prior to In deposition is shown in Figure 6.3 (a). Before discussing the data acquired by employing this device it is instructive to present results of finite element modeling.

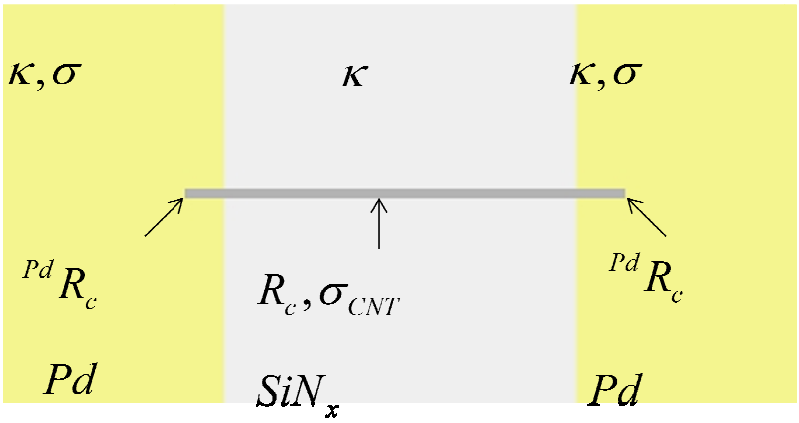

Figure 6.1 Schematic of device fabricated for studying joule heating in a MWCNT. Current is passed through a metallic CNT having Pd electrodes.

Simulations were carried out using the geometry of the actual device. This modeling exercise was done at two extremes of lowest and highest $^{SiN}R_c$ values reported in the literature i.e. the R_c values reported by Maune *et. al.* (6.1) and Tsen *et. al.* (6.2). Since neither of these two studies report thermal contact resistance between metal and CNT ($^{metal}R_c$), we calculated it from reported R_c of CNT with the reported Substrate $^{Subs}R_c$ value. Given the larger area of contact, it is reasonable to assume that $^{metal}R_c$ is fifty times smaller than the $^{Subs}R_c$. Thus for

Maune *et. al* and Tsen *et. al.*, $^{metal}R_c$ should be 0.012 m.K/W and 0.2 m.K/W respectively.

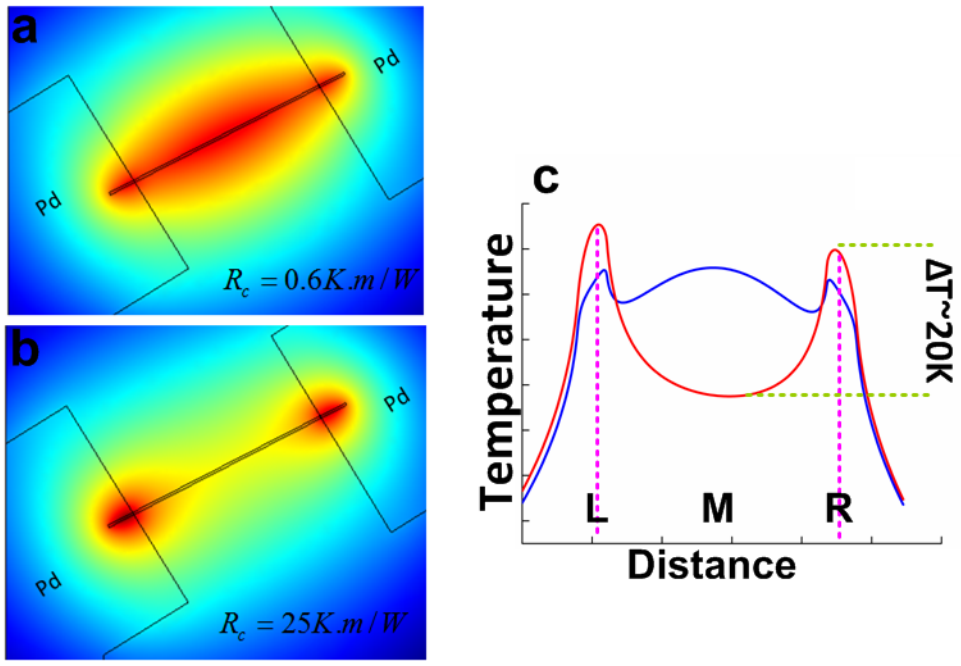

Figure 6.2 Simulated thermal maps of a biased CNT (a) using the lowest thermal contact resistance value (b) using the highest value reported in literature. It is to be noted that the temperature profiles are very different for the two thermal contact resistance values used in the simulations. For qualitative analysis (c) shows temperature profiles along the length of CNT. The blue curve corresponds to the case when R_c =0.6 m.K/W was used, whereas the red curve is obtained when R_c =25 m.K/W is used in the simulations. Dotted pink lines are drawn at the positions where the Left (L) and Right (R) contacts are along the length of the CNT. It can be seen here that for the higher R_c value (red curve) the contacts are significantly hotter than the Middle (M) of the CNT. Even though for the lower R_c value, the contacts appear to be at slightly higher temperature (blue curve) than the point M, such a temperature drop along the length of CNT is below temperature resolution of our technique.

The simulated thermal maps thus obtained are shown in Figures 6.2 (a) and 6.2 (b). By looking at these maps it is apparent that thermal profile of CNT depends strongly on the R_c values. In the case of Figure 6.2 (a), the CNT appears to be at a uniform

temperature whereas, the thermal map of Figure 6.2 (b) shows that for the R_c values used there, the contacts would get hot first.

Temperature versus distance along the length of CNT plot for the two R_c values under discussion are shown in Figure 6.2 (c). As before, for the higher R_c (Tsen *et. al.*) the simulated plot shows that the temperature difference between the points M, L and R contacts of CNT is significant. However, for the smaller R_c (Maneu *et. al.*) while the contacts still slightly hotter than point M, the temperature difference between C and ends is below the resolution of EThM.

For the CNTs used in our studies measured ${}^{SiN}R_c$ is ten times the Tsen *et. al*. value. Thus in our measurements the heating of contact should be more profound and this should manifest itself easily in the form of In on the contacts melting before that at the mid or the entire region that is not imbedded under Pd.

The experimental data are collected by employing EThM. The voltage applied along the two ends of the MWCNT is ramped in 10mV steps and, as before, a MATLAB script is used to capture the DF images at each applied voltage. The data for this experiment are shown in Figure 6.3. It can be seen that contrary to what was expected in light of simulations performed for two extreme R_c values, than melting of In in this data set starts at the center of the CNT. While our data does not match (even qualitatively) to either results of the simulations shown in Figure 6.2, it resembles more closely to the simulations for Maune *et. al*. suggesting that that the thermal contact resistance of CNT used in this device be close to ${}^{SiN}R_c \sim 0.6$ K.m/W and ${}^{Pd}R_c \sim 0.012$ K.m/W. However, as discussed in the previous chapter, these values are completely excluded by our measurements. Thus, we see a contradiction

in our model when applied simultaneously to the data of chapter 5 and the data presented here. It is to be noted that Maneu et. al. extracted the R_c by electrical break down method, which is at a higher temperature (~600 ^oC) than the melting point of Indium (~156^oC) used here. This means that R_c measured through self-heating a CNT apparently differs by more than two orders of magnitude from the values that when the CNTs are remotely heated by a Pd heater wire.

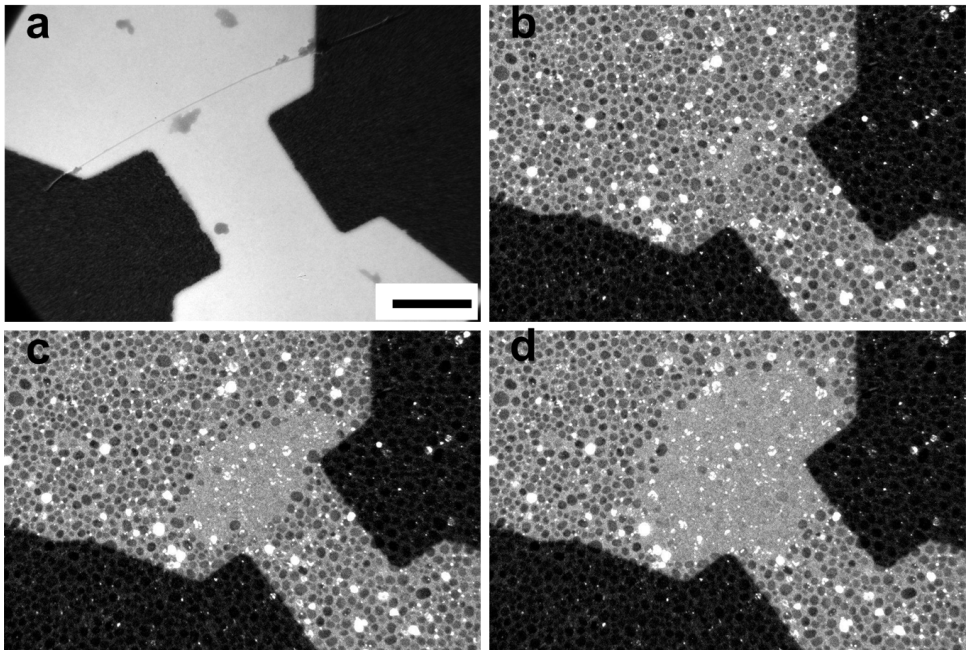

Figure 6.3 High resolution TEM image of the device and the data of Joule heating in CNT. The TEM image of a device with MWCNT is shown in (a). (b), (c) and (d) are the data acquired when 1.94V, 2.04V and 2.14V are applied across the CNT. Clearly, the melting occurs at the center of CNT first. The melting profiles of our data resemble (qualitatively) to the simulations carried out by using Rc=0.6 K.m/W as shown in Figure 6.2 (a). As shown in the previous chapter, such a low value is completed excluded for our CNTs, within the model developed. The scale bar is 1 μm.

This led us to suspect that there might be other modes of heat transfer like thermal radiation (6.3) or near-field thermal radiation (6.4) when the CNTs are heated by passing current through them. It is also possible that the hot electrons in the CNT the electrons scatter off the phonons in the substrate (6.5). To investigate it further we present an ongoing research project in which current is passed through a part of the CNT and see if the CNT is at higher than assumed temperatures or not.

6.2 Investigating modes of heat transfer in Self-heated Carbon Nanotubes

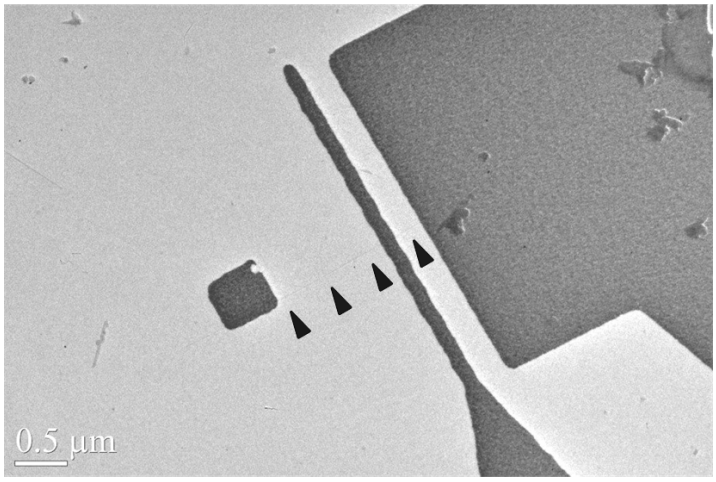

Figure 6.4 High resolution TEM image of the device fabricated to understand modes of heater transfer in a CNT when operated by a direct current. The current flows through just a short segment of CNT (~450nm)between one thin and one wide electrode. To ensure proper thermal anchoring of the un-operated part of the CNT to the substrate a small Pd patch is added. This geometry will provide insight into whether or not there is any variation along the entire CNT.

To understand the physical mechanism that is responsible for thermal transport when current is passed through the CNT we design a device in which current flows through a part of the CNT as shown in the Figure 6.4, where it can be seen there that current can flow through just a short segment of CNT.

The choice of one Pd electrode on the right in Figure 6.4 to be wide and the second electrode to be wire-thin is to ensure a robust thermal anchoring on the right. The isolated contact (referred to as remote Pd patch from here on) on further left is added to improve the thermal coupling between CNT and the substrate. While here we only discuss data taken for such a device, measurements were done on samples with and without this remote Pd patch. Both types of samples yielded identical results.

As done in previous studies, we ramp the voltage in 1mV steps. A few dark field images captured at specified voltages are shown in Figure 6.5. It is obvious that the melting of In starts in the middle of the active region and the melting profile is centered around that region. In our preliminary analysis we note that the segment of the CNT through which no current was passed shows no significant heating of the substrate underneath. If the entire CNT was at the same temperature, we would have observed the melting of the In at the remote contact at lower voltages. Another interesting observation is that melting profile is roughly circular about the operated region of CNT. If the CNT was being heated by the current, we would expect to see the In near the remote contact to melt at lower voltages than for other locations at the same distance from the source.

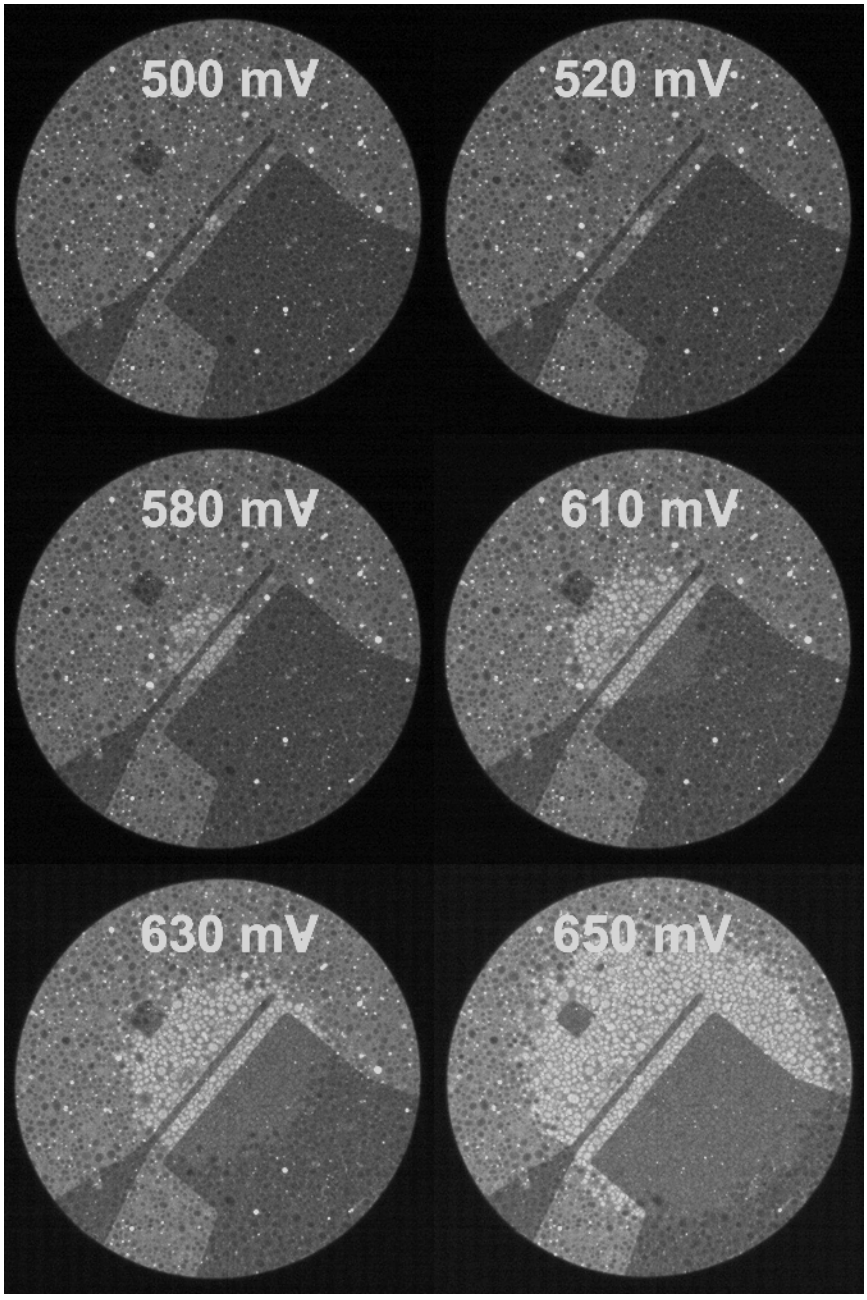

Figure 6.5 Data acquired (at the specified voltaged) in TEM showing that the CNT gets hot only in the region in which the current passes. The melting of the In even at 650mV is centered around that region.

To qualitatively understand this data we carry simulations (shown in Figure 6.6) using a model geometry which is similar to the geometry of the device and using parameters extracted from previous studies (chapter 5). The results of these simulations show (Figure 6.6 (a)) a melting profile in which the entire CNT, not just the operated segments, gets hot, different from what is observed in experiments.

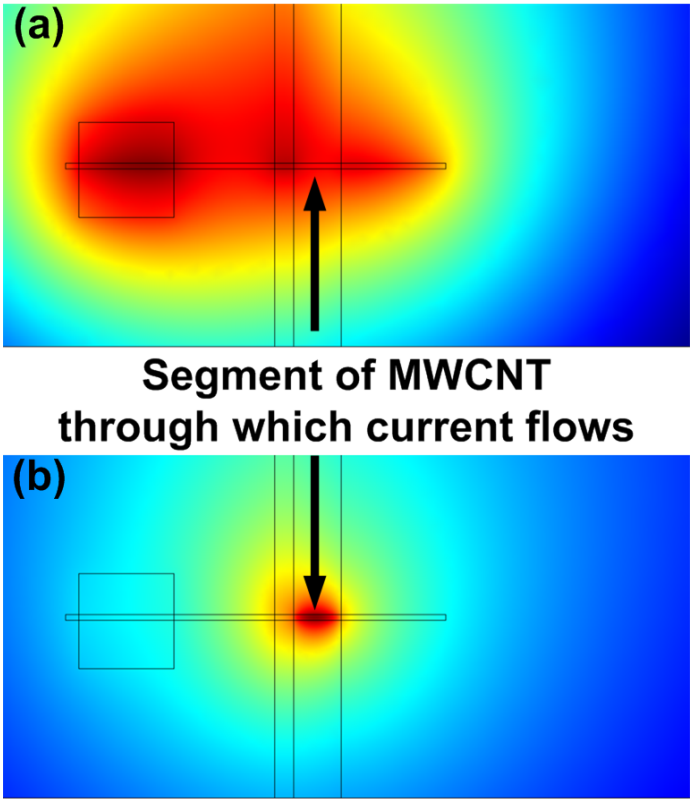

Figure 6.6 Simulations of a device in which current is passed through just a small segment of CNT. While (a) is obtained by assuming the standard joule heating model, this thermal map does not match well to the data. (b) matches data better but is obtained by considering a non-physical case of power being generated in SiN_x , instead of in the nanotube.

Cursory modifications of the parameters show that it is difficult to construct a model that simultaneously predicts the current results and those of Chapter 5. However one surprising modification to the model shows excellent qualitative agreement. When we perform the simulations by assuming that somehow there is

power generated in the substrate instead of in the nanotube, the simulated maps show that the operated region gets hot first, matching the experimental results. This is apparently an unphysical model but these results could most straightforwardly be explained by assuming that hot electrons in the CNT are inelastically scattered off by the phonons in the dielectric layer. In order to draw a robust conclusion, however, a detailed quantitative analysis is required.

6.3 Future Work

In the immediate future the aim is to explore if remote scattering is a necessary component of a unique and complete model needed to explain the data presented above. This will require a more detailed and careful analysis and modeling of the most recent data. An alternate model can be constructed based upon a very low thermal conductivity for the CNTs (less than approximately 100W/K. m). Experiments are ongoing to test this possibility by constructing devices that are highly sensitive to the thermal conductivity of the nanotube. Also, It will be instructive to repeat the same experiment but with a device in which the operated region of CNT is suspended instead of resting on SiN_x, whereby remote scattering would presumably be suppressed.

A long term aim of this field is to make thermal logic devices (6.6, 6.7) from CNTs (6.8). For this purpose it will be important to understand a temperature dependence of Rc and thermal behavior of CNT-CNT junctions. Electrical properties of such cross CNTs have been studied (6.9) but thermal behavior of such a device remains to be explored.

References

6.1 H. Maune, H. Y. Chiu, and M. Bockrath, Appl. Phys. Lett. 89, 013109 (2006)

6.2 A. W. Tsen, L. A. K. Donev, H. Kurt, L. H. Herman, and J. Park, Nat. Nanotechnol. 4, 108 (2009)

6.3 Y. Fan, S. B. Singer, R. Bergstrom, C. Regan, Phys Rev Lett, 102 (18), 187402 (2009)

6.4 S. Shen, A. Narayanaswamy, and G. Chen. Nano Lett. 9, 2909, (2009)

6.5 V. Perebeinos, S. V. Rotkin, A. G. Petrov, and P. Avouris, Nano lett. 9, 1, 312 (2009)

6.6 B. Li, L. Wang, and G. Casati, Phys. Rev. Lett. 93, 184301 (2004)

6.7 B. Li, L. Wang, and G. Casati, Appl. Phys. Lett. 88, 143501 (2006)

6.8 C.W. Chang, D. Okawa, A. Majumdar, and A. Zettl, Science 314, 1121-1124 (2006)

6.9 M. S. Fuhrer, A. K. L. Lim, L. Shih, U. Varadarajan, A. Zettl, and P. L. McEuen, Physica E 6, 868 (2000)

Appendix

A.I.1. Comsol Modeling

The Comsol 3.5a software that we employ in our simulations comes with many pre-defined modules in which working equations are already set-up. Instead of having a script-based command system, the boundary conditions and the sub-domain settings can be fed in the model via graphical user interface. Once the geometry is defined the electrical properties and thermal properties can defined in separate layers. Thus, by choosing appropriate built-in modules – which have predefined, yet customizable to the physical situation at hand, working equations; we can carry out simulations after putting in the values of variables such as thermal & electrical conductivities of the various components of the geometry, initial temperature and bias conditions etc. into the model. The first step is to define the geometry in Comsol. The geometry can be defined by importing the Design CAD file into the Comsol or by putting in the coordinates of each point. Every segment of the geometry is characterized through the properties of the material it represents in Comsol by defining "sub-domain" settings in the software. Once this is done we, based on the physical situation, define the correct boundary conditions (see Figure A.I.1).

In our Comsol analysis, we set-up our model so that it has three layers, one electrical and two thermal. Two thermal layers are important because in our experiments we measure the temperature of SiN_x membrane (represented by the temperature layer T1) by directly observing the solid to liquid phase transition of In islands while the temperature of the CNT (represented by temperature layer T2) is

not measured directly in our experiments. Thus our simulations not only give the temperature of the substrate but enable us to infer that of the CNT as well.

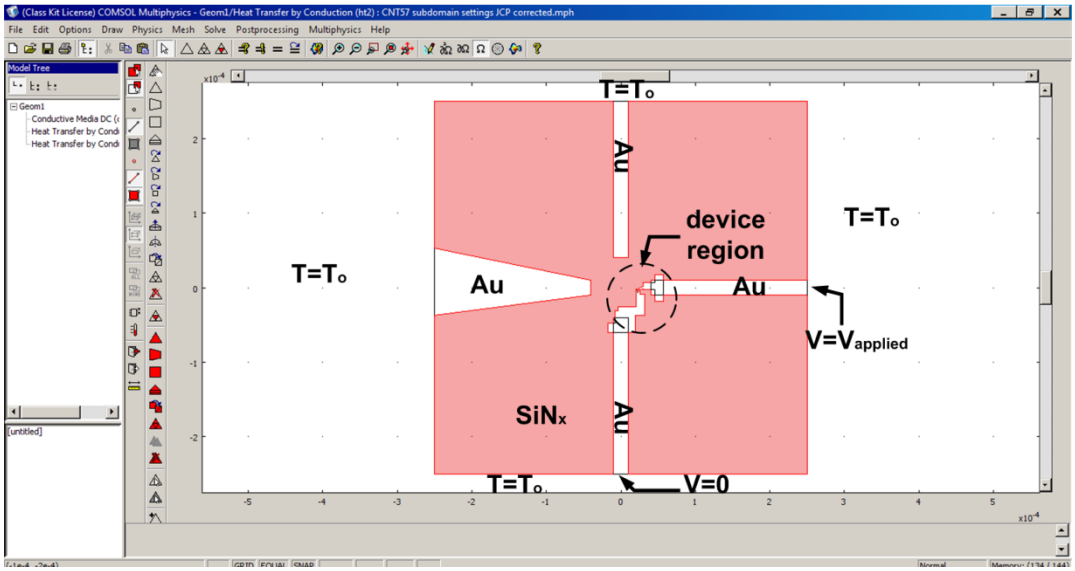

Figure A.I.1 Defining Geometry and Boundary conditions in Comsol. The simulations are carried out over the whole suspended SiN_x membrane window, the boundaries of which are assumed to be at room temperature, To.

In the electric-conduction layer, the electrical properties of all the components in the model, namely Au-leads, Pd contacts & heater wires, CNT and SiNx are defined. Given that the biases applied are too low to significantly heat the Au leads, we neglect the temperature dependence of the electrical resistance of the Au. The sheet resistance of Au leads, measured by using four-probe Van der Pauw method to be 1.048 Ω, can be converted to resistivity by multiplying it to an arbitrary thickness of 100 nm. All the physical parameters in our modeling were normalized to this length scale except the electrical conductivity of Pd, which is determined by matching the current density through the heater wire in the model to that measured experimentally at the lowest applied bias. The temperature dependence of the electrical conductivity, defined in Comsol by the equation $\sigma = \sigma_o(1 + \alpha(T1 -$

$T_o))^{-1}$, where α the temperature coefficient is accounted for by using α as a free parameter in matching the current density in Comsol at high bias to the experimental value at that applied voltage. Due to its electrically insulating nature, the substrate is assumed to have a very high electrical resistance of 1GΩ.

In first of the two "heat transfer by conduction" layers, defined by temperature T1 in Comsol, we calculate the thermal conductivities of Au and Pd by using Wiedemann-Franz law. For the extraction of thermal contact resistances, simulated maps are obtained at two extremes of the 95% confidence intervals of melting voltages at the two sides of the heater wire (one where the CNT is present and the other side where there is no CNT), as described in section 5.3 of this dissertation. The thermal conductivity of the substrate is calibrated by making it a free parameter in the simulated maps obtained at the voltages obtained experimentally for the side where no CNT was present in the experiment. The thermal contact resistance is chosen to be a free parameter in the simulated maps which are obtained at voltages extracted from the experiments for the side of the heater wire where CNT is present (refer to the section 5.3 of this dissertation). Thus iterations between the two sides give us the thermal conductivity of the SiN_x and the thermal contact resistance, simultaneously. Note that the thermal conductivity of the substrate is calibrated independently for each experiment described herein.

The second of the two "heat transfer by conduction" layers, defined by temperature T2 in Comsol, contains only CNT in the model. Because we expect the temperature gradient in our measurements to be not more than 50 ^{o}C and for the sake of simplicity, we take the thermal conductivity of the CNT to independent of

temperature. While the 3-d value of thermal conductivity of CNT, found in literature is 3000 W/m.K (Kim *et. al*., Phys. Rev. Lett. 87, 215502 (2001)), this values needs to be normalized to a 2-d value that goes into Comsol. Thus the appropriate thermal conductivity of the CNT to be used should be;

$$\frac{3000\ (W/m.K) \times \pi(7.5(nm))^2}{15(nm) \times 100(nm)}$$

where $7.5\ nm$, is the radius of CNT as measured by TEM; $15\ nm$ is the dimensions of the CNT (same as the diameter) in Comsol model; and $100\ nm$ is the arbitrary thickness to which all the 3-d values are normalized.

A.I.2 Comsol Modeling (Mesh Study)

The simulations were carried out by employing finite element analysis. In finite element analysis the geometry is divided by a triangular mesh and the predefined equations are solved for each mesh element. The final solution is obtained by integrating the solution from every mesh element for the whole geometry. Due to the flexibility in customizing the mesh we employed the commercially available software Comsol 3.5a available in the Engineering Labs on campus.

Initial simulations were done by the script-based software called FlexPDE. While scripting in FlexPDE we did not have the ability to choose the mesh size. Consequently, the software gave errors if any part of the device geometry was orders of magnitude smaller than the largest parts. More specifically, the software failed to converge the solution for our devices that involved CNTs, because the diameter of

CNT was several orders of magnitude smaller than the other components of the device.

Element growth rate **(Resolution of narrow regions)**	No of mesh elements **(Degrees of freedom solved)**	Reliable Solution? (Unreliable when re-meshing gave a variation of 0.5%-20% in derived values)
1.6 **(1.0)**	4355 **(26334)**	No
1.7 **(1.0)**	6549 **(39498)**	No
1.9 **(1.0)**	5999 **(36198)**	No
2.1 **(1.5)**	10778 **(64899)**	Yes
2.1 **(2.0)**	13564 **(81615)**	Yes
2.1 **(2.5)**	18236 **(109677)**	Yes

Table A.I: The mesh study done to see how the reliability of the solution is affected by the resolution of the meshing.

Comsol does give more control over defining meshes but if the number of meshes (and hence the degree of freedom to be solved) are low, the solutions could be inaccurate. During the course of our simulations we realized that for low degrees of freedom, a simple re-meshing could give variations in derived parameters between 0.5%-20%. For this reason we did a systematic mesh study and realized that if the number of degrees of freedom solved is above 50,000, the solution given by comsol is accurately reliable. The mesh study is summarized in the Table A.I.

A.II Analytical Modeling

To cross-check the results of Comsol we did a "back of the envelope" analytical calculation. In the device set-up discussed in chapter 5, a hot CNT is imbedded in Pd. The amount of heat the CNT imbedded in Pd can 'dump' into the substrate will be limited by the thermal contact resistance between the CNT and Pd. Since in Comsol, we treat CNT to be in one thermal layer and Pd and substrate to be in another, we can extract the temperature difference between the two thermal layers. Thus the temperature difference between the CNT and substrate layer beneath it, *delT* is known. Keeping this information in mind we set-up a simplified model in which a cylindrical heating source (radius a , & thickness w) is imbedded into cylindrical sink (radius b, & thickness w). The schematic is shown in Figure A.II

The working equation is

$$\nabla^2 T = 0$$

which, in cylindrical coordinates, takes the form

$$\frac{1}{r}\frac{\partial}{\partial r}\left(r\frac{\partial T}{\partial r}\right) = 0$$

$$\partial\left[r\frac{\partial T}{\partial r}\right] = 0,$$

$$\Longrightarrow \quad r\frac{\partial T}{\partial r}|_r - r\frac{\partial T}{\partial r}|_a = 0$$

or

$$(r\frac{\partial T}{\partial r})|_r = (r\frac{\partial T}{\partial r})|_a = \gamma \qquad (1)$$

where

$$\gamma = (r\frac{\partial T}{\partial r})|_a \qquad (2)$$

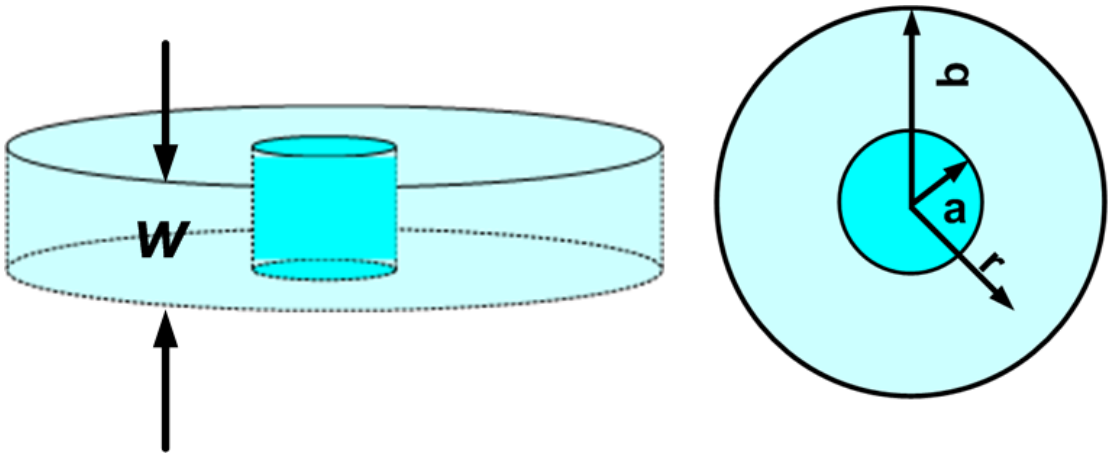

Figure A.II: Cross-sectional & top view of the geometry employed for analytical estimate of thermal contact resistance

solving (1)

$$r\frac{\partial T}{\partial r} = \gamma$$

$$\frac{\partial T}{\partial r} = \frac{\gamma}{r}$$

$$\Delta T = \int_a^b \frac{\gamma}{r} dr = \gamma \ln r|_{r=a}^{r=b}$$

$$\Delta T = \gamma \ln \frac{b}{a} \qquad (3)$$

we calculate γ by noting that the thermal flux ($\kappa\frac{\partial T}{\partial r}$, κ being the thermal conductivity of the substrate SiN_x) when multiplied by the area $area = 2\pi \times a \times w$, gives the power. This is the same power given by the expression

$$P = \frac{2\times a\times delT}{R_c} \qquad (4)$$

Thus,

$$\kappa \frac{\partial T}{\partial r}|_a \times (area) = P = \frac{2 \times a \times delT}{R_c} \qquad (5)$$

$area = 2\pi \times a \times w$. By substituting (2) and (3) in equation (5) we get;

$$\gamma = \frac{\partial T}{\partial r}|_a = \frac{delT}{\pi \kappa w R_c} \qquad (6)$$

We can solve (6) for R_c,

$$R_c = \left(\frac{delT}{\Delta T}\right) \frac{a}{\pi \kappa w} \ln \frac{b}{a} \qquad (7)$$

For $a = 0.5\mu m$, $delT = 7.7\ K, b = 2.5\mu m, \kappa = 2.3 \frac{W}{K} \cdot m, w = 100nm$ and $\Delta T = 1.8\ K$, (7) gives the estimate to be;

$$R_c = 4.8\ K \cdot m/W$$

This is consistent with the value extracted from finite element analysis and these results can be used to cross-check finite element analysis results when meshing problems or other numerical uncertainties are suspected.

A.III Design of the Custom-Built TEM Holder

We designed three TEM specimen holders in total. Two of these specimen holders, custom built for two different TEM models (Jeol 4000FX & Jeol 2100), in addition to imaging have the capability to do four probe electrical measurements. We will refer to each of these holders as “Electrical Measurement Holder”.

The third holder was designed and constructed to calibrate the field of the Objective Lens (OL) of the TEM. In such a holder a Hall sensor was affixed at the location where specimen is conventionally inserted. We will refer to such a holder as “Hall Calibration Holder”.

Since the design and assembly procedure of all three specimen holders was very similar, we will explain the construction details of only one specimen holder. The information regarding the dimensions of the specimen holders was obtained from JEOL.

The body of the specimen holder was machined in three main parts as shown in figure. The first part referred to as “Nose Piece” or the “Tip” in this dissertation requires most care both in design and machining. The second part, referred to as “Mid Part” is relatively simple. This Mid Part contains a guide pin which is aligned to the guide grove in the microscope during specimen insertion (see Figure A.III.2). The rear part of the specimen holder, which we refer to as “Connector End”, has an electronic connector that electrically connects the sample to the external electronics as well as an alignment blade. While connecting the Connector End to the Mid Part care must be taken in ensuring that this alignment blade and the guide pin on the mid part are at the angle specified by manufacturer.

We designed the Nose Piece in such a way that the electrical connection between the sample and the external electronics is made via Beryllium-Copper (Be-Cu) clips and Cu wires. Be-Cu clips make contact with the sample from the back as shown in Figure 4.10 of this dissertation. All the wiring is done on the back side of the specimen holder as well; ergo the groves on that side. The width of these groves was chosen such that there is enough room to work when the wiring is done. These groves are deep enough to ensure that the wires do not stick much out lest they interfere with the parts of the TEM during insertion and withdrawal of the specimen holder. The insulated Cu wires and bare Be-Cu clips are affixed to the specimen

holder by using an insulating epoxy. Wherever electrical insulation between the specimen holder and wires or clips is desired insulating epoxy is used and whenever an electrical connection is desired a conducting epoxy, containing silver, is used. While being very different in composition, both types of epoxies are hardened when cured at or above 70 ^{o}C for more than an hour in a convection oven.

After sonication of machined parts in acetone to rid them of any oily residue and make the holder vacuum compatible, the wiring is done on the machined Nose-Piece, the three parts are permanently attached to each other by using insulating epoxy. Once that is done, appropriate-sized O-rings, lubricated by vacuum compatible vacuum grease, are put onto the specimen holder. Finally the specimen holder is inserted in the TEM and the system is pumped over night to make check if there are any vacuum leaks.

The Solid-Work drawing are shown in the following pages.

Figure A.III.1 The Solid-Works design diagrams of a custom-built TEM specimen holder.

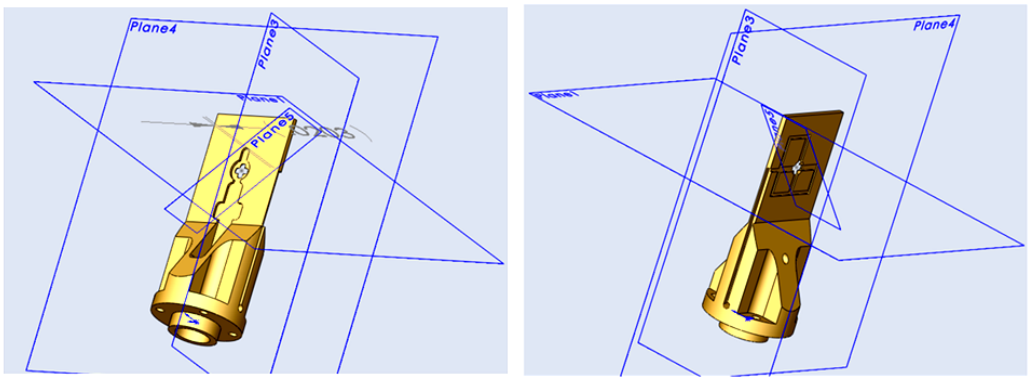

Solid works 3-D drawings of "Nose-Piece"

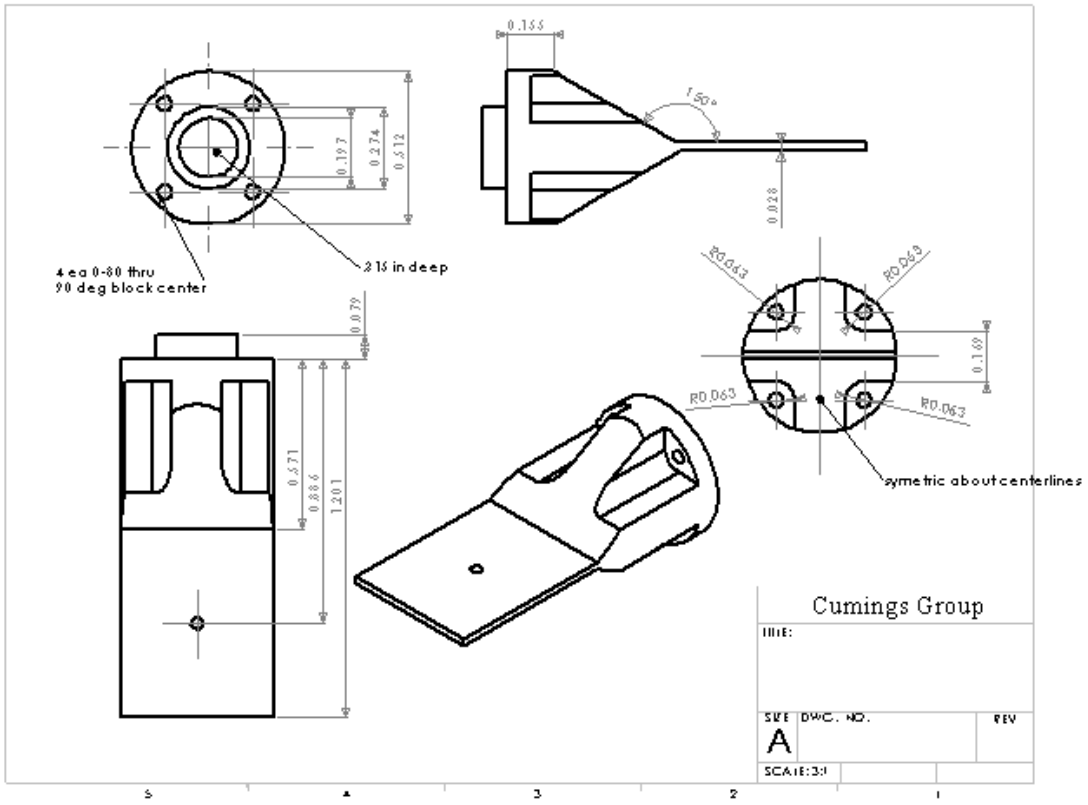

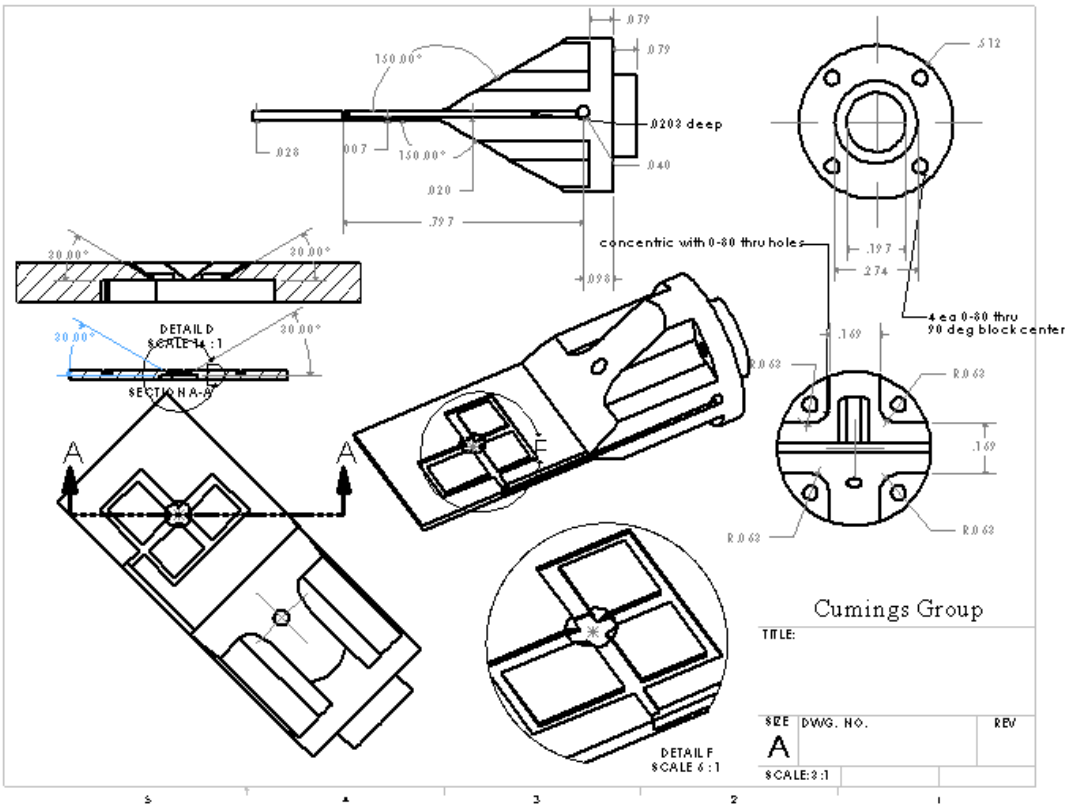
.079
.079
150.00°
.0203 deep
.028
.007
150.00°
.040
.020
.797
.512
.197
.274
concentric with 0-80 thru holes
.098
4 ea 0-80 thru
90 deg block center
.169
R.063
.169
R.063
R.063
20.00°
20.00°
20.00°
20.00°
DETAIL D
SCALE 4 : 1
SECTION A-A
A
A
DETAIL F
SCALE 6 : 1
Cumings Group
TITLE:
SIZE
DWG. NO.
REV
A
SCALE:3:1

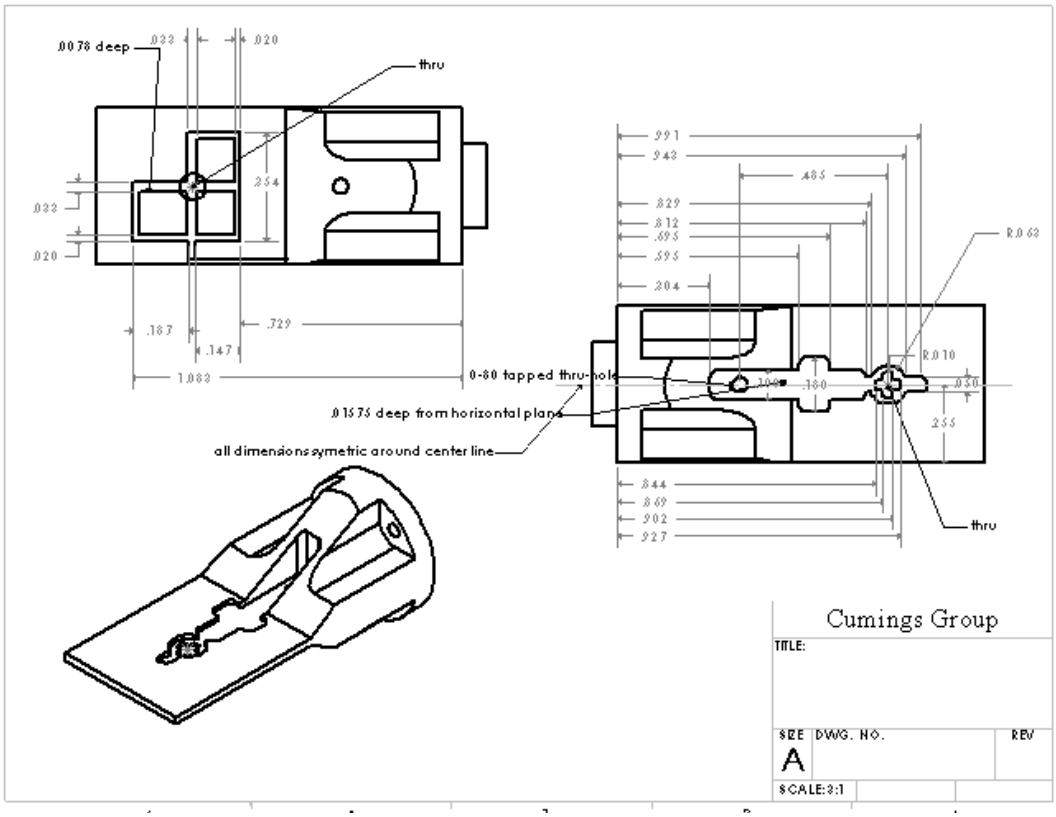
.0078 deep
.033
.020
thru
.254
.033
.020
.187
.147
.729
1.083
.991
.943
.485
.829
.812
.695
.595
.204
R.063
R.010
.180
.030
.255
.844
.869
.902
.927
thru
0-80 tapped thru-hole
.0157 5 deep from horizontal plane
all dimensions symetric around center line
Cumings Group
TITLE:
SIZE
DWG. NO.
REV
A
SCALE:3:1

Figure A.III.2 The Solid Works Drawings Of Mid-Part And Connector End Of The Custom Built Specimen Holder

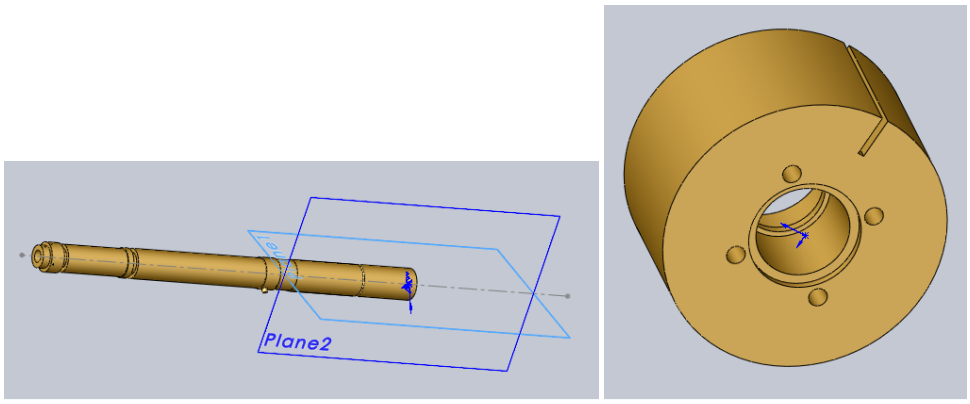

Solid works 3-D drawings of Mid-Part & Connector End

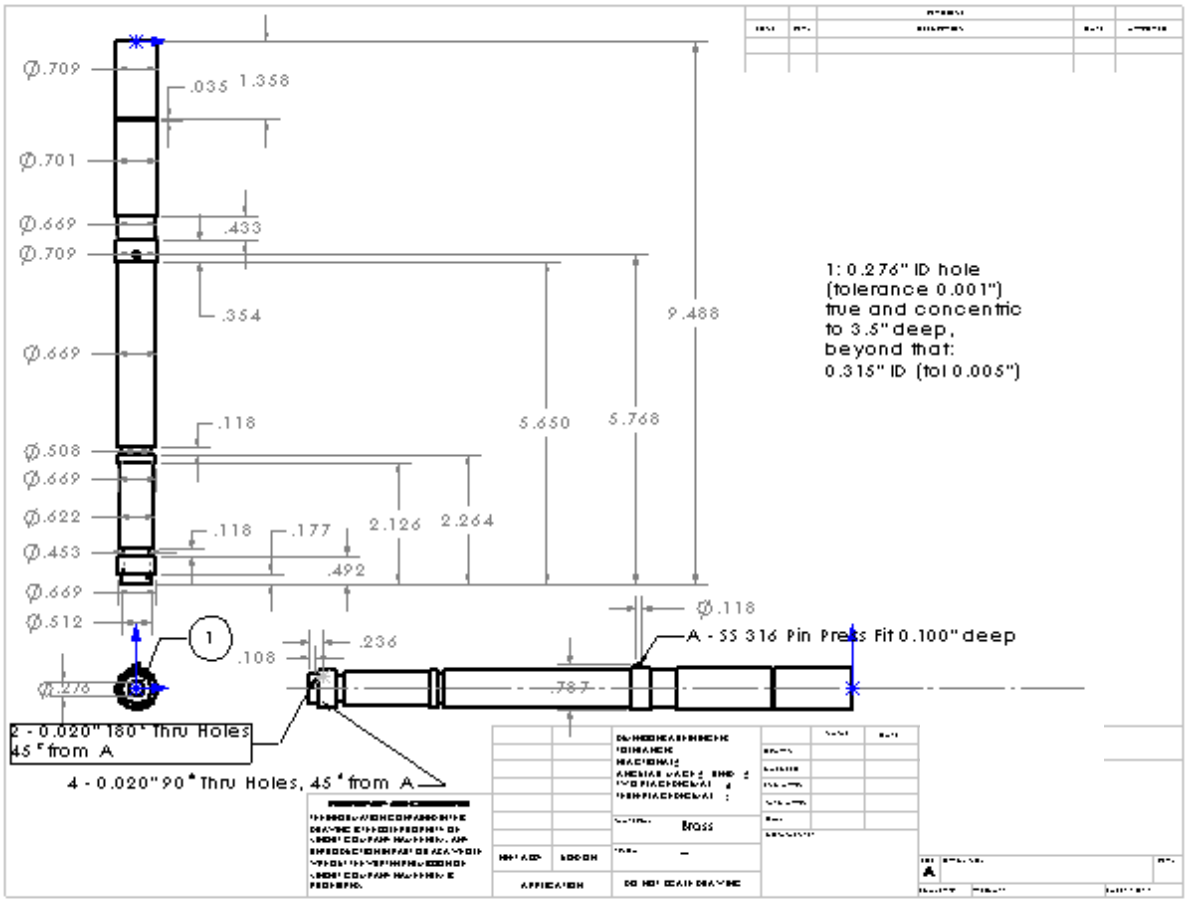

Dimensions of Mid-Part

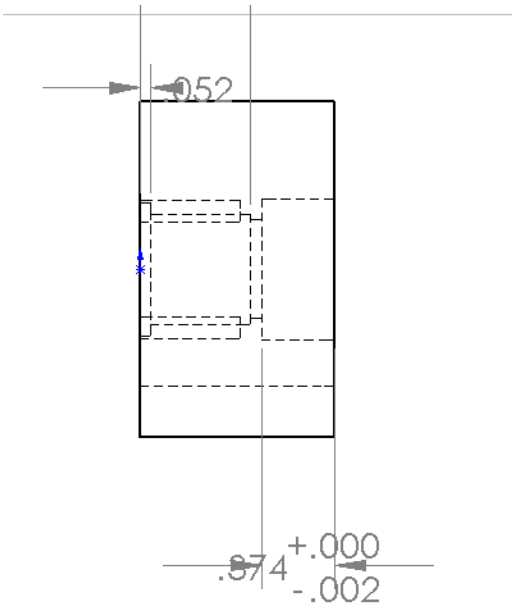

Dimensions of Connector End

Reference List

References Chapter 1

1.1 Radushkevich L.V., Lukyanovich V.M., Zurn Fisic Chim. 24, 111, (1952)

1.2 S. Ijima. Nature, 354, 56 (1991)

1.3 R. Saito, M. Fujita, G. Dresselhaus, M. S. Dresselhaus, Appl. Phys. Lett. 60, 18, 6951 (1992)

1.4 N. Hamada, S, Sawada and A. Oshiyama, Phys. Rev. Lett., 68, 10, 1579 (1992)

1.5 J. W. Mintmire, B. I. Dunlap, C. T. White, Phys. Rev. Lett. 68, 5, 631 (1992)

1.6 T. Guo, P. Nikolaev, A. Rinzler, D. Tomanek, D. Colbet and R. Smalley, J. Phys. Chem. 99, 10694 (1995)

1.7 M. Jose-Yacaman, M. Miki-Yoshida, L. Rendon And J. G. Santiesteban, Appl. Phys. Lett. 62 657 (1993)

1.8 W. Kratschmer, L. Lamb, K. Foristopoulos and D. Huffman, Nature 347, 354 (1990)

1.9 X. Wang, Q. Li, J. Xie, Z. Jin, J. Wang, Y. Li, K. Jiang and S. Fan, Nano Lett. 9, 9 3137 (2009)

1.10 T. W. Ebbesen, Carbon Nanotubes, Ann. Rev. Mater. Sci. , 24, 235 (1994)

1.11 T. W. Ebbesen, Carbon Nanotubes: Preparation and Properties, ed. T. W. Ebbesen, CRC Press, Boca Raton, 1997, p139

1.12 T. W. Ebbesen and P. M. Ajayyan, 358, 220 (1992)

1.13 T. W. Ebbesen, H. Hiura, J. Fujita et. al., Chem. Phys. Lett., 209, 83 (1993)

1.14 G.H. Taylor et. al., Cathode deposits in fullerene formation- microstructural evidence for independent pathways of pyrolytic carbon and nanobody formation, J. Cryst. Growth, 135, 157 (1994)

1.15 X. Zho et. al., Preparation of high grade carbon nanotubes by hydrogen arc discharge, Carbon, 35, 775 (1994)

1.16 X. K. Wang et. al., Carbon nanotubes synthesized in a hydrogen arc discharge, Appl. Phys. Lett., 66, 2430, (1995)

1.17 L. C. Qin, et. al. The smallest carbon nanotube, Nature, 408, 50 (2000)

1.18 H. Yokomichi, et. al. Synthesis of carbon nanotubes by arc discharge in CF_4 gas atmosphere, Jpn. J. Appl. Phys., 37, 6492 (1998)

1.19 K. Shimotani et. al., New synthesis of multi-walled carbon nanotubes using an arc discharge technique under organic molecular atmospheres, Appl. Phys. A, 73, 451 (2001)

1.20 S. Cui et. al., Investigation on preparation of multiwalled carbon nanotubes by DC arc discharge under N_2 atmosphere, Carbon, 42, 931 (2004)

1.21 M. Ishigami et. al. A simple method for the continuous production of carbon nanotubes, Chem. Phys. Lett. 319, 457 (2000)

1.22 H. W. Zhu et. al., Formation of carbon nanotubes in water by the electric-arc technique, Chem. Phys. Lett., 366, 664 (2002)

1.23 X. S. Li et. al., High-yield synthesis of multiwalled carbon nanotubes by water-protected arc discharge method, Carbon 41, 1664 (2003)

1.24 N. Sano et. al., Pressure effects on nanotubes formation using submerged arc in water method, Chem. Phys. Lett., 378, 29 (2003)

1.25 I. Alexandrou et. al., Structure of carbon onions and nanotubes formed by arc in liquids, J. Chem. Phys., 120, 1055 (2004)

1.26 N. Sano, Synthesis of carbon onions in water, Nature, 414, 506 (2001)

1.27 R.T.K. Baker and P.S. Harris Chemistry and Physics of Carbon, Marcel Dekker, Inc., New York pp. 83–165 (1998)

References Chapter 2

2.1 P.R. Wallace. Phys. Rev. 71, 622 (1947)

2.2 X. Blasé, L. X. Benedict, E. L. Shirley. Phys. Rev. Lett. 72, 1878 (1994)

2.3 C.L. Kane and E. J. Mele. Phys. Rev. Lett. 78, 1932 (1997)

2.4 Z. Yao, C. L. Kane, and C. Dekker. Phys. Rev. Lett. 84, 2941 (2000)

2.5 J-Y Park, S. Rosenblatt, Y. Yaish, V. Sazonova, H. Ustunel, S. Braig, T. A. Arias, P. Brouwer and P. L. McEuen, Nano Lett. 4, 517 (2004)

2.6 S. J. Tans, R. M. Verschueren, and C. Dekker. Nature 393, 49 (1998)

2.7 M. Bockrath, J. Hone, A. Zettl, P. L. McEuen, A. G. Rinzler, and R. E. Smalley.Phys. Rev.B 61, 10606 (2000)

2.8 R. Martel, V. Derycke, C. Lavoie, J. Appenzeller, K. K. Chan, J. Terso, and P. Avouris. Phys. Rev. Lett. 8725, 6805 (2001)

2.9 A. Bachtold, P. Hadley, T. Nakanishi, and C. Dekker. Science 294, 1317 (2001)

2.10 V. Derycke, R. Martel, J. Appenzeller, and P. Avouris,Nano Letters 1, 453 (2001)

2.11 C. W. Zhou, J. Kong, E. Yenilmez, and H. J. Dai. Science 290, 1552 (2000)

2.12 S. J. Tans, M. H. Devoret, H. Dai, A. Thess, R. E. Smalley, L. J. Georliga, and C. Dekker. Nature 386, 474 (1997)

2.13 Bockrath, D. H. Cobden, P. L. McEuen, N. G. Chopra, A. Zettl, A. Thess, and R. E. Smalley. Science 275,1922 (1997)

2.14 H. W. C. Postma, T. Teepen, Z. Yao, M. Grifoni, and C. Dekker. Science 293, 76 (2001)

2.15 A. Y. Kasumov, R. Deblock, M. Kociak, B. Reulet, H. Bouchiat, II Khodos, Y. B. Gorbatov, V. T. Volkov, C. Journet, and M. Burghard. Science 284, 1508 (1999)

2.16 A. F. Morpurgo, J. Kong, C. M. Marcus, and H. Dai. Science 286, 263 (1999)

2.17 Tzahi Cohen-Karni , Lior Segev , Onit Srur-Lavi , Sidney R. Cohen & Ernesto Joselevich. Nature Nanotech. 1, 36 - 41 (2006)

2.18 B. Bourlon, C. Miko, L. Forro, D. C. Glattli, and A. Batchtold. Phys. Rev. Lett. 93, 176806 (2004)

2.19 G.W. C. Kaye and T. H. Laby, Tables of Physical and Chemical Constants, 16^{th} ed. Longman, London, (1995)

2.20 J.C. Hones, Studies of 1-D Carbon based Metals: AC_{60} and Carbon Nanotubes, 109 (1998)

2.21 J.C. Hones, Studies of 1-D Carbon based Metals: AC_{60} and Carbon Nanotubes, 111 (1998)

2.22 J. W. Mintmire and C. T. White, Carbon 33, 893-902 (1995)

2.23 N. Hamada, S. Sawada and A. Oshiyama, Phy. Rev. Lett. 68, 1579-1581 (1992)

2.24 J. Heremans, C. P. Beetz Jr.. Phys. Rev. B 32, 1981 (1985)

2.25 M.S. Dresselhaus, G. Dresselhaus, Ph. Avouris (Eds): Cabon Nanotubes, Adv. Topics in Appl. Phys. 88 (2001)

2.26 W. Yi, L. Lu, Z. Dian-lin, Z. W. Pan, S. S. Xie. Phys. Rev. B 59, R9015 (1999)

2.27 P. Kim, L. Shi, A. Majumdar, and P. L. McEuen, Phys. Rev. Lett. 87, 215502 (2001)

2.28 S. Berber, Y. K. Kwon, and D. Tomanek, Phys. Rev. Lett. 84, 4613 (2000)

2.29 E. S. Choi, D. S. Suh, G. T. Kim, D. C. Kim, Y.W. Park,K. Liu, G. Duesberg, and S. Roth, Synth. Met. 103, 2504 (1999)

2.30 R. S. Prasher, X. J. Hu, Y. Chalopin, N. Mingo, K. Lofgreen, S. Volz, F. Cleri, and P. Keblinski

2.31 M. Fujii, X. Zhang, H. Xie, H. Ago, K. Takahashi, T. Ikuta, H. Abe, and T. Shimizu, Phys. Rev. Lett. 95, 065502 (2005)

2.32 G.E. Begtrup, K.G. Ray, B.M. Kessler, T.D. Yuzvinsky, H. Garcia, and A. Zettl, Phys. Rev. Lett. 99, 155901 (2007)

References Chapter 3

3.1 G. L. Pollack, Rev. of Modern Phys. 41, 1 (1969)

3.2 A. A. Abrikosov and I. M. Khalatnikov Sov. Phys. Usp. 66, 68, (1958)

3.3 T. E. Swartz, R. O. Pohl, Rev. of Mod. Phys. 61, 3, 605-668 (1999)

3.4 R. Prasher, Nano Lett. 5, 2155 (2005)

3.5 P. G. Collins, M. Hersam, M. Arnold, R. Martel, and P. Avouris, Phys. Rev. Lett. 86, 3128 (2001)

3.6 H. Maune, H-Y. Chiu and M. Bockrath. Appl. Phy. Lett. 89, 013109 (2006)

3.7 H. Y. Chiu, V. V. Deshpande, H. W. C. Postma, C. N. Lau, C. Miko, L. Forro, and M. Bockrath, Phys. Rev. Lett. 95, 226101 (2005)

3.8 I-K Hsu, R. Kumar, A. Bushmaker and S. B. Cronin, Appl. Phys. Lett. 92, 063119 (2008)

3.9 P. Kim, L. Shi, A. Majumdar and P. L. McEuen, Phys. Rev. Lett. 87, 21, 215502-1 (2001)

3.10 C. H. Yu, S. Saha, J. H. Zhou, L. Shi, A. M. Cassell, B. A. Cruden, Q. Ngo, J. Li, J. Heat Transfer 128, 234, (2006)

3.11 Prasher, Phys. Rev. B, 77, 075424 (2008)

3.12 C. H. Yu, S. Saha, J. H. Zhou, L. Shi, A. M. Cassell, B. A. Cruden, Q. Ngo, J. Li, J. Heat Transfer 128, 234 (2006)

3.13 M. T. Pettes and L. Shi, Adv. Fun. Mat. 19, 3918 (2009)

3.14 A.W. Tsen, A. K. Donev, H. Kurt, L. H. Herman, J. Park. Nature Nanotech. 2, 108-113 (2008)

3.15 A. Majumdar, Ann. Rev. of Mat. Sci., 29, 505, (1999)

3.16 L. Shi, S. Plyasunov, A. Bachtold, P. L. McEuen, and A. Majumdar, App. Phys. Lett.77, 26, (2000)

3.17 P. Kim,L. Shi, A. Majumdar, P. L. McEuen, Mesoscopic Physica B, 323, 67-70 (2002)

3.18 J. Hone, M. Whitney, C. Piskoti, and A. Zettl, Phys. Rev. B 59, R2514 (1999)

3.19 E. Pop, D. Mann, J. Cao, Q. Wang, K. Goodson, H. Dai, Phys. Rev. Lett. 95, 155505 (2005)

3.20 A. Javey, J. Guo, Q. Wang, M. Lundstrom and H. Dai, Nature 424, 654-657 (2003)

3.21 A. W. Bushmaker, V. V. Deshpande, M. W. Bockrath, and S. B. Cronin. Nano Lett. 7, 12, 3618 (2007)

3.22 J-H. Chen, C. Jang, S. Xiao, M. Ishigami and M. S. Fuhrer, Nature Nanotech., 3, 207, (2008)

3.23 A. M. Dasilva, K. Zou, J. K. Jain, and J. Zhu, Phys. Rev. Lett. PRL 104, 236601 (2010)

3.24 V. Perebeinos, S. V. Rotkin, A. G. Petrov, and P. Avouris, Nano lett. 9, 1, 312 (2009)

References Chapter 4

4.1 D. B. Williams and C. B. Carter, Transmission Electron Microscopy, Plenum Press, New York (1996) (ISBN:0-306-45247-2)

4.2 Majumdar, A. Scanning thermal microscopy. Ann. Rev. Mater. Sci. 29, 505 (1999)

4.3 T. Brintlinger, Y. Qi, K. H. Baloch, D. Goldhaber-Gordon, and J. Cumings, Nano Lett., 8(2), 582 (2008)

4.4 Aqua Save is sulfonated polyoniline obtained from Rayon Mitsubishi

4.5 Wiedemann-Franz Law, Kittel, Introduction to Solid State Physics, 5th Ed, Wiley, New York (1976)

4.6 C.H. Mastrangelo, Y. C. Tai and R. S. Mullar, Sensor Actuat a-Phys 23, 856 (1990)

4.7 S. M. Lee and D. G. Cahill, J Appl Phys 81 (6), 2590 (1997)

4.8 W. Holmes, J. M. Gildemeister, P. L. Richards et al., Appl Phys Lett 72, 18, (1998)

4.9 B. L. Zink and F. Hellman, Solid State Comm. 129, 3, 199 (2004)

4.10 H Preston-Thomas, The International Temperature Scale of 1990 (ITS-90) Metrologia, 27, 3, (1990)

4.11 A. Pimpinelli, J. Villain, Physics of Crystal Growth, Cambridge University Press. ISBN 0-521-55198-6 (1999)

4.12 G. Schmid. Chem. Rev. 92, 1709 (1992)

References Chapter 5

5.1 J. Hone, B. Batlogg, Z. Benes, A. T. Johnson, and J. E. Fischer, Science 289, 1730 (2000)

5.2 P. Kim, L. Shi, A. Majumdar, and P. L. McEuen, Phys. Rev. Lett., 215502 (2001)

5.3 M. J. Biercuk, M.C. Llaguno, M. Radosavljevic, J.K. Hyun, A. T. Johnson, and J.E. Fischer, Appl. Phys. Lett. 80, 2767–2769 (2002)

5.4 J. Hone, M.C Llaguno, M.J. Biercuk, A.T. Johnson, B. Batlogg, Z. Benes, J.E. Fischer, Appl. Phys. A 74, 339-343 (2002)

5.5 S. Berber, Y. K. Kwon, and D. Tomanek, Phys. Rev. Lett. 84, 4613 (2000)

5.6 E. Pop, D. Mann, Q. Wang, K. Goodson, and H. J. Dai, Nano Lett. 6, 96 (2006)

5.7 S. Maruyama, Physica B 323,193 (2002)

5.8 D. J. Yang, Q. Zhang, G. Chen, S. F. Yoon, J. Ahn, S. G. Wang, Q. Zhou, Q. Wang and J. Q. Li, Phys. Rev. B 66, 165440 (2002)

5.9 T .Y. Choi, D. Poulikakos, J. Tharian, and U. Sennhauser, NanoLett. 6, 1589 (2006)

5.10 M. Fujii, X. Zhang, H. Q. Xie, H. Ago, K. Takahashi, T. Ikuta, H. Abe, and T. Shimizu, Phys. Rev. Lett. 95, 065502 (2005)

5.11 C. H. Yu, L. Shi, Z. Yao, D. Y. Li, and A. Majumdar, NanoLett. 5, 1842 (2005)

5.12 J. P. Small, K. M. Perez, and P. Kim,Phys. Rev. Lett. 91, 256801 (2003)

5.13 I. K. Hsu, R. Kumar, A. Bushmaker, S. B. Cronin, M. T. Pettes, L. Shi, T. Brintlinger, M. S. Fuhrer, and J. Cumings, Appl. Phys. Lett. 92, 063119 (2008)

5.14 B. Li, L. Wang and G. Casati, Phys. Rev. Lett.93, 184301 (2004)

5.15 B. Li, L. Wang and G. Casati, Lett. 88, 143501 (2006)

5.16 R. S. Prasher, X. J. Hu, Y. Chalopin, N. Mingo, K. Lofgreen, S. Volz, F. Cleri, and Pawel Keblinski, Phy. Rev. Lett. 102, 105901 (2009)

5.17 L. Shi, App. Phys. Lett. 92, 206103 (2008)

5.18 H. Maune, H. Y. Chiu, and M. Bockrath, Appl. Phys. Lett. 89, 013109 (2006)

5.19 C. H. Yu, S. K. Saha, J. H. Zhou, L. Shi, A. M. Cassell, B. A. Cruden, Q. Ngo, and J. Li, J. Heat Transfer 128, 234-239 (2006)

5.20 A. W. Tsen, L. A. K. Donev, H. Kurt, L. H. Herman and J. Park, Nature Nanotechnology 4, 108 - 113 (2008)

5.21 H-Y. Chiu, V. V. Deshpande, H. W. Postma, C. N. Lau, C. Miko, L. Forro, M. Bockrath, Phys. Rev. Lett. 95, 226101, (2005)

5.22 A. Javey, J. Guo, M. Paulsoson, Q. Wang, D. Mann, M. Lundstorm, H. Dai, Phys. Rev. Lett. 92, 106804 (2004)

5.23 E. Pop; D. A. Mann, K. E. Goodson, H. Dai, J. of Appl. Phys. 101, 093710 (2007)

5.24 P. Kim, L. Shi, A. Majumdar, P. L. McEuen,Physica B 323, 67-70, (2002)

5.25 L. Shi, J. Zhuo, P. Kim, A. Batchtold, A. Majumdar, P. L. McEuen, J. Appl. Phys. 105, 104306 (2009)

5.26 M.T. Pettes,L. Shi, Adv. Funct. Mater. (2009), 19, 3918-3925

5.27 G. L. Allen, R. A. Bayles, W. W. Gile,and W. A. Jesser, Thin Solid Films 144(1986)

5.28 N. G. Chopra, L. X. Benedict, V. H. Crespi, M. L. Cohen, S. G. Louie and A. Zettl, Nature 377, 135-138 (1995)

5.29 G. E. Begtrup, K. K. Ray, B. M. Kessler, T. D. Yuzvinsky, H. Garcia and A. Zettl, Phys. Rev. Lett. 99, 155901 (2007)

5.30 Z. Chen, W. Jang, W. Bao, C. N. Lau, and C. Dames. App. Phys. Lett. 95, 161910 (2009)

5.31 T. Hertel, R. E. Walkup and P. Avouris, Phys. Rev. B, 58, 20 (1998)

5.32 M. S. Purewal, B. H. Hong, A. Ravi, B. Chandra, J. Hone, and P. Kim, Phys. Rev. Lett. 98, 186808 (2007)

5.33 M. F. Yu, O. Lourie, M. J. Dyer, K. Moloni, T. F. Kelly, and R. S. Rouff, Science 287, 5453 (2000)

5.34 H. Dai, J. H. Hafner, A. G. Rinzler, D. T. Colbert, and R. E. Smalley. Nature 384, 147 (1996)

5.35 S. Shen, A. Narayanaswamy, and Gang Chen., Nano Lett. 9, 8, (2009)

References Chapter 6

6.10 H. Maune, H. Y. Chiu, and M. Bockrath, Appl. Phys. Lett. 89, 013109 (2006)

6.11 A. W. Tsen, L. A. K. Donev, H. Kurt, L. H. Herman, and J. Park, Nat. Nanotechnol. 4, 108 (2009)

6.12 Y. Fan, S. B. Singer, R. Bergstrom, C. Regan, Phys Rev Lett, 102 (18), 187402 (2009)

6.13 S. Shen, A. Narayanaswamy, and G. Chen. Nano Lett. 9, 2909, (2009)

6.14 V. Perebeinos, S. V. Rotkin, A. G. Petrov, and P. Avouris, Nano lett. 9, 1, 312 (2009)

6.15 B. Li, L. Wang, and G. Casati, Phys. Rev. Lett. 93, 184301 (2004)

6.16 B. Li, L. Wang, and G. Casati, Appl. Phys. Lett. 88, 143501 (2006)

6.17 C.W. Chang, D. Okawa, A. Majumdar, and A. Zettl, Science 314, 1121-1124 (2006)

6.18 M. S. Fuhrer, A. K. L. Lim, L. Shih, U. Varadarajan, A. Zettl, and P. L. McEuen, Physica E 6, 868 (2000)